

# Transition Metal Incorporation: Electrochemical, Structure, and Chemical Composition Effects on Nickel Oxyhydroxide Oxygen-Evolution Electrocatalysts

*Raul A. Marquez,<sup>†</sup> Emma Kalokowski,<sup>†</sup> Michael Espinosa,<sup>†</sup> Jay T. Bender,<sup>‡</sup> Yoon Jun Son,<sup>‡</sup> Kenta Kawashima,<sup>†</sup> Chikaodili E. Chukwuneke,<sup>†</sup> Lettie A. Smith,<sup>†</sup> Hugo Celio,<sup>||</sup> Andrei Dolocan,<sup>||</sup> Xun Zhan,<sup>||</sup> Nathaniel Miller,<sup>§</sup> Delia J. Milliron,<sup>†,‡</sup> Joaquin Resasco,<sup>‡</sup> and C. Buddie Mullins<sup>†,‡,||,⊥,∇,\*</sup>*

<sup>†</sup> Department of Chemistry, The University of Texas at Austin, Austin, Texas 78712, United States.

<sup>‡</sup> McKetta Department of Chemical Engineering, The University of Texas at Austin, Austin, Texas 78712, United States.

<sup>§</sup> Department of Geosciences, The University of Texas at Austin, Austin, Texas 78712, United States.

<sup>||</sup> Texas Materials Institute, The University of Texas at Austin, Austin, Texas 78712, United States.

<sup>⊥</sup> Center for Electrochemistry, The University of Texas at Austin, Austin, Texas 78712, United States.

<sup>∇</sup> H2@UT, The University of Texas at Austin, Austin, Texas 78712, United States.

\* Corresponding author: [mullins@che.utexas.edu](mailto:mullins@che.utexas.edu)

Number of pages: 74

Number of figures: 44

Number of tables: 6

## Table of Contents

Materials .....	3
Electrocatalytic Film Preparation .....	4
Substrate preparation .....	4
Film electrodeposition .....	4
Electrode naming scheme .....	6
Electrochemical Measurements .....	7
Electrochemical cell setup .....	7
Reference electrodes .....	8
Voltammetry and iR compensation .....	9
Electrochemical conditioning .....	10
OER overpotential and Tafel analysis .....	10
Coulouvoltammetry (QV) tests.....	11
Energy storage behavior measurements.....	12
Capacitance measurements from galvanostatic charge-discharge (GCD) cycling .....	13
Electrochemical impedance spectroscopy (EIS) analysis.....	14
Detailed Material Characterization .....	16
Film surface characterization.....	16
Grazing-incidence X-ray diffraction (GIXRD) .....	17
Electron microscopy and electron energy loss spectroscopy (EELS) .....	17
Time-of-flight secondary ion mass spectrometry (TOF-SIMS) .....	18
Inductively coupled plasma mass spectrometry (ICP-MS) .....	18
X-ray photoelectron spectroscopy (XPS) .....	19
Raman spectroscopy .....	20
Supporting Figures and Tables .....	22
References.....	71

## Materials

KOH electrolytes were prepared from reagent-grade potassium hydroxide (Sigma Aldrich, flakes, 89.9% according to the certificate of analysis). The electrolyte was purified following our previous protocol.<sup>1</sup> Nickel(II) nitrate hexahydrate (Thermo Scientific, Puratronic, 99.9985% metal basis) was used for Fe purification and Ni(OH)<sub>2</sub> film electrodeposition. Stock solutions of 1 M KOH electrolyte spiked with different transition metals were prepared using iron(III) nitrate nonahydrate, cobalt(II) nitrate hexahydrate, manganese(III) nitrate hydrate, and copper (II) nitrate hydrate (Thermo Scientific, Puratronic, >99.995% metal basis). Iron(II) chloride tetrahydrate (Thermo Scientific, 99.94% metal basis) and sodium nitrate (Thermo Scientific, 99+%) were used for films containing codeposited Fe, while cobalt(II) nitrate hexahydrate was used for films containing Co. Ethylenediaminetetraacetic acid (EDTA) tetrasodium salt dihydrate (Sigma Aldrich, 99.5%) was dissolved in the 1 M KOH electrolyte for ion complexation studies. Ethanol (Pharmco, 99.5%) was used to clean Ni foil (NF) substrates. High-purity hydrochloric acid (Thermo Scientific, 99.999% metal basis) was used to prepare 3 M HCl solutions for Ni foil cleaning. Acid dilutions for cleaning glassware and ICP-MS analysis were prepared using TraceMetal grade nitric acid (Fisher Scientific, 67 - 70%, Fe < 1 ppb). All the electrolytes and acid dilutions were prepared with deionized (DI) water (18.2 M $\Omega$ ·cm). Ni foil (Thermo Scientific, 99.5%, annealed) with a thickness of 0.05 mm was used as the substrate for electrocatalytic film deposition. Potassium chloride (Sigma-Aldrich, ~3 M KCl saturated with AgCl) was used for roughening Au substrates.

## Electrocatalytic Film Preparation

### *Substrate preparation*

Ni foil pieces ( $20 \times 10 \times 0.25$  mm) were cut and immersed in ethanol within shell type 1 glass vials (Fisher Scientific,  $15 \times 45$  mm), placed in an ultrasonic bath for 15 minutes, and dried overnight in a vacuum oven at  $60$  °C. The exposed electrode surface area was fixed using a polydimethylsiloxane (PDMS) coating (SYLGARD 184 Silicone Elastomer Kit, Dow). The coating was prepared by vigorously mixing the curing elastomer base and the curing agent in a 10:1 ratio for 10 min using a polytetrafluoroethylene (PTFE) rod. Next, this mixture was degassed in a vacuum oven for about 5 minutes or until no bubbles remained visible. The liquid PDMS mixture was carefully applied to a 5 mm segment extending from the foil's center towards its right and rear sides, exposing a  $10 \times 10$  mm<sup>2</sup> area on one side. A 5 mm flat portion was intentionally left uncoated to serve as a clipping region. The PDMS-coated Ni foil pieces were cured in a small oven at  $150$  °C for 10 min as recommended by the manufacturer. After curing, the electrodes were kept in a vacuum oven until use. Prior to electrochemical measurements, the PDMS-coated electrodes were placed inside clean shell type 1 vials and sequentially cleaned for 15 minutes each in three solutions: (1) ethanol, (2) 3 M HCl, and (3) deionized water.

### *Film electrodeposition*

We deposited our electrocatalytic films using a thin-film architecture to minimize electrical conductivity and mass transport effects.<sup>2</sup> As suggested by previous studies,<sup>2-4</sup> hydroxide catalyst films were cathodically deposited using a two-electrode configuration from a 20 mM nickel(II) nitrate aqueous solution. The pH of the plating bath was adjusted to  $\sim 3$  using 1 M nitric acid. A 50 mL glass cell, cleaned with nitric acid, was filled with  $\sim 15$  mL of the plating bath and purged with

N<sub>2</sub> gas for 5 min. A Ni foam counter electrode (geometric area: 2 x 2 cm<sup>2</sup>) was fixed at a constant distance (1 cm) from the working electrode. A distinct Ni foam counter electrode was employed for each deposition of the same type of film to prevent cross-contamination. The working electrode was secured with a Ti clip holder and aligned parallel to the counter electrode. Upon cell assembly, the films were deposited galvanostatically at -1 mA·cm<sup>-2</sup> for 300 s, equivalent to a final deposition charge of 300 mC·cm<sup>-2</sup> (thickness: ~550 nm). Electrodeposition was executed without stirring in a sequence of three intervals of 100 s with resting periods of 10 s to minimize concentration gradients.<sup>5</sup> A constant flow of N<sub>2</sub> gas was maintained in the headspace to sustain positive pressure within the cell and prevent O<sub>2</sub> from entering.

For films containing codeposited Fe and Co, the total metal content in the solution was held at 20 mM. For example, NiFe films were deposited from a 10 mM Fe(II) and 10 mM Ni(II) nitrate solution and adjusted to pH ~3. While nitrate salts of Ni and Co were used directly, Fe-containing films were prepared using FeCl<sub>2</sub>·4H<sub>2</sub>O and NaNO<sub>3</sub> to prevent precipitation of insoluble Fe oxides/hydroxides. This solution was freshly prepared on the day of Fe film deposition and purged with N<sub>2</sub> before and after adding FeCl<sub>2</sub>. A stoichiometric amount of NaNO<sub>3</sub> was added to maintain the total nitrate concentration constant across all plating baths. After deposition, the films were carefully rinsed with DI water and dried in a vacuum oven until use. Fe-containing films were tested immediately after deposition. Co and Fe contents in bimetallic samples were quantified by energy-dispersive X-ray spectroscopy (EDX).

### *Electrode naming scheme*

Electrocatalytic films follow a specific naming convention based on the substrate and chemical composition. The naming convention is as follows:

*Substrate abbreviation:* This study used only two substrates, Ni foil substrate (NF) and roughened gold substrate (Au).

*Chemical composition:* Metals in the sample name reflect only those initially deposited before conducting any conditioning or aging procedure. For example, Ni indicates the deposition of nickel only, while NiFe indicates the deposition of both nickel and iron (*i.e.*, bimetallic film).

*Chemical phase:* Films designated as oxyhydroxide (*e.g.*, NiOOH) have undergone electrochemical conditioning, resulting in the formation of the oxyhydroxide phase. Films designated as hydroxides [*e.g.*, Ni(OH)<sub>2</sub>] have not undergone electrochemical conditioning. These samples include as-deposited films or electrodes aged in KOH electrolyte, as indicated by the figure description.

*Deposited charge:* Unless stated otherwise, all films were deposited to a final charge of 300 mC·cm<sup>-2</sup>. Films were deposited to a final charge of 50 mC·cm<sup>-2</sup> for specific measurements. These films are regarded as *thin* throughout the text and are denoted by a "t" preceding their composition.

For example, consider the following electrode samples:

**NF-NiOOH** refers to a Ni(OH)<sub>2</sub> film deposited on Ni foil substrate to a final charge of 300 mC·cm<sup>-2</sup>, then subjected to electrochemical conditioning, which resulted in a NiOOH phase.

**Au-t-NiOOH** refers to a Ni(OH)<sub>2</sub> film deposited on a roughened Au substrate to a final charge of 50 mC·cm<sup>-2</sup>, then subjected to electrochemical conditioning, which resulted in a NiOOH phase.

## Electrochemical Measurements

### *Electrochemical cell setup*

Electrochemical tests were performed in a 100 mL PTFE cell to avoid contamination from glassware, as described in our previous study.<sup>1</sup> The cell was cleaned before experiments with 3 M HNO<sub>3</sub> and rinsed with copious DI water. Electrochemical measurements were conducted using a Gamry Reference 620 potentiostat/galvanostat in a three-electrode configuration. A graphite rod (Gamry) was used as a counter electrode to avoid incidental Pt incorporation.<sup>6</sup> The counter electrode was cleaned periodically by soaking in 3 M HNO<sub>3</sub>. Fresh and clean graphite rods and PTFE cells were used for each metal-containing 1 M KOH electrolyte. Each tested sample underwent three replicate measurements.

Fresh KOH electrolyte was used for each electrochemical test. The electrolytes were standardized and purified according to our previous guidelines.<sup>1</sup> Before electrochemical tests, the electrolytes were degassed with high-purity O<sub>2</sub> for 30 min using a plastic bubbler. Due to reproducibility concerns, we used magnetic stirring to dislodge bubbles only after degassing the electrolyte but not during electrochemical tests. Stock solutions containing 1 M KOH and 10 ppm of various transition metal cations were prepared by dissolving the appropriate nitrate salts in purified 1 M KOH. Aliquots were drawn from these stock solutions to achieve the specific concentrations required for each experiment. For ion complexation studies, we prepared a 10 mM EDTA stock solution and took aliquots to reach target EDTA concentrations. We selected EDTA concentrations of 0.5 and 1.0 mM based on the total concentration of potential interfering ions in the KOH electrolyte that could be complexed by EDTA (refer to **Figure S5** and **Table S6** for details). The mixture of KOH, transition metals, and EDTA was allowed to stabilize for 12 hours before initiating the tests.

### Reference electrodes

All potentials were measured against a Hg/HgO reference electrode with 1 M KOH electrolyte as the filling solution (CH Instruments). A separate Hg/HgO reference electrode was used for tests in purified 1 M KOH to avoid incidental cross-contamination. Potentials were converted to the reversible hydrogen electrode (RHE) according to the equation:

$$E_{\text{RHE}} = E_{\text{Hg/HgO}}^{\circ} + 0.0592(\text{pH}) + E_i \quad (1)$$

where  $E_i$  is the measured potential vs. Hg/HgO. The value of  $E_{\text{Hg/HgO}}^{\circ}$  in 1 M KOH was determined experimentally by measuring the open circuit potential (OCP) for 5 min against a saturated calomel electrode (SCE) used only for this purpose. The value of  $E_{\text{Hg/HgO}}^{\circ}$  was determined by considering the liquid junction potential difference in the OCP measurement according to the following equation:<sup>7</sup>

$$E_{\text{Hg/HgO}}^{\circ} = E_{\text{OCP}} + E_{\text{SCE}}^{\circ} - E_{\text{LJP}} \quad (2)$$

where  $E_{\text{OCP}}$  is the measured OCP value,  $E_{\text{SCE}}^{\circ}$  is the half-cell standard reduction potential of the SCE (0.2412 V vs. SHE at 25 °C, KCl sat.), and  $E_{\text{LJP}}$  is the liquid junction potential difference (6.4 mV for KCl sat. | 1 M KOH).<sup>7</sup> The average experimental value of  $E_{\text{Hg/HgO}}^{\circ}$  in 1 M KOH was determined to be  $108.0 \pm 2.1$  mV. This potential was periodically monitored to ensure stability between experiments. Additionally, we used a standard hydrogen electrode (SHE) to calibrate the saturated calomel electrode and correct for potential drift between measurements.<sup>7</sup> The SHE was made using a platinized Pt electrode in acidic electrolyte having a unit activity of  $\text{H}^+$  and  $\text{H}_{2,\text{(g)}}$  (1 bar). The reversible potential for hydrogen is estimated as the average between forward and reverse sweeps around the potential of zero current. More details can be found elsewhere.<sup>7-9</sup>

### *Voltammetry and iR compensation*

The OCP was measured for one hour before experiments or until the potential was completely stable (typically between -0.05 and -0.15 V vs. Hg/HgO,  $\pm 5$  mV variation). Linear sweep voltammetry (LSV) and CV scans to compare the samples before and after electrochemical conditioning were recorded at a scan rate of  $5 \text{ mV}\cdot\text{s}^{-1}$  to minimize capacitive contributions. CV scans were performed between 0.15 and 0.80 V vs. Hg/HgO for most measurements, only being different for Fe-containing electrolytes (*i.e.*, between 0.15 and 0.70 V vs. Hg/HgO). The third scan is reported for LSV and CV recorded before and after conditioning. LSV and CV scans were corrected for 85% uncompensated resistance ( $R_u$ ) using the positive feedback mode in the Gamry software.  $R_u$  was determined using electrochemical impedance spectroscopy (EIS) by identifying the minimum point of total impedance at high frequencies (between 80 and 30 kHz). Measurements were taken at a stable OCP and an amplitude of 5 mV, where the phase angle approaches zero and both capacitive and inductive impedances become negligible.<sup>3,10</sup> **Figure S1** displays a typical Nyquist plot measured at the OCP. The value of  $R_u$  varied from 1.9 to  $2.4 \Omega$  for films deposited on Ni foil substrate.  $R_u$  was monitored periodically among experiments to ensure good contact with the Ti clip electrode (variation was  $\sim 0.02 \Omega$ ).

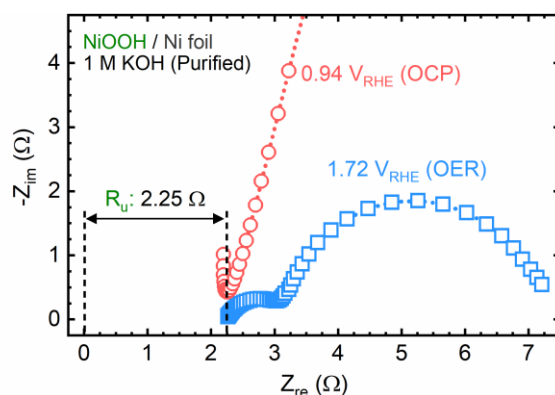


**Figure S1.** High-frequency Nyquist plots of an NF-NiOOH electrode measured both at the OCP and in the OER active potential range. The resulting  $R_u$  value is displayed for reference. The Nyquist plot measured at the OCP is offset on the y-axis for clarity.

### *Electrochemical conditioning*

For examining the OER catalytic activity, electrochemical conditioning was performed *via* chronopotentiometry (CP) at a constant current density of  $2.5 \text{ mA}\cdot\text{cm}^{-2}$  for at least 12 h to favor the formation of a thin and compact hydrous oxide layer on the surface.<sup>11</sup> The electrolyte was stirred with a magnetic stir bar for 5 min after conditioning to dislodge bubbles. Following electrochemical conditioning, electrochemical measurements were performed (*vide infra*). For examining the electrochemical energy storage properties of  $\text{Ni}(\text{OH})_2/\text{NiOOH}$  films deposited on Ni foil, electrochemical conditioning consisted of galvanostatic charge-discharge (GCD) cycling tests at  $2.5 \text{ mA}\cdot\text{cm}^{-2}$  for a total of 1600 cycles. For each GCD cycle, a constant current was applied to charge/discharge the electrode between the starting potential (*i.e.*, 0.15 V *vs.* Hg/HgO) and the full-charge potential; the latter corresponds to the OER onset potential and was determined for each electrocatalytic film exposed to transition metals using the coulombometry (QV) method (*vide infra*).<sup>12</sup> GCD tests at different currents were also performed for each catalytic film.

### *OER overpotential and Tafel analysis*

The overpotential ( $\eta$ ) was calculated using the equation  $\eta = E_i - E_{\text{rev}}$  where  $E_i$  is the measured potential (corrected for 85%  $R_u$ ) and  $E_{\text{rev}}$  is the reversible potential of the OER (0.306 V *vs.* Hg/HgO).<sup>13</sup> All the current densities were calculated from a projected geometric area ( $\sim 1 \text{ cm}^2$ ) defined by the PDMS coating and measured using an optical profilometer. This coating effectively prevented the electrolyte from reacting with the bare Ni foil substrate, so only the  $\sim 1 \text{ cm}^2$  area containing the electrocatalytic film was converted into the active NiOOH film during electrochemical conditioning. In contrast, the rest of the Ni foil substrate remained unchanged.

Tafel slopes were estimated using multistep chronoamperometry (MUSCA) and multistep chronopotentiometry (MUSCP) methods, as these reflect steady-state responses that are more suitable for Tafel analysis, contrary to traditional potentiodynamic polarization curves.<sup>14</sup> MUSCA measurements were performed by applying about 16 potential steps starting from the OER onset potential with 10 mV increments. Each step lasted 600 s, but only the last 300 s were averaged for Tafel analysis. MUSCP measurements were performed by applying a series of current steps starting from 0.25 mA to 1.50 mA with 0.05 increments, each lasting 300 s. The OER overpotentials were corrected for 100%  $iR$  drop using the  $R_u$  value from EIS as follows:

$$E_{iR,corr} = E_{RHE} - iR_u \quad (3)$$

where  $i$  is the steady-state current for each step, and  $E_{RHE}$  is the electrode potential converted to the RHE scale. Tafel plots were constructed by plotting the logarithm of the sampled currents against the respective OER overpotentials. The OER charge calculated from QV measurements was also used to construct Tafel plots (*vide infra*).

#### *Coulovoltammetry (QV) tests*

The QV method was utilized to determine the OER onset potential based on previously established methodologies.<sup>12</sup> In brief, a sequence of CV scans is executed with varying vertex potentials (*i.e.*, the potential limit of the scan where the sweep direction is reversed) across a potential range (from 0.45 to 0.75 V vs. Hg/HgO) where redox peaks could mask the OER onset potential. Next, the charge density (in C·cm<sup>-2</sup>) is calculated by integrating the area under the voltammetric response at each vertex potential. When an irreversible reaction occurs, the charge consumed during the anodic scan surpasses that of the cathodic scan, resulting in a net positive charge density. For these measurements, we opted for thin electrocatalytic films (*i.e.*, NF-*t*-

NiOOH) with a charge of  $50 \text{ mC}\cdot\text{cm}^{-2}$  and an approximate thickness of 80 nm. CV scans were conducted without  $iR$  compensation to circumvent charge-trapping effects.<sup>2</sup> These QV tests were performed after electrochemical conditioning *via* CP ( $1 \text{ mA}\cdot\text{cm}^{-2}_{\text{geo}}$  for 5 min) to ensure consistent and reproducible results. The charge was measured on the first scan to account for all the redox-active cations in the film. To achieve the complete reduction of the film before subsequent CV scans at higher vertex potentials, we applied a cathodic step at  $-0.5 \text{ vs. Hg/HgO}$  for 600 seconds or until the reduction current stabilized. The OER onset potential was determined by plotting the charge density (*i.e.*, OER charge) against the vertex potential and calculating the first derivative.

#### *Energy storage behavior measurements*

CV scans at different sweep rates were utilized to evaluate the charge storage behavior of the NF-NiOOH electrodes. CV scans around the  $\text{Ni}^{2+/3+}$  redox peak (from 0.1 to 0.65 V *vs.* Hg/HgO) were measured at varying scan rates from 10 to 100  $\text{mV}\cdot\text{s}^{-1}$  without  $iR$  compensation. The relationship between the peak current  $j$  with the scan rate  $\nu$  was examined as follows:

$$\begin{aligned} i &= a\nu^b \\ \log i &= b \log \nu + \log a \end{aligned} \quad (4)$$

A linear plot of  $\log i$  against  $\log \nu$  yields a slope  $b$ . A  $b$  value of 0.5 indicates that charge storage is governed by diffusion (*i.e.*, Faradaic or redox charge storage), with the peak current response proportional to the square root of the scan rate ( $i \sim \nu^{1/2}$ ). A  $b$  value of 1.0 implies capacitor-like behavior (*i.e.*, charge storage on the surface), with peak current response proportional to the scan rate ( $i \sim \nu$ ).<sup>15</sup>

### Capacitance measurements from galvanostatic charge-discharge (GCD) cycling

Following electrochemical conditioning of NF-NiOOH films through GCD cycling, the total capacitance ( $C_{\text{tot}}$ ) below the OER onset potential was estimated as follows:<sup>16</sup>

$$C_{\text{tot}} = \frac{Q}{\Delta V} \quad (5)$$

where  $Q$  is the total charge (*i.e.*, capacity) of each cycle, and  $\Delta V$  is the potential window set for GCD. **Note:** as explained previously in the electrochemical conditioning subsection, the potential window was set based on a starting potential of 0.15 V *vs.* Hg/HgO and the full-charge potential, which varied depending on the OER onset potential corresponding to each electrocatalytic film and determined by the QV method (see **Tables S1** and **S2** for onset potential values for each film).

The total capacitance is determined for each cycle using the Gamry Echem Analyst software, and therefore, it varies throughout GCD cycling. Thus, a plot of the capacitance *vs.* cycle number is obtained (see **Figure S11c**). The  $C_{\text{tot}}$  value corresponding to each film was determined by averaging the values for the last 100 cycles, where the total capacitance curve stabilizes. This average  $C_{\text{tot}}$  value was used to determine the  $C_{\text{redox}}$  value (*vide infra*).

The Gamry Echem Analyst software provides additional figures of merit to evaluate the energy storage properties. The capacity retention ( $C_{\text{ret}}$ , shown as %Capacity in the Gamry Echem Analyst software) is determined as follows:

$$C_{\text{ret}} = \frac{Q_i}{Q_0} \quad (6)$$

where  $Q_i$  is the total charge of each cycle, and  $Q_0$  is the total initial charge calculated from the whole GCD cycling experiment. The coulombic efficiency ( $Q_{\text{eff}}$ ) is calculated as the ratio of the charge in the charge and discharge steps for each cycle. The energy is calculated as the sum of the

electric power multiplied by time. The energy efficiency is calculated as the ratio of energy in the charge and the discharge steps for each cycle. The Gamry Echem Analyst software provides these parameters automatically from the GCD cycling test.

**Note:** Ni(OH)<sub>2</sub>/NiOOH electrodes display distinct redox peaks from CV scans and a nonlinear GCD profile, indicating faradaic charge storage (*i.e.*, battery-type) rather than true pseudocapacitive behavior, which follows a linear dependence on the stored charge with the width of the potential window.<sup>15,17,18</sup> Thus, our electrodes function as redox-enhanced electrochemical capacitors (redox ECs).<sup>19</sup> It has been suggested that capacity (*i.e.*, charge) rather than capacitance should be used to measure their performance, as the capacitance varies with the potential window used.<sup>17,19</sup> However, we opted to use capacitance to examine changes in energy storage properties, aiming to subtract the double-layer capacitance ( $C_{dl}$ ). Comparing capacitances of different redox ECs is only valid when the same potential window is used. GCD testing of the NF-NiOOH electrodes exposed to various transition metal cations was conducted within roughly the same potential window (see the OER onset potentials in **Tables S1** and **S2**). The potential window was slightly different only for NF-NiOOH electrodes conditioned in Fe-containing KOH due to the OER onset. Note that this comparison is valid only among comparable redox ECs to evaluate changes in stored charge. Capacitance values derived from our study should not be compared to other energy storage materials in the literature; instead, capacity should be used.

#### *Electrochemical impedance spectroscopy (EIS) analysis*

Potentiostatic EIS measurements were performed to estimate the charge transfer resistance ( $R_{ct}$ ) associated with the OER and the  $C_{dl}$ . EIS was measured in the frequency range from 0.1 to  $10^6$  Hz at an amplitude of 5 mV. Potentials in the 0.50 to 0.75 V vs. Hg/HgO range were probed

to compare similar current densities before and after electrochemical conditioning.<sup>20</sup> EIS fitting was performed using a general Randles equivalent circuit model, including a term for the contact resistance (**Figure S2**). In this model,  $R_s$  represents the series resistance resulting from the sum of the solution resistance of the electrolyte and the electrocatalytic film resistance.<sup>21,22</sup>  $R_c$  and  $CPE_c$  denote the impedance originated from the contact between the film and the electrode clip.  $R_{ct}$  and  $CPE_{ct}$  represent the total charge transfer resistance and the constant phase element, respectively, characterizing the catalytic interface.

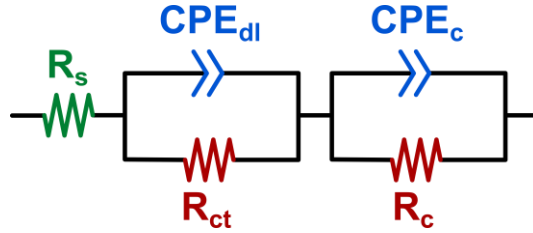


**Figure S2.** Equivalent circuit model for EIS data fitting.

Fitted parameters were determined using the Gamry Echem Analyst software. The  $C_{dl}$  was calculated according to the following equation:<sup>20,23</sup>

$$C_{dl} = CPE_{ct} \times (\omega_{max})^{n-1} \quad (7)$$

where  $\omega_{max}$  (in  $s^{-1}$ ) is the frequency at which the imaginary component of the Nyquist plot reaches a maximum,  $n$  represents the degree of depression of the semicircle compared with an ideal semicircle and has a value less than 1.0, and  $CPE_{ct}$  is the constant phase element used to model the charge-transfer process. This value was used to separate the  $C_{redox}$  contribution to the total capacitance determined through GCD tests as follows:

$$C_{redox} = C_{tot} - C_{dl} \quad (8)$$

## Detailed Material Characterization

### *Film surface characterization*

The surface characteristics of the as-deposited films were analyzed using non-contact profilometry (NCP) with a Keyence VK-X1100 Optical profilometer. Surface roughness and film thickness were estimated from 3D surface profiles obtained with a 404 nm laser and a 50x objective lens. The electrochemically active surface area (ECSA) for the Ni foil substrate was determined through CV scans at varying scan rates, conducted in a CH<sub>3</sub>CN solution containing 0.15 M KPF<sub>6</sub> as supporting electrolyte.<sup>24</sup> For these electrochemical measurements, we employed a glass cell separated by a porous glass frit for the working and counter electrodes. A platinum mesh (2.5 x 2.5 cm<sup>2</sup>) served as the counter electrode, while a silver wire enclosed in a Luggin capillary filled with the same electrolyte was used as the reference electrode. The tip of this capillary was positioned approximately 1 cm away from the working electrode. The working electrode compartment contained about 30 mL of solution, and 10 mL was used in the counter electrode compartment to balance the hydrostatic pressure. Before initiating measurements, the electrolyte was purged with N<sub>2</sub> gas for 10 minutes. A constant flow of N<sub>2</sub> was maintained in the headspace throughout the measurements to keep a positive pressure. Following best practices outlined in a prior study,<sup>25</sup> the OCP was monitored until it stabilized, typically within 10 min. Next, CV scans ranging from 10 to 1000 mV·s<sup>-1</sup> were conducted around ±200 mV of the stable OCP value, *iR* compensation was implemented using the current interruption method, and the current sensitivity was set to 25% higher than the maximum current at each scan rate. Average cathodic and anodic currents were plotted against the scan rate, and an allometric function ( $y = bv^\alpha$ ) was fitted to derive the C<sub>dl</sub> value from constant *b*. For additional details, please refer to **Figure S4** and its supporting note.

### *Grazing-incidence X-ray diffraction (GIXRD)*

GIXRD was utilized to examine the crystallinity of the as-deposited Ni(OH)<sub>2</sub> film deposited on Ni foil. Measurements were conducted on a Rigaku Ultima IV diffractometer equipped with a Cu K $\alpha$  ( $\lambda = 1.54186 \text{ \AA}$ ) radiation source at 40 kV and 44 mA. The scan rate was 0.5 degrees per minute, using a thin-film configuration with an incident angle of 0.3°.

### *Electron microscopy and electron energy loss spectroscopy (EELS)*

Scanning electron microscopy (SEM) images and EDX elemental maps were acquired using a Thermo Scientific Apreo 2 microscope to study the morphology. SEM imaging was conducted at high vacuum ( $\sim 5 \times 10^{-6}$  Torr), a 4 nm spot size, a 0.40 nA current, and a 10 kV accelerating voltage. For high-angle annular dark-field scanning transmission electron microscopy (HAADF-STEM) imaging and EELS analysis, samples were prepared as follows: NF-NiOOH electrodes were aged for one week in 2 mL of purified 1 M KOH spiked with transition metals (500 ppb M<sup>n+</sup>). The films were then conditioned *via* CP @ 2.5 mA·cm<sup>-2</sup> for 15 min. Next, the electrodes were sonicated for 5 min in 2 mL of ethanol within shell-type 1 glass vials. A total of 7.5  $\mu$ L were dropcast onto Cu grids (Ted Pella, ultrathin C film on Lacey carbon, 400 mesh) in three 2.5  $\mu$ L increments and allowed to dry in a vacuum oven between each step. HAADF-STEM and EELS measurements were conducted in a JEOL NEOARM probe-corrected transmission electron microscope with aberration correction. All measurements were performed at an operating voltage of 80 kV. EDX elemental maps were captured with a JEOL large-angle silicon drift detector. EELS measurements utilized a Gatan Quantum energy filter with a Dual EELS detector. HAADF-STEM images were analyzed using the Gatan Microscopy Suite. EELS spectral processing was done using the HyperSpy v1.7.3 toolbox.<sup>26</sup>

### *Time-of-flight secondary ion mass spectrometry (TOF-SIMS)*

Depth profiles and high-resolution elemental maps were acquired using an IONTOF GmbH TOF-SIMS 5 instrument in ultrahigh vacuum ( $\sim 10^{-9}$  Torr). For depth profiling in negative polarity, a  $\text{Cs}^+$  beam (40 nA, 0.5 kV) was applied to sputter an area of  $300 \times 300 \mu\text{m}^2$ . Then, a  $\text{Bi}^+$  analysis beam (4 pA, 30 keV) was used to raster-scan an area of  $100 \times 100 \mu\text{m}^2$  centered within the Cs-sputtered crater. In positive polarity, an  $\text{O}_2^+$  beam (40 nA, 1 kV) was used instead of  $\text{Cs}^+$ . The instrument was configured to fast-imaging mode for high-resolution imaging, achieving a lateral resolution of approximately 200 nm and a current of  $\sim 0.4$  nA. For TOF-SIMS analysis, NF-NiOOH electrodes were aged for one week in 2 mL of purified 1 M KOH spiked with transition metals (100 ppb  $\text{Fe}^{3+}$ ,  $\text{Co}^{2+}$ , and  $\text{Mn}^{2+}$ ). After aging, the films were conditioned *via* CP @ 2.5  $\text{mA}\cdot\text{cm}^{-2}$  for 10 min. The samples were rinsed with DI water and dried in a vacuum oven until analysis.

### *Inductively coupled plasma mass spectrometry (ICP-MS)*

Solution-mode ICP-MS was employed to measure metal concentrations in the KOH electrolyte. We conducted a 1000x dilution routine as outlined in our previous work.<sup>1</sup> Samples were collected from the electrochemical cell at specified intervals, with each aliquot being 250  $\mu\text{L}$  in volume. This dilution was essential to enhance instrument stability and optimize plasma performance due to the complexity of the 1 M KOH matrix, which has high total dissolved solids primarily consisting of  $\text{K}^+$  and  $\text{Na}^+$ . This process ensured that the detection limits for all analytes remained in the low ppb range. Solution-mode ICP-MS measurements were conducted on an Agilent 7500ce spectrometer equipped with a quadrupole mass analyzer and a collision/reaction cell. The method was optimized by tuning the plasma in no gas, He, and  $\text{H}_2$  modes to eliminate

unwanted polyatomic interferences. The accuracy and precision of the method were verified by analyzing quality control and spiked samples prepared from reference standards. Calibration curves for the isotopes under investigation were also established. A comprehensive explanation of this methodology is available elsewhere.<sup>1</sup>

#### *X-ray photoelectron spectroscopy (XPS)*

XPS analyses were carried out with a PHI VersaProbe 4 instrument using a nonmonochromatic Mg K $\alpha$  source (1253.6 eV). Using a Mg source over a traditional Al source is critical to prevent the overlap between Ni LMM Auger features and Fe 2p peaks, which would otherwise make Fe detection impossible.<sup>3</sup> The base pressure of the instrument was  $\sim 10^{-9}$  Torr. High-resolution spectra were collected over an analysis area of  $\sim 250 \times 250 \mu\text{m}^2$  using a pass energy of 10 eV. The charge neutralizer was not employed in post-conditioned samples to prevent partial reduction of the NiOOH phase. Additionally, Ar<sup>+</sup> sputtering was conducted for 30 s on one NF-NiOOH electrode sample to investigate its impact on the reduction of the NiOOH phase (see **Figure S27**). Samples containing other transition metals were analyzed without Ar<sup>+</sup> sputtering. Binding energy calibration was carried out using the C 1s peak for adventitious hydrocarbons at 284.8 eV. Data analysis was performed using CasaXPS software. The spectral fitting parameters for the C 1s, O 1s, Ni 2p, Fe 2p, and Co 2p peaks were adopted from previous studies.<sup>27–29</sup> Fitting components were modeled using a combination of Gaussian (70%) and Lorentzian (30%) profiles, denoted as GL(30) in CasaXPS. For fitting the spectra of transition metal peaks, a standard Shirley-type baseline was employed. This baseline featured variable offset levels at the high binding energy endpoint.

For sample preparation, the methodology was consistent with that used for EELS samples. Immediately after electrochemical conditioning, the electrodes were immersed in N<sub>2</sub>-purged DI water to remove residual KOH electrolyte. A circular section with a diameter of ~3 mm was excised from the electrode and situated atop an Al crucible with a droplet of DI water. This assemblage was then placed on the XPS holder and dried through repeated cycling between atmospheric pressure and low vacuum (>50 Torr), facilitated by a sorption pump. After drying, the chamber was evacuated to a high vacuum and transferred to the main XPS analysis chamber. This procedure was followed to minimize contamination and mitigate surface exposure to air post-conditioning.

#### *Raman spectroscopy*

Measurements were performed in a Horiba LabRAM ARAMIS confocal Raman microscope equipped with a 100× magnification objective. Two lasers at 532 and 633 nm were employed at 50% of their total power with a spot size of approximately 1 μm. Each spectrum was recorded at a 1 cm<sup>-1</sup> resolution by averaging three scans, each lasting 60 s. At least three locations on each sample were examined, and the resulting spectra were averaged. A calibration check against a value of 520.7 cm<sup>-1</sup> using a silicon wafer was conducted prior to measurements. Post-conditioned NF-NiOOH electrodes were prepared in the same manner as for TOF-SIMS experiments.

For surface-enhanced Raman spectroscopy (SERS) experiments, thin Ni(OH)<sub>2</sub> films were deposited on screen-printed electrodes (SPE) with Au serving as both working and counter electrodes (Metrohm DropSens, 220BT). First, the Au SPE was electrochemically roughened by placing ~100 μL of 0.1 M KCl solution, saturated with AgCl, onto the SPE. Thirty cyclic voltammetry scans were carried out from -0.3 to 1.3 V vs. Ag at 50 mV·s<sup>-1</sup>. Next, a thin Ni(OH)<sub>2</sub>

film was deposited galvanostatically at a cathodic current of  $-1 \text{ mA}\cdot\text{cm}^{-2}$  for 50 s (total charge:  $50 \text{ mC}\cdot\text{cm}^{-2}$ ). The film was deposited using a two-electrode configuration with the SPE as the working electrode and Ni foam ( $2 \times 2 \text{ cm}^2$  geometric area) as the counter electrode. The SPE was secured to a Ti clip holder, establishing electrical contact exclusively with the SPE's working and counter electrode terminals, thus ensuring film deposition only on the gold surfaces. After the deposition, the films were rinsed with deionized (DI) water and stored in a vacuum oven until further use. Before SERS measurements, the electrodes were aged for one week in purified 1 M KOH electrolyte spiked with transition metals ( $100 \text{ ppb M}^{n+}$ ) and conditioned electrochemically *via* CP @  $1 \text{ mA}\cdot\text{cm}^{-2}$  for 5 min. The resulting electrocatalyst consisted of a thin NiOOH film deposited on Au (Au-*t*-NiOOH).

## Supporting Figures and Tables

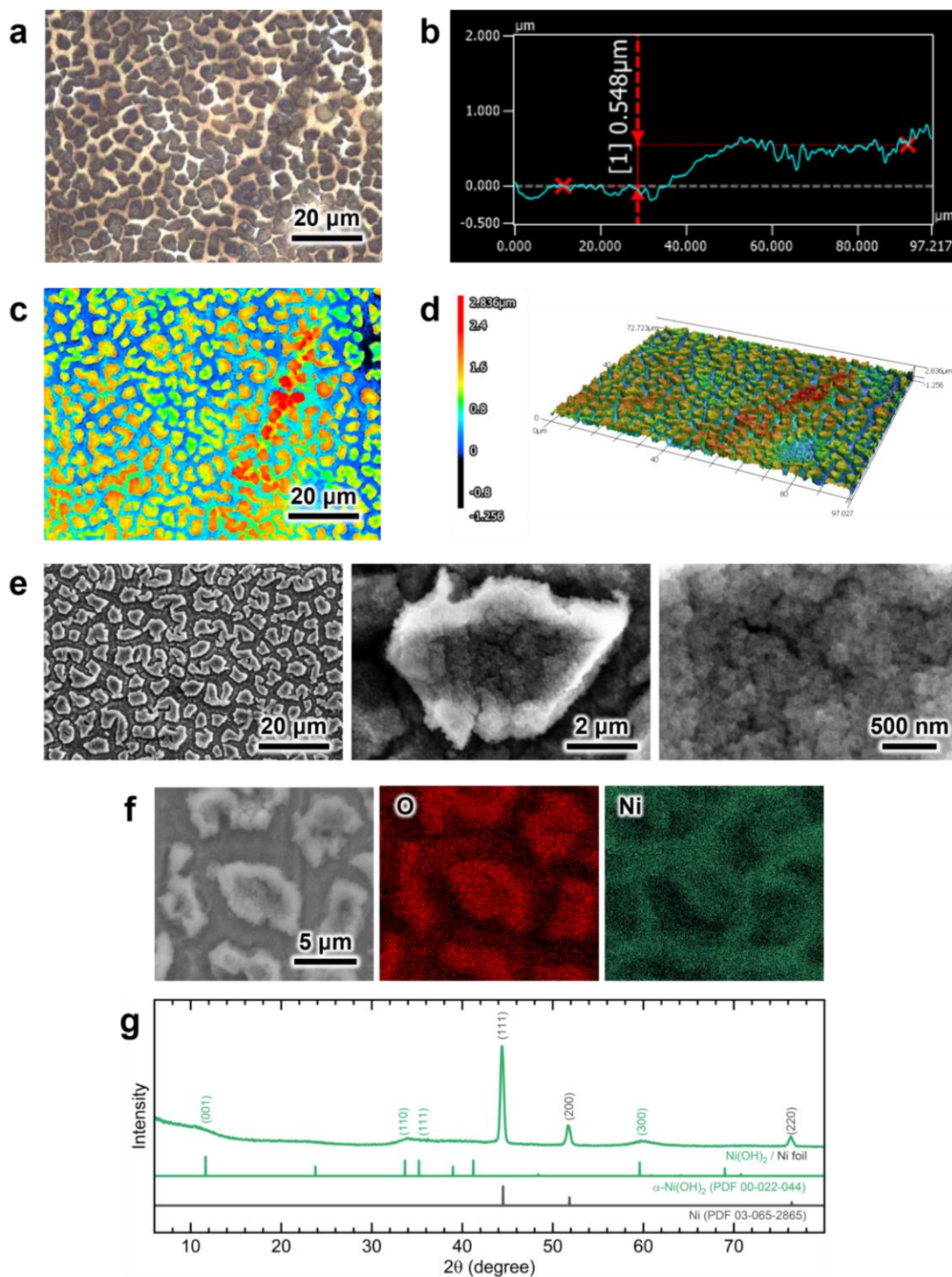


**Figure S3.** Film characterization of the as-deposited NF-Ni(OH)<sub>2</sub> film: (a) NCP optical image, (b) profile graph near the edge of the film with estimated thickness, (c) 2D height-color map, (d) 3D topographic view, (e) SEM images at different magnifications, (f) EDX elemental mapping, (g) GIXRD pattern. The pattern for the Ni foil substrate is shown (in gray) for reference.

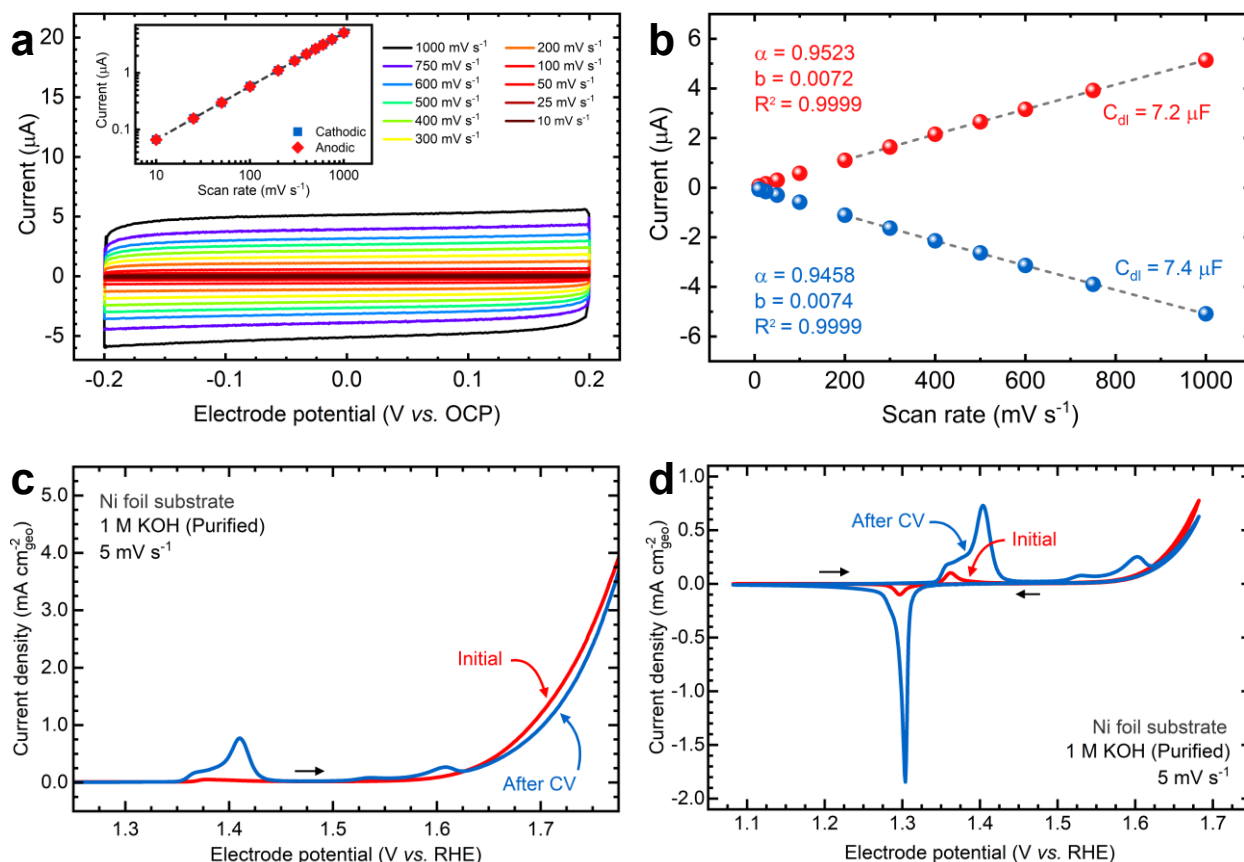


**Figure S4.** Electrochemical characterization of the Ni foil substrate. Estimation of the ECSA in CH<sub>3</sub>CN with 0.15 M KPF<sub>6</sub> electrolyte: (a) CV scans near the OCP and (b) anodic (red) and cathodic (blue) currents (at 0 V vs. OCP) as a function of the scan rate. (c) LSV and (d) CV scans before and after prolonged CV cycling to examine the oxidation resistance of the bare Ni foil substrate.

**Supporting Note:** The average double-layer capacitance ( $C_{dl}$ ) for the Ni foil substrate was determined through three separate measurements and yielded a value of 7.1  $\mu\text{F}$ . Using a specific capacitance value of 11  $\mu\text{F}\cdot\text{cm}^{-2}$  in CH<sub>3</sub>CN/KPF<sub>6</sub> electrolyte,<sup>24</sup> the estimated ECSA is 0.65 cm<sup>2</sup>. Based on geometric area measurements using optical microscopy, the roughness factor is 1.04. Ni foil substrates were cleaned and stored in a vacuum oven at 58 °C for five days prior to  $C_{dl}$  measurements. To examine the substrate's oxidation resistance, CV cycling was conducted following our guidelines.<sup>1</sup> Even after 1600 CV cycles, the redox peak intensities of the Ni foil substrate remained notably lower than those of the electrocatalytic films deposited on Ni foil (see **Figures 1** and **4** in the main manuscript). This result suggests that the Ni foil substrate did not significantly contribute to the observed redox signals after film conditioning. Additionally, the OER current decreases after cycling, which is expected to occur in Fe-purified KOH electrolyte.<sup>1,20</sup>

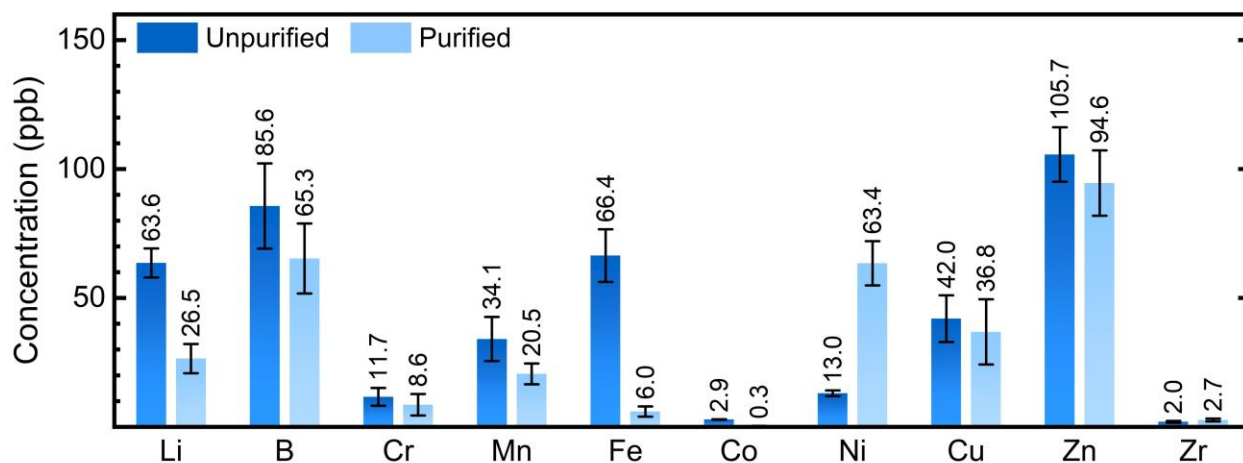


**Figure S5.** Concentrations of the primary elements found in unpurified and purified 1 M KOH electrolytes used in this study. Uncertainty bars indicate the standard deviation derived from five replicate solution-mode ICP-MS measurements.

**Supporting Note:** Our purification process successfully decreases Fe and Co impurity levels, leaving Mn and Cu concentrations unchanged. For tests involving  $\text{Mn}^{2+}$  and  $\text{Cu}^{2+}$  spiked into the KOH electrolyte, the added volume from stock solutions was adjusted to account for existing Mn and Cu in the purified electrolyte. All spiked electrolytes were formulated using the same purified KOH electrolyte, ensuring that overall ion concentration and composition remained consistent, with only the spiked cation varying.

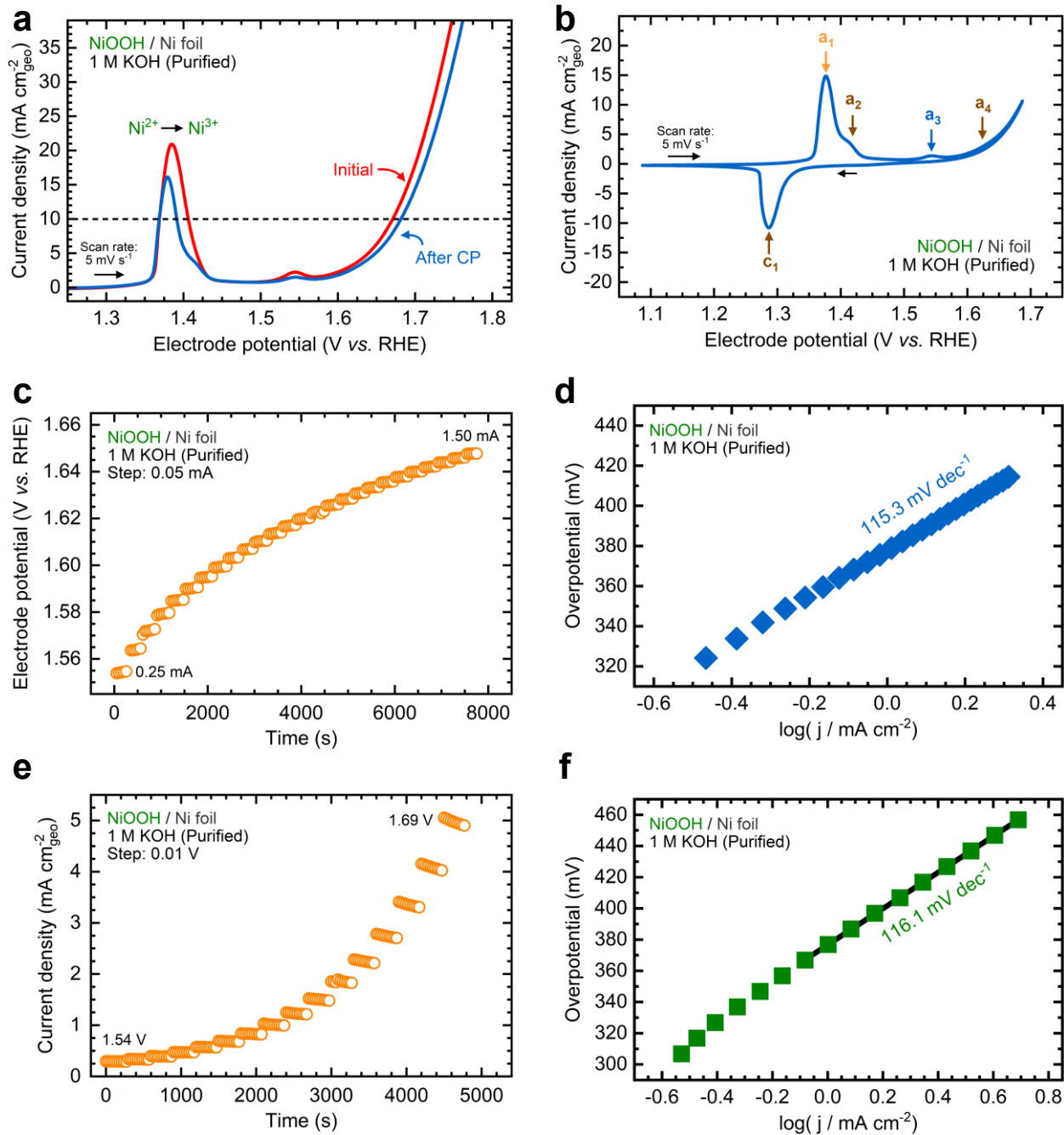


**Figure S6.** Electrochemical characterization of NF-NiOOH electrodes in purified 1 M KOH electrolyte: (a) linear sweep voltammograms before and after CP conditioning, (b) cyclic voltammogram after electrochemical conditioning, (c) multistep chronopotentiometry test near the OER onset, (d) corresponding Tafel plot using data from (c), (e) multistep chronoamperometry test near the OER onset, (f) corresponding Tafel plot using data from (e).

**Supporting Note:** Peaks shown in **Figure S6b** correspond to the Bode scheme of the  $\text{Ni}(\text{OH})_2/\text{NiOOH}$  system.<sup>1</sup> There are four prominent anodic peaks and one cathodic peak. Peaks **a1** and **a3** are attributed to the  $\gamma$ -NiOOH phase, where peak **a1** indicates the oxidation of  $\alpha$ -Ni(OH)<sub>2</sub> to  $\gamma$ -NiOOH. Peak **a3** is associated with the formation of high-valent Ni species, likely NiO<sub>2</sub>.<sup>13,30</sup> Peak **a2** corresponds to the transformation of  $\beta$ -Ni(OH)<sub>2</sub> to the  $\beta$ -NiOOH phase.<sup>3,13</sup> Peak **a4** arises from the decrease in OER current after aging and corresponds to  $\beta$ -NiOOH.<sup>3,13</sup> In the cathodic scan, peak **c1** is attributed to the reduction of  $\gamma$ -NiOOH to  $\alpha$ -Ni(OH)<sub>2</sub>.<sup>30,31</sup> The observed lack of symmetry can be attributed to a minor shoulder resulting from the reduction of  $\beta$ -NiOOH to  $\beta$ -Ni(OH)<sub>2</sub>.<sup>3,13</sup> Moreover, the increase in the intensity of peaks **a3** and **a4** after extended CV cycling (**Figures S11b** and **d**) is attributed to the overcharge of the  $\beta$  phase and transformation of  $\beta$ -NiOOH to  $\gamma$ -NiOOH when the upper potential limit lies beyond 0.7 V vs. Hg/HgO (~1.63 V vs. RHE).<sup>3,13</sup> Thus, the NF-NiOOH electrode, following CP conditioning in Fe-purified 1 M KOH, consists of a mixture of  $\alpha/\gamma$  and  $\beta/\beta$  phases, with the former predominating. Note that the redox peak positions in **Figure S6b** align with the fact that the  $\alpha/\gamma$  phase appears at more negative potentials than the  $\beta/\beta$  phase.<sup>31-34</sup>

**Table S1.** Electrochemical performance of NF-NiMOOH electrodes after electrochemical conditioning in purified 1 M KOH electrolyte spiked with transition metal cations.

Sample	$\eta$ @ 10* (mV)	EIS $R_{ct}$ ( $\Omega$ )	EIS $C_{dl}$ (mF·cm <sup>-2</sup> )	$E_{onset, OER}$ (V vs. RHE)	Tafel slope** (mV·dec <sup>-1</sup> )	$b$ value	$C_{tot, GCD}^\dagger$ (mF·cm <sup>-2</sup> )	$Q_{eff}^{\dagger\dagger}$ (%)	$C_{ret}^\ddagger$ (%)
NiOOH (Purified KOH)	454.0	8.42 (1.68)	30.39 (1.68)	1.566	114.0	0.557	103.3	99.5	19.3
NiOOH (100 ppb Fe <sup>3+</sup> )	330.5	2.91 (1.58)	32.77 (1.58)	1.446	37.0	0.595	99.6	98.5	13.6
NiOOH (100 ppb Co <sup>2+</sup> )	427.2	4.78 (1.68)	21.92 (1.68)	1.564	80.4	0.548	145.5	98.4	25.3
NiOOH (100 ppb Mn <sup>2+</sup> )	439.7	6.55 (1.68)	25.05 (1.68)	1.566	92.7	0.536	126.7	97.9	18.2
NiOOH (100 ppb Cu <sup>2+</sup> )	448.1	9.74 (1.68)	22.88 (1.68)	1.566	118.9	0.546	105.6	98.6	21.6
NiFeOOH (Purified KOH)	329.8	1.85 (1.58)	17.10 (1.58)	1.466	32.9	0.860	-	-	-
NiCoOOH (Purified KOH)	409.2	4.70 (1.68)	56.2 (1.68)	1.548	68.9	0.686	223.0	99.7	19.98
NiCoOOH (100 ppb Fe <sup>3+</sup> )	330.6	1.66 (1.58)	82.5 (1.58)	1.446	37.2	0.672	139.3	99.6	23.5

The table displays average values calculated from three replicate measurements; for EIS results, values in parenthesis reflect the applied potential (in V vs. RHE);

\*OER overpotential at 10 mA·cm<sup>-2</sup><sub>geo</sub>;

\*\*MUSCA and MUSCP average;

<sup>†</sup> $C_{tot}$ : Total capacitance;

<sup>††</sup> $Q_{eff}$ : Coulombic efficiency;

<sup>‡</sup> $C_{ret}$ : Capacity retention after 1600 GCD cycles.

**Supporting Note:** Measurements of the total capacitance for NiFe(OH)<sub>2</sub> using GCD were not conducted because the Ni<sup>2+/3+</sup> redox peak significantly overlapped with the OER current, compromising the accuracy of these measurements.

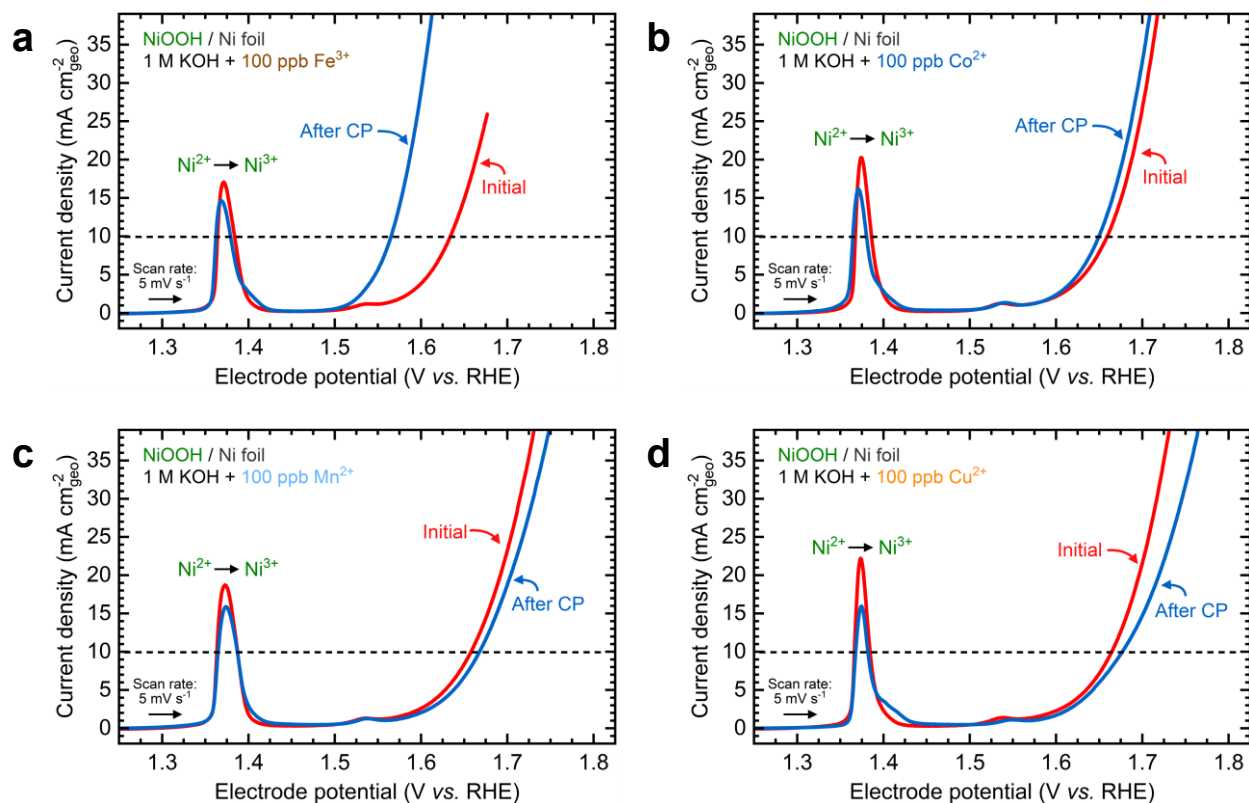


**Figure S7.** Linear sweep voltammograms of NF-NiOOH electrodes before and after CP conditioning in purified 1 M KOH electrolyte spiked with transition metal cations (100 ppb  $M^{n+}$ ): (a)  $Fe^{3+}$ , (b)  $Co^{2+}$ , (c)  $Mn^{2+}$ , and (d)  $Cu^{2+}$ .

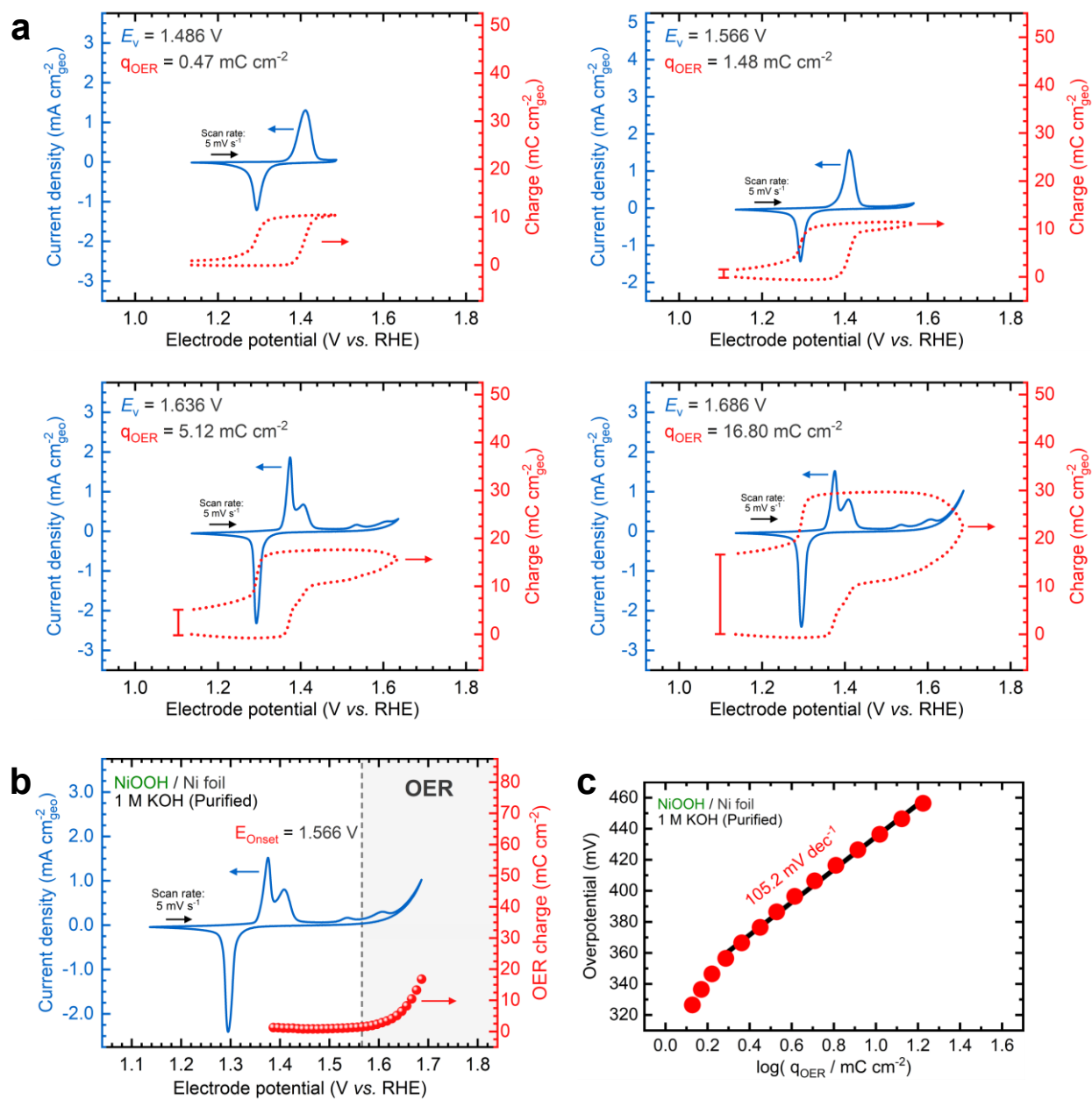


**Figure S8.** Coulo Voltammetry analysis of the OER onset potential and Tafel slope of NF-*t*-NiOOH electrodes after CP conditioning in purified 1 M KOH electrolyte: (a) CV scans along with electric charge plots at varying vertex potentials, (b) CV and electric charge plot depicting the OER charge across the vertex potential range, and (c) Tafel slope calculation based on the OER charge values close to the OER onset.

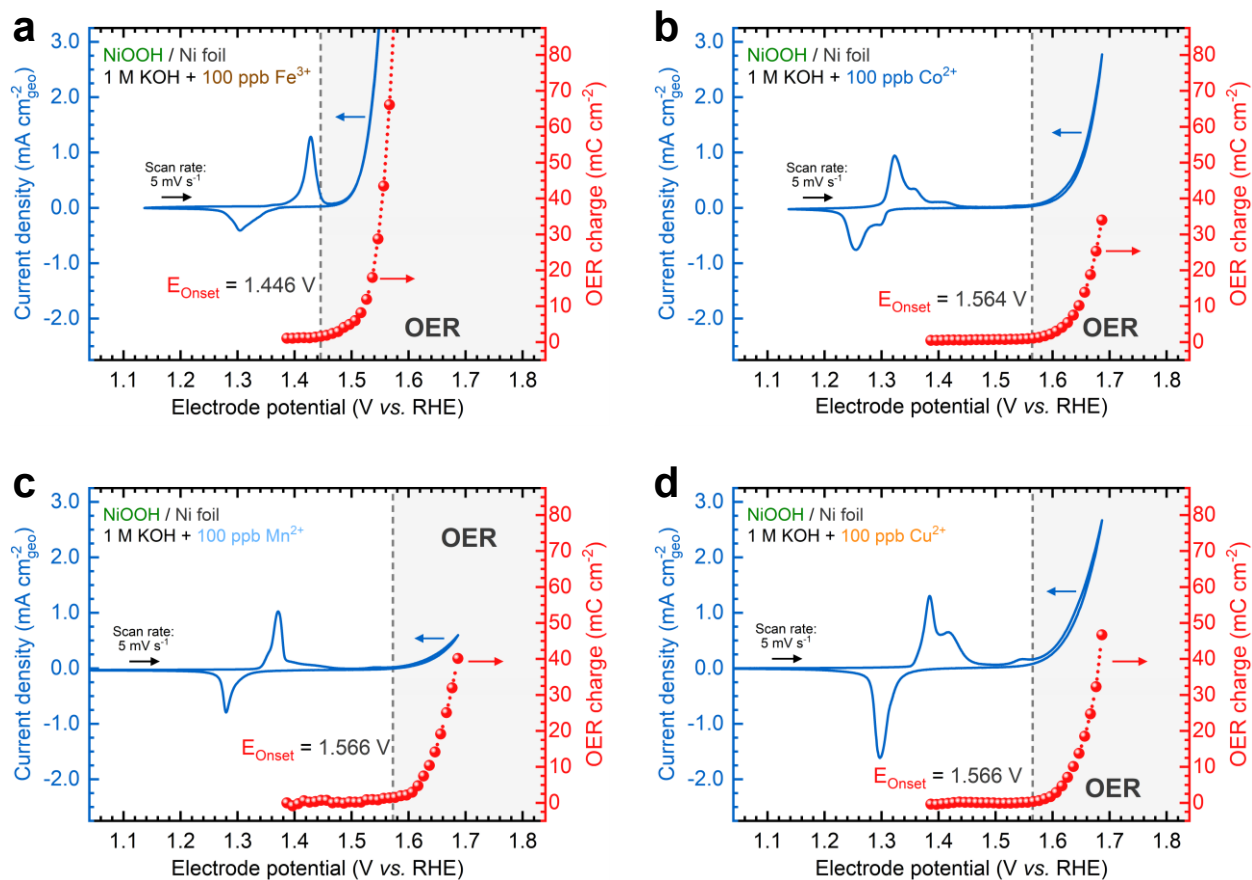


**Figure S9.** Coulovoltammetry plots showing the OER onset of NF-*t*-NiOOH electrodes after CP conditioning in purified 1 M KOH electrolyte spiked with transition metal cations (100 ppb  $M^{n+}$ ): (a)  $Fe^{3+}$ , (b)  $Co^{2+}$ , (c)  $Mn^{2+}$ , and (d)  $Cu^{2+}$ .

**Supporting Note:** We acknowledge the challenge of comparing results obtained from NF-*t*-NiOOH electrodes used for QV measurements with those from thicker NF-NiOOH electrodes. As previously mentioned, we employed thin films to reduce charge-trapping effects during continuous CV cycling. Note, however, that QV measurements were solely conducted to provide an initial estimate of the full charge potential ( $E_{fc}$ ), which was then used to optimize the potential window during GCD cycling. Then, we optimized the  $E_{fc}$  value through coulombic efficiency results (see **Figure S11** and **Tables S1** and **S2**) to minimize OER contributions to the charge-discharge profiles and capacitance estimations from GCD conditioning. QV measurements using thin NiOOH films only provide an initial assessment of the OER onset and do not affect our interpretation of GCD conditioning results.

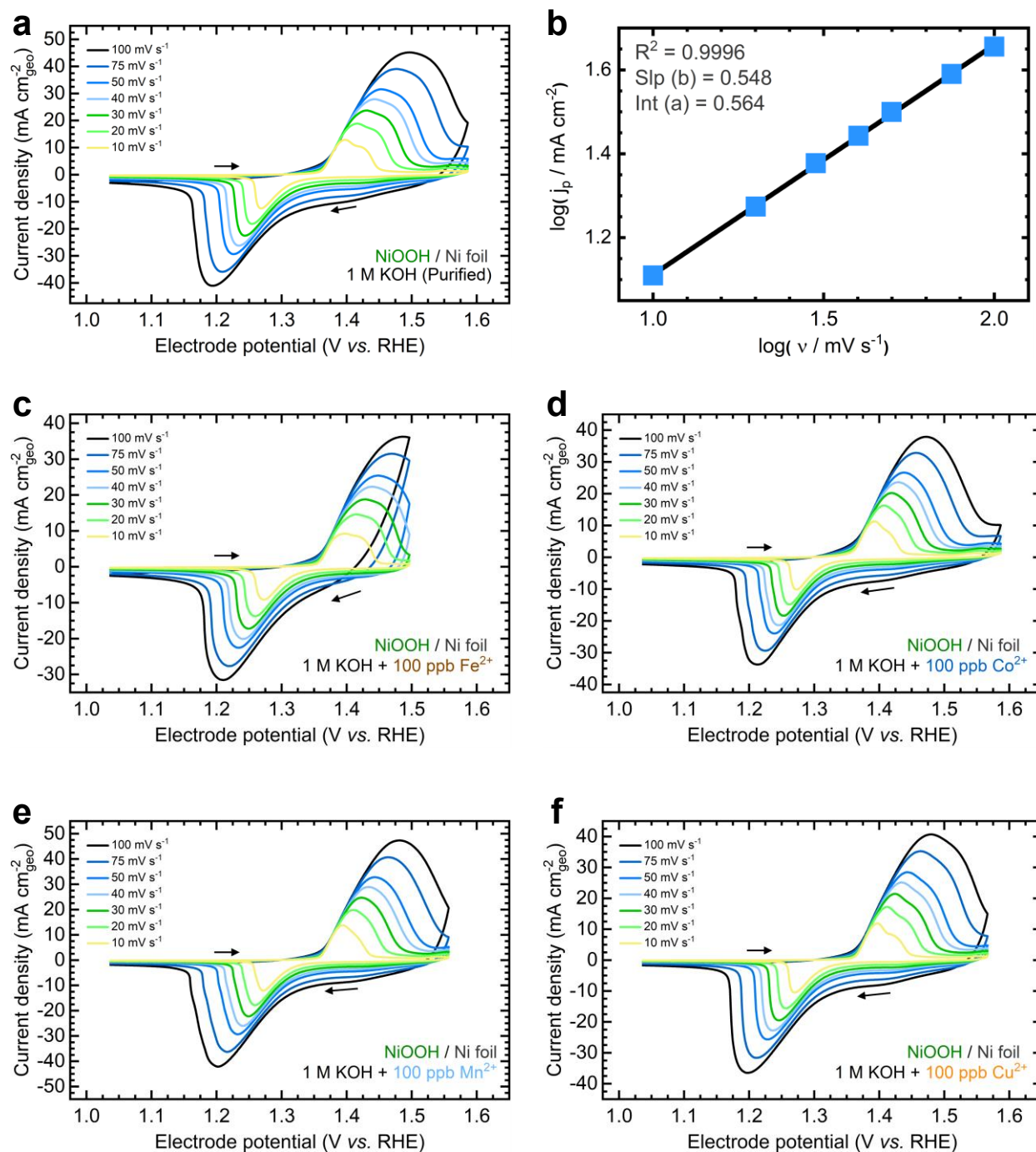


**Figure S10.** Energy storage properties of NF-NiOOH electrodes: (a) CV scans at varying scan rates after CP conditioning in purified 1 M KOH electrolyte, (b) linear dependence of the anodic peak on the scan rate; CV scans after CP conditioning in purified 1 M KOH electrolyte spiked with transition metal cations (100 ppb M<sup>n+</sup>): (c) Fe<sup>3+</sup>, (d) Co<sup>2+</sup>, (e) Mn<sup>2+</sup>, and (f) Cu<sup>2+</sup>.

**Supporting Note:** We acknowledge a possible bias in measurements involving Fe-containing KOH, given the noticeable overlap of the OER current with the Ni redox peak. We included these data as the peak potential remained distinguishable below 100 mV·s<sup>-1</sup>.

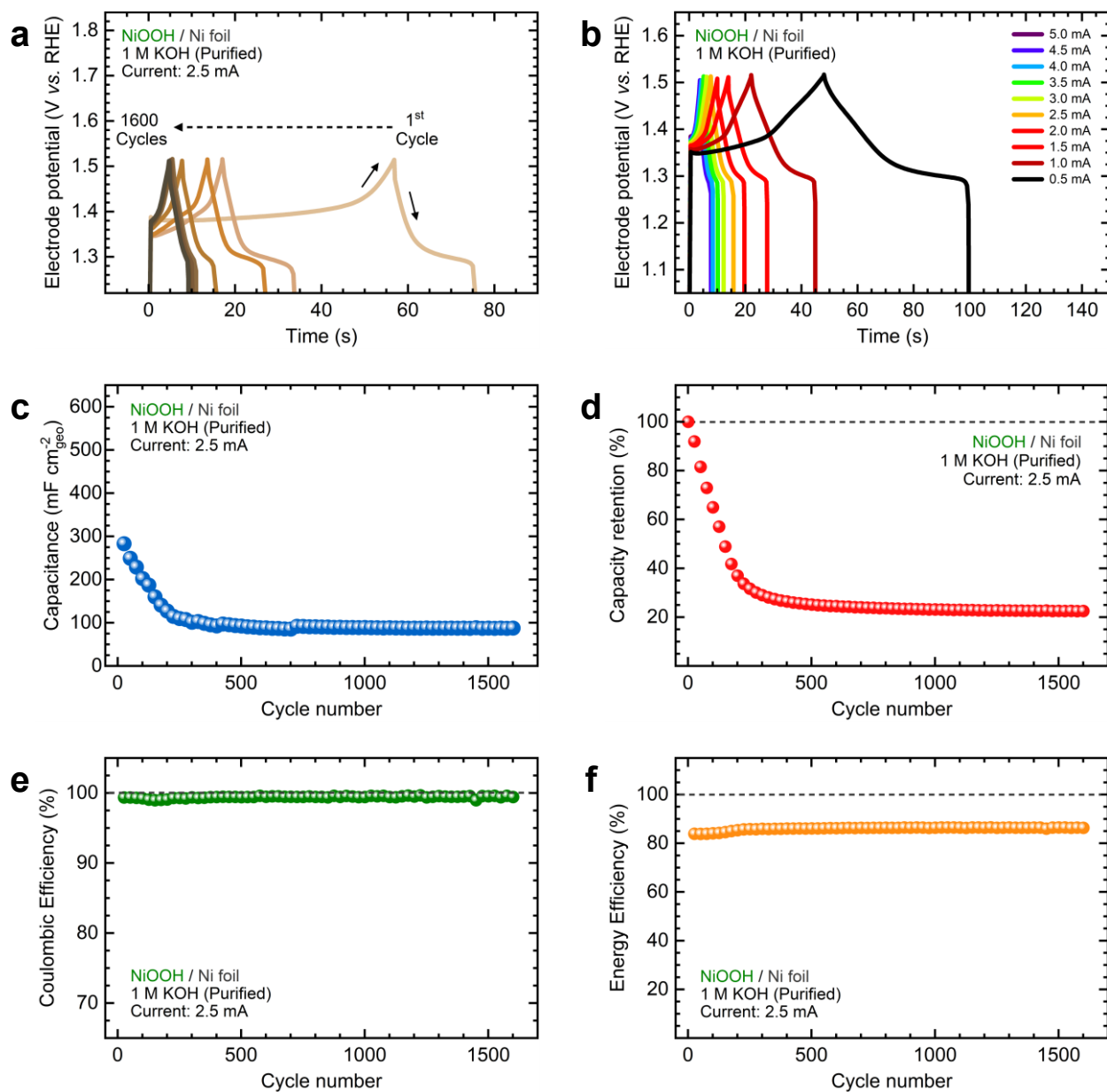


**Figure S11.** Energy storage properties of NF-NiOOH electrodes after GCD conditioning in purified 1 M KOH electrolyte: (a) charge-discharge profiles during cycling at a current density of 2.5 mA cm<sup>-2</sup><sub>geo</sub> with one profile taken every 200 cycles, (b) charge-discharge profiles across various currents, (c) total capacitance, (d) capacity retention, (e) coulombic efficiency, and (f) energy efficiency over repeated cycles.

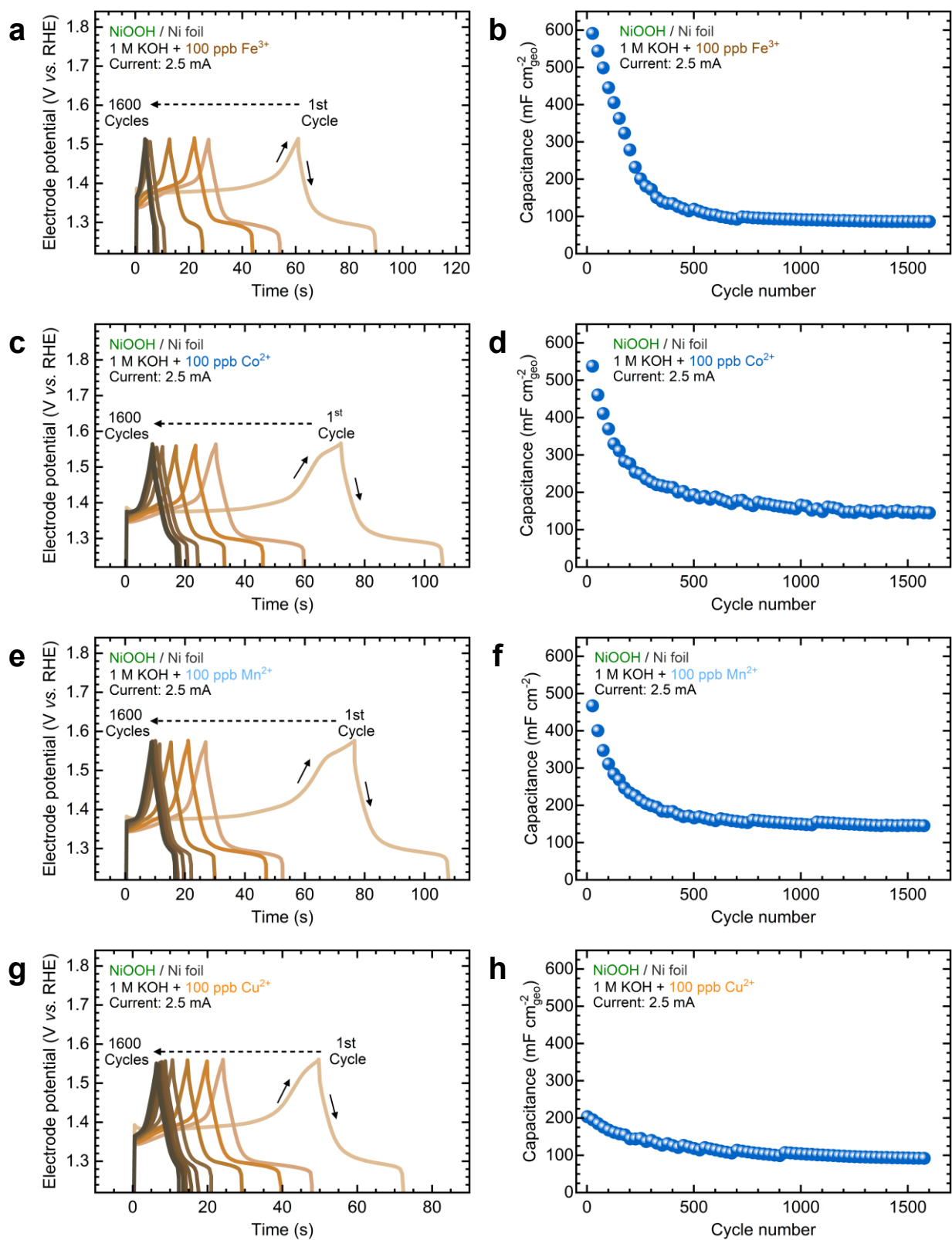


**Figure S12.** Charge-discharge profiles (a, c, e, g) and total capacitance over repeated cycles (b, d, f, h) of NF-NiOOH electrodes during GCD conditioning in purified 1 M KOH electrolyte spiked with transition metal cations (100 ppb M<sup>n+</sup>): (a, b) Fe<sup>3+</sup>, (c, d) Co<sup>2+</sup>, (e, f) Mn<sup>2+</sup>, and (g, h) Cu<sup>2+</sup>.

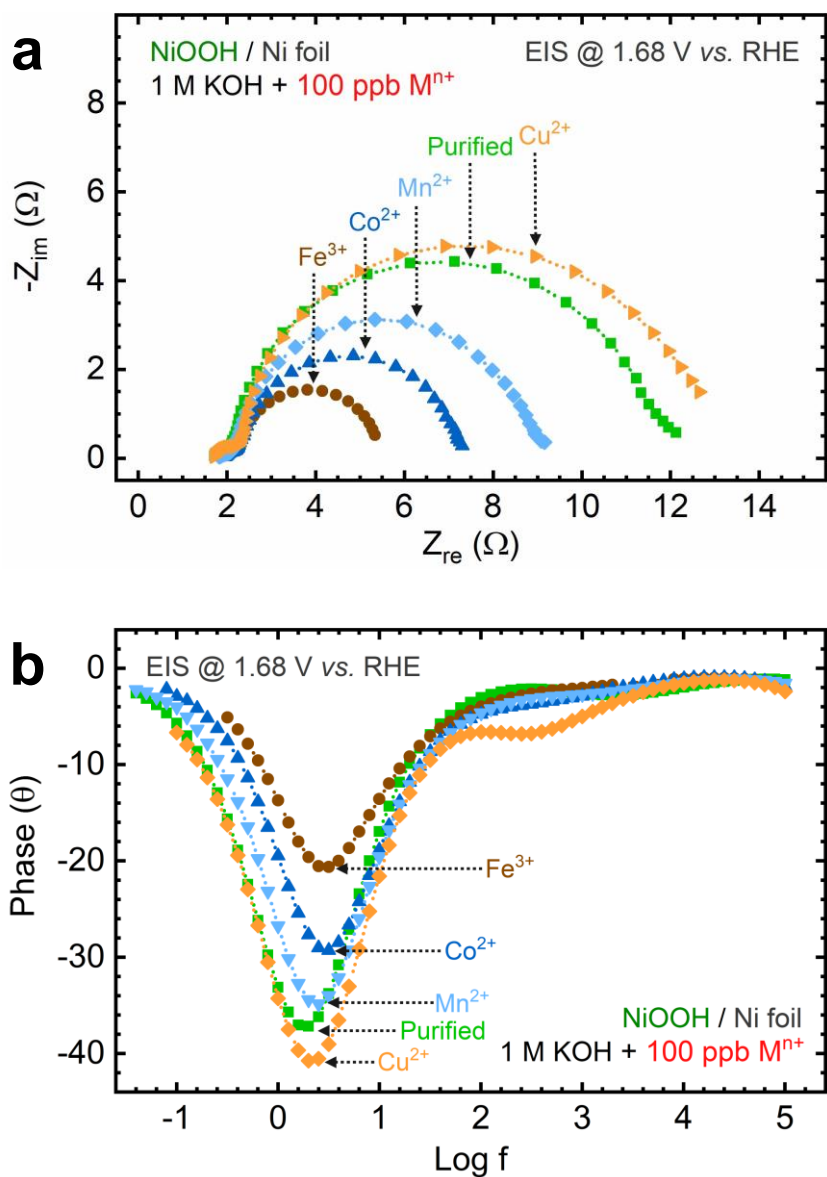


**Figure S13.** EIS analysis of NF-NiOOH electrodes after CP conditioning in purified 1 M KOH electrolyte spiked with transition metal cations (100 ppb  $M^{n+}$ ): (a) Nyquist plots, (c) Bode plots.

**Supporting Note:** The Nyquist plots in **Figure S13a** feature two semicircles. The higher-frequency semicircle is associated with the contact impedance between the working electrode and the titanium clip.<sup>22</sup> The prominent lower-frequency semicircle results from the electrochemical interactions at the interface between the electrocatalyst and the electrolyte. The equivalent circuit corresponding to this system is shown in **Figure S2**.

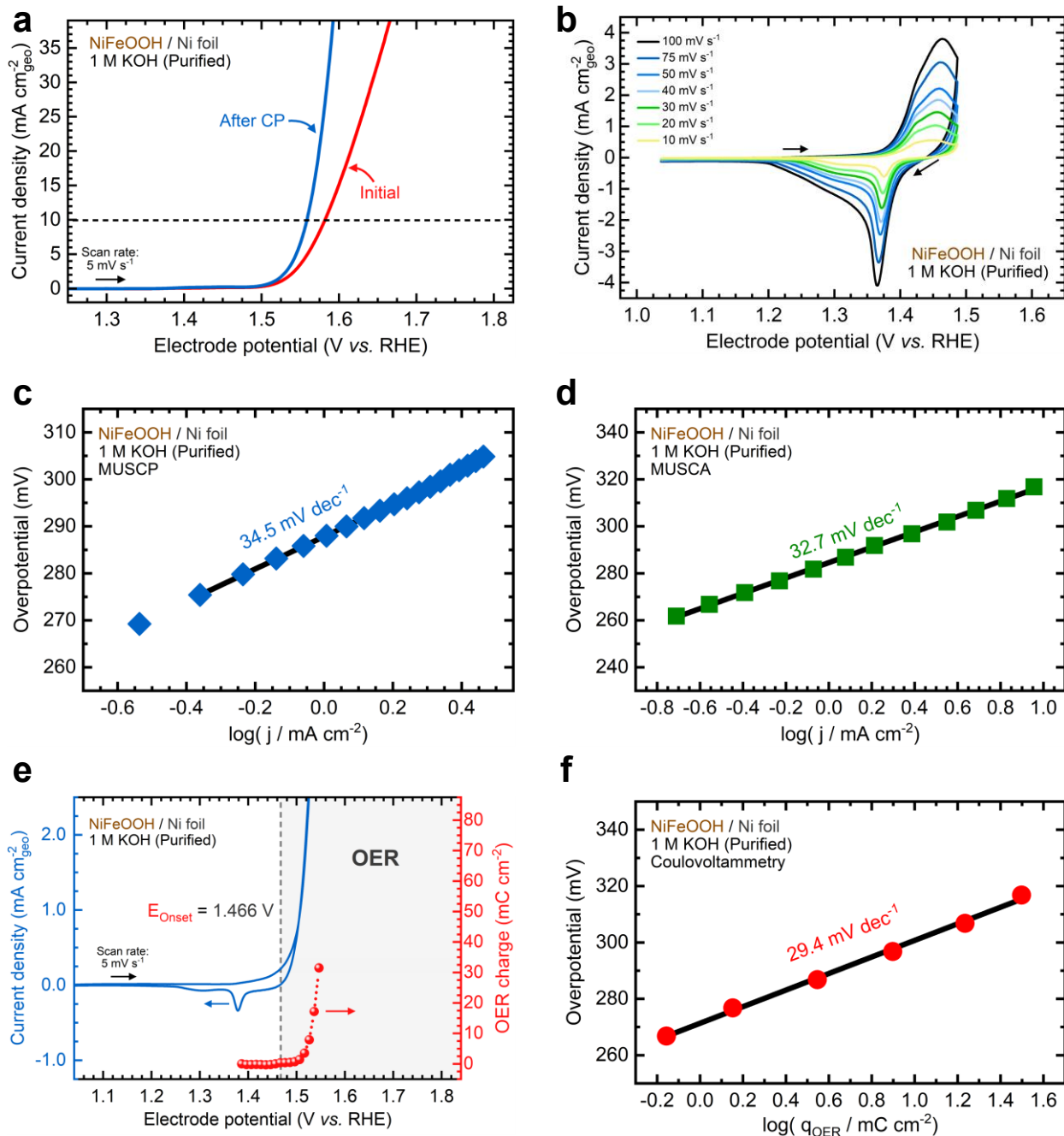


**Figure S14.** Electrochemical characterization of NF-NiFeOOH electrodes after CP conditioning in purified 1 M KOH electrolyte: (a) linear sweep voltammograms before and after electrochemical conditioning, (b) CV scans from 10 to 100 mV·s<sup>-1</sup>, (c) Tafel slope from multistep chronopotentiometry, (d) Tafel slope from multistep chronoamperometry, (e) coulovoltammogram plot, and (f) Tafel slope from coulovoltammometry analysis.

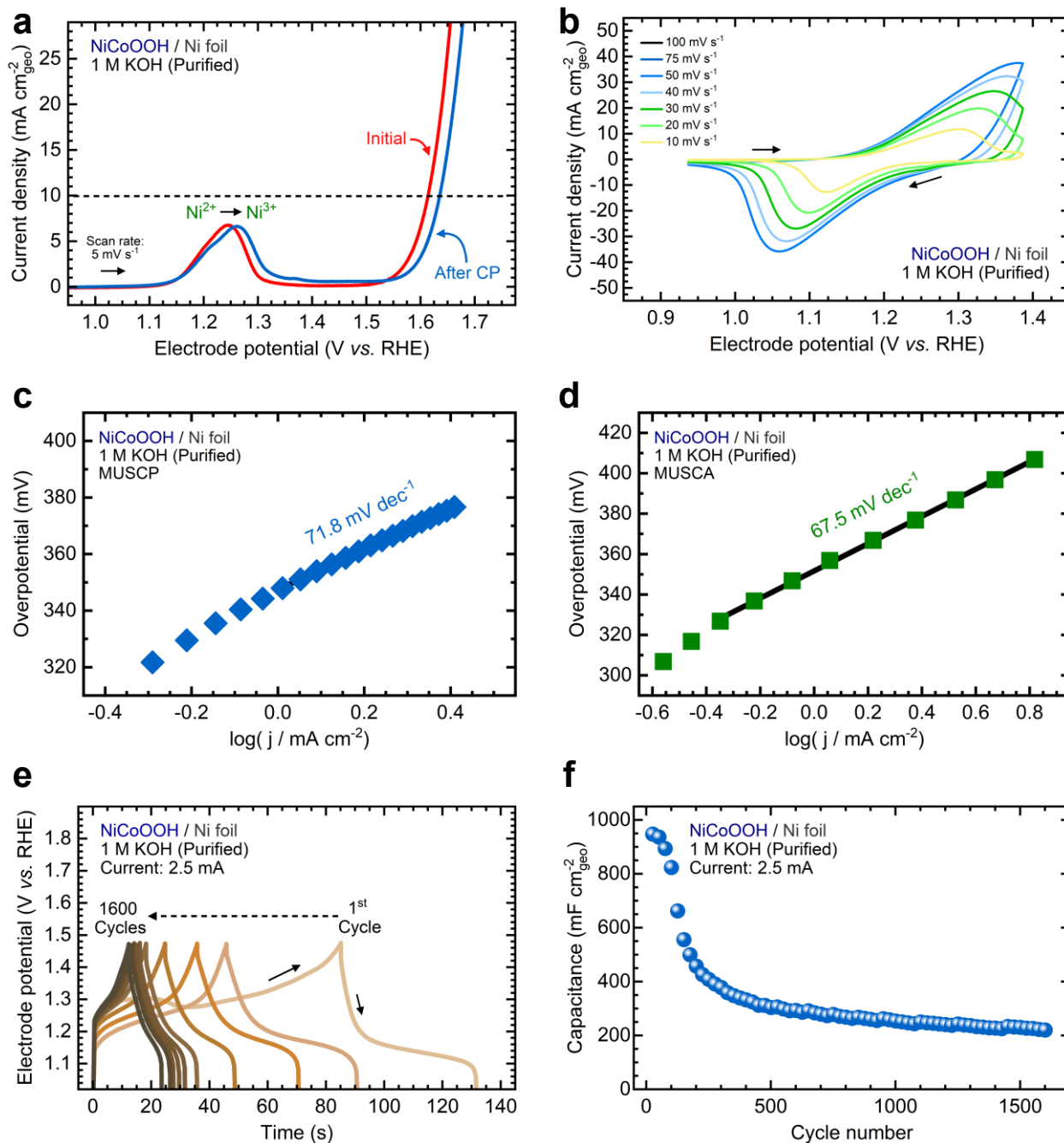


**Figure S15.** Electrochemical characterization of NF-NiCoOOH electrodes after CP conditioning in purified 1 M KOH electrolyte: (a) linear sweep voltammograms before and after electrochemical conditioning, (b) CV scans from 10 to 100  $\text{mV}\cdot\text{s}^{-1}$ , (c) Tafel slope from multistep chronopotentiometry, (d) Tafel slope from multistep chronoamperometry, (e) galvanostatic charge-discharge profiles during GCD cycling, and (f) capacitance over repeated cycles.

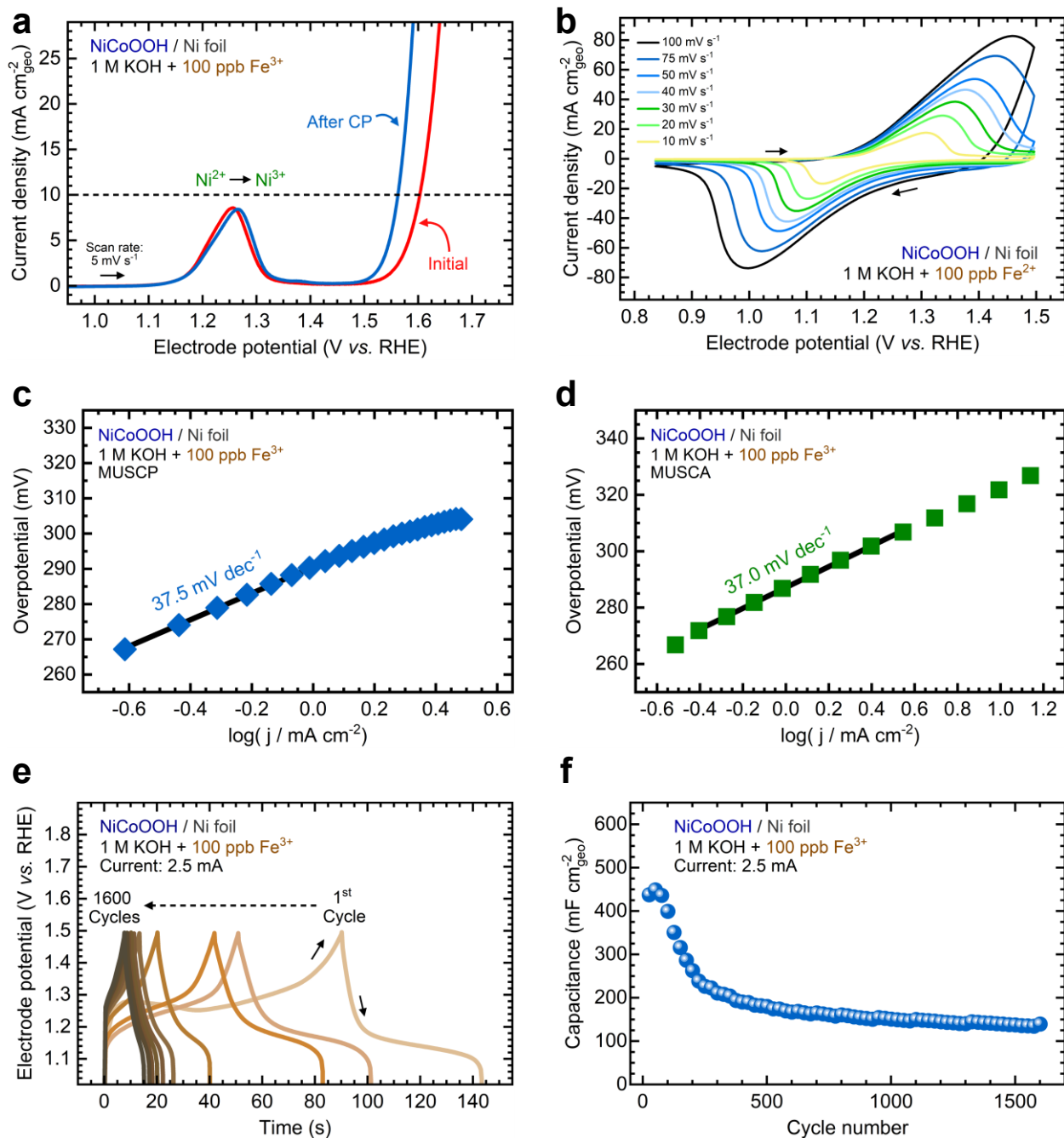


**Figure S16.** Electrochemical characterization of NF-NiCoOOH electrodes after CP conditioning in purified 1 M KOH electrolyte spiked with 100 ppb  $\text{Fe}^{3+}$ : (a) linear sweep voltammograms before and after electrochemical conditioning, (b) CV scans from 10 to 100  $\text{mV}\cdot\text{s}^{-1}$ , (c) Tafel slope from multistep chronopotentiometry, (d) Tafel slope from multistep chronoamperometry, (e) galvanostatic charge-discharge profiles during cycling, and (f) capacitance over repeated cycles.

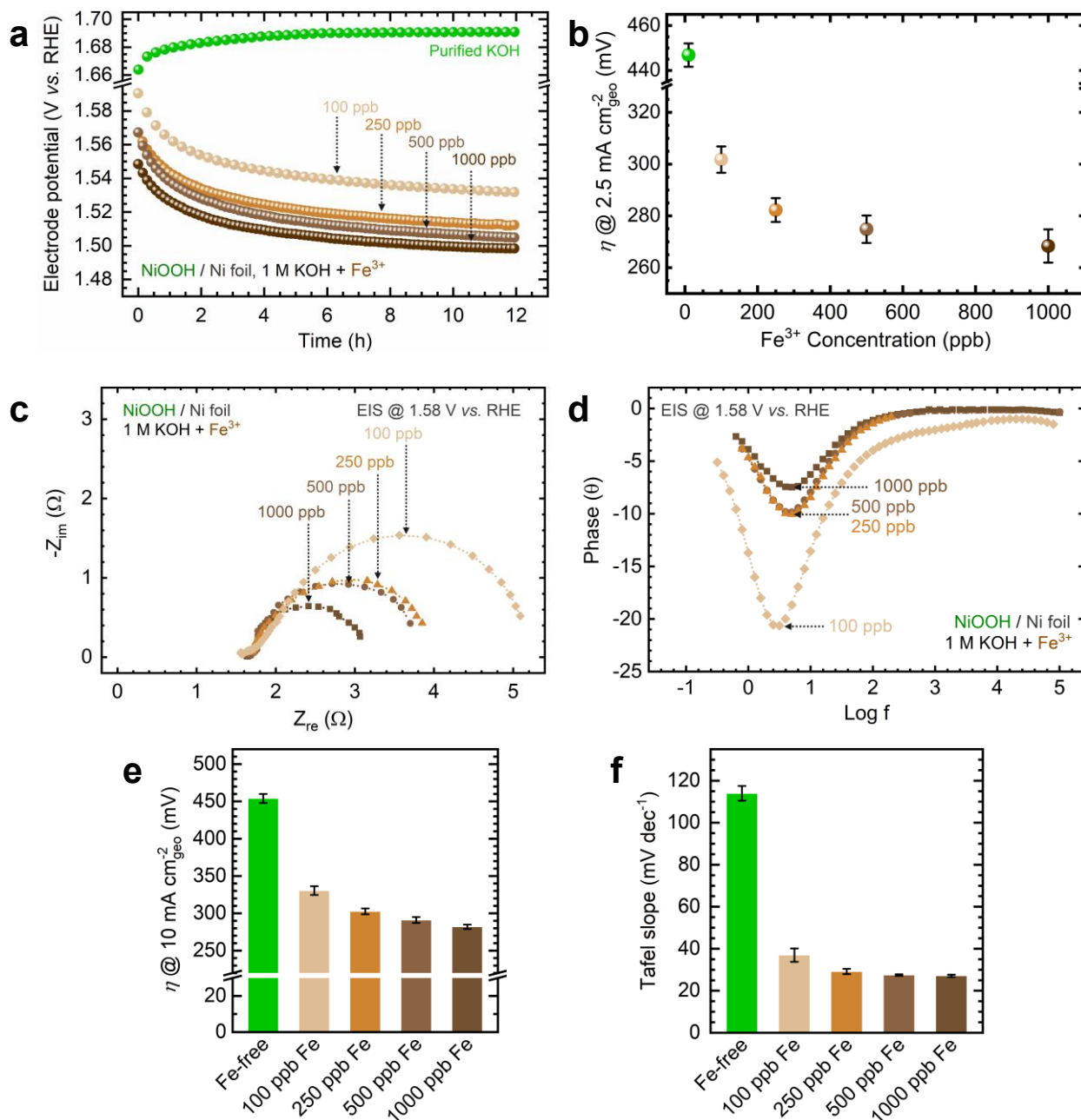


**Figure S17.** Electrochemical performance of NF-NiOOH electrodes conditioned in purified 1 M KOH electrolyte spiked with increasing Fe<sup>3+</sup> concentrations: (a) CP conditioning curves at 2.5 mA·cm<sup>-2</sup>geo, (b) OER overpotentials at 2.5 mA·cm<sup>-2</sup>geo with increasing Fe<sup>3+</sup> concentration, (c) Nyquist and (d) Bode plots from EIS analysis, (e) OER overpotentials at 10 mA·cm<sup>-2</sup>geo and (f) average Tafel slopes with increasing Fe<sup>3+</sup> concentration. Uncertainty bars indicate the standard deviation derived from three replicate measurements.

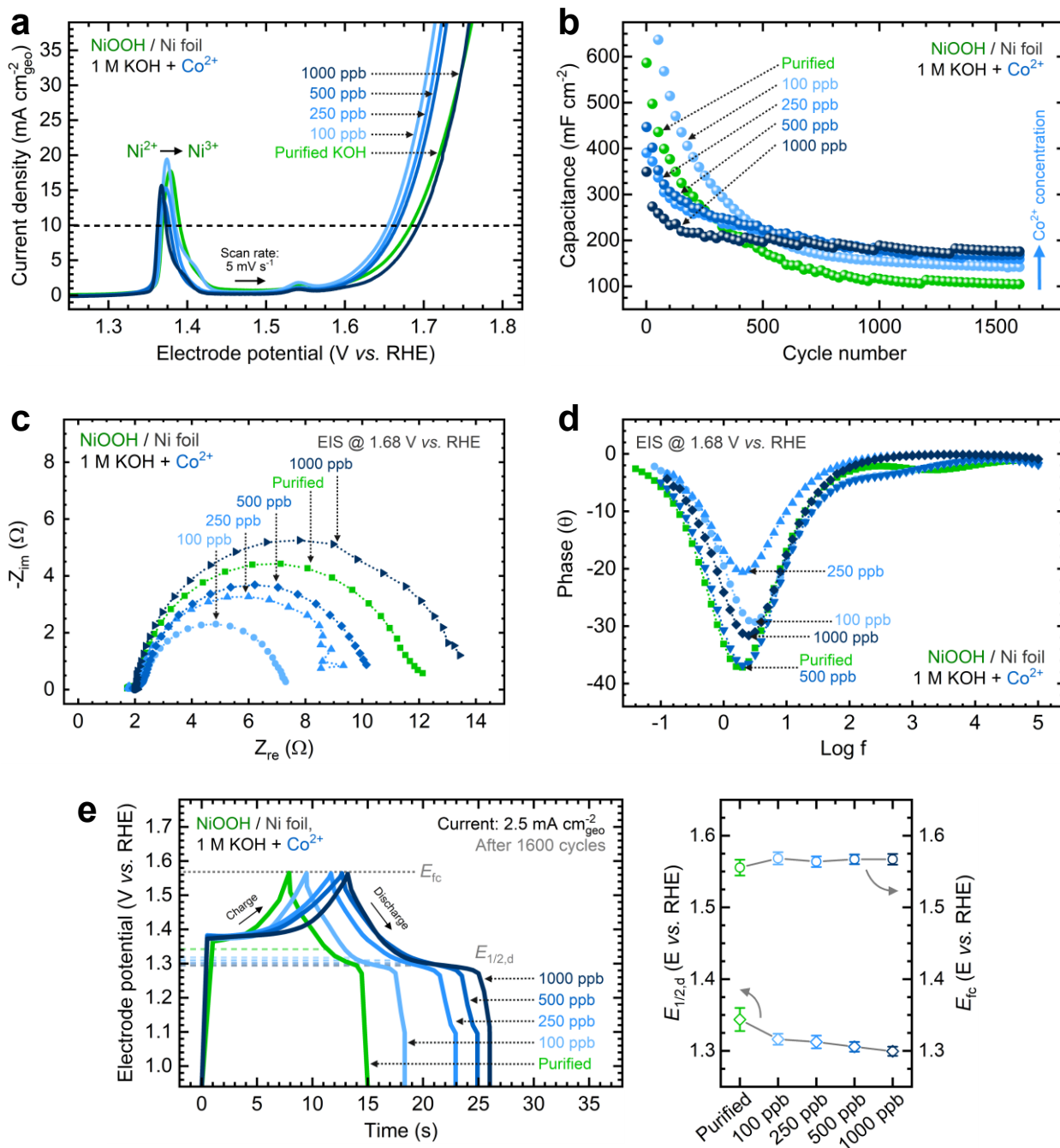


**Figure S18.** Electrochemical performance of NF-NiOOH electrodes conditioned in purified 1 M KOH electrolyte spiked with increasing Co<sup>2+</sup> concentrations: (a) liner sweep voltammograms, (b) total capacitance over multiple cycles, (c) Nyquist and (d) Bode plots from EIS analysis, (e) galvanostatic charge-discharge profiles at 2.5 mA·cm<sup>-2</sup><sub>geo.</sub> along with corresponding half-discharge and full-charge potential values at increasing Co<sup>2+</sup> concentrations. Uncertainty bars indicate the standard deviation derived from three replicate measurements.

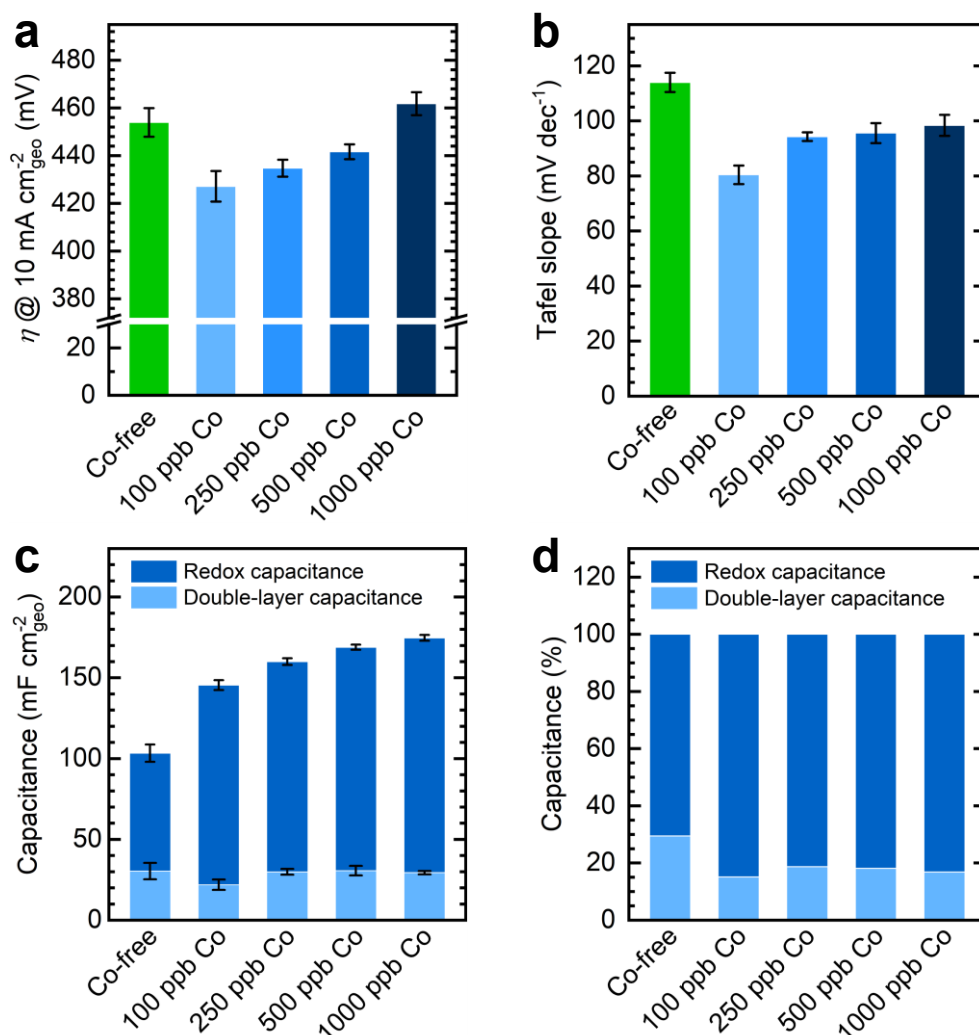


**Figure S19.** Observed trends of different electrochemical parameters for NF-NiOOH electrodes after conditioning in purified 1 M KOH electrolyte spiked with increasing Co<sup>2+</sup> concentrations: (a) OER overpotentials at 10 mA·cm<sup>-2</sup><sub>geo</sub>, (b) average Tafel slopes, (c) total and (d) relative capacitance contributions estimated from EIS and GCD measurements. Uncertainty bars indicate the standard deviation derived from three replicate measurements.

**Supporting Note:** The height of the bars shown in **Figure S19c** represents the total capacitance measured from GCD conditioning. The  $C_{dl}$ , determined from EIS analysis, was subtracted from the total capacitance to estimate the redox capacitance. **Figure S19d** shows the relative contributions of  $C_{dl}$  and  $C_{redox}$  to the total capacitance.

**Table S2.** Electrochemical performance of NF-NiMOOH electrodes after electrochemical conditioning in purified 1 M KOH electrolyte spiked with increasing Fe<sup>3+</sup> and Co<sup>2+</sup> concentrations.

Sample	$\eta$ @ 10* (mV)	EIS R <sub>ct</sub> ( $\Omega$ )	EIS C <sub>dl</sub> (mF·cm <sup>-2</sup> )	E <sub>onset, OER</sub> (V vs. RHE)	Tafel slope** (mV·dec <sup>-1</sup> )	b value	C <sub>tot, GCD</sub> (mF·cm <sup>-2</sup> )	Q <sub>eff</sub> <sup>†</sup> (%)	C <sub>ret</sub> <sup>‡</sup> (%)
NiOOH (Purified KOH)	454.0	8.42 (1.68)	30.39 (1.68)	1.566	114.0	0.557	103.3	99.5	16.3
NiOOH (100 ppb Fe <sup>3+</sup> )	330.5	2.91 (1.58)	32.77 (1.58)	1.446	37.0	0.595	99.6	98.5	13.6
NiOOH (250 ppb Fe <sup>3+</sup> )	302.7	2.13 (1.58)	31.23 (1.58)	1.446	29.2	0.589	-	-	-
NiOOH 500 ppb Fe <sup>3+</sup> )	291.0	1.93 (1.58)	35.47 (1.58)	1.446	27.5	0.605	-	-	-
NiOOH (1000 ppb Fe <sup>3+</sup> )	282.0	1.83 (1.58)	31.84 (1.58)	1.466	27.1	27.1	-	-	-
NiFeOOH (Purified KOH)	329.8	1.85 (1.58)	17.10 (1.58)	1.466	32.9	0.860	-	-	-
NiOOH (100 ppb Co <sup>2+</sup> )	427.2	4.78 (1.68)	21.92 (1.68)	1.564	80.4	0.548	145.5	98.4	18.3
NiOOH (250 ppb Co <sup>2+</sup> )	434.8	5.00 (1.68)	29.87 (1.68)	1.564	94.3	0.546	160.0	98.0	32.5
NiOOH (500 ppb Co <sup>2+</sup> )	441.7	6.57 (1.68)	30.63 (1.68)	1.564	95.6	0.548	168.9	97.5	33.9
NiOOH (1000 ppb Co <sup>2+</sup> )	461.8	11.47 (1.68)	29.38 (1.68)	1.564	98.4	0.529	174.7	98.8	45.4
NiCoOOH (Purified KOH)	409.2	4.70 (1.68)	56.2 (1.68)	1.548	68.9	0.686	223.0	99.7	19.98

The table displays average values calculated from three replicate measurements; for EIS results, values in parenthesis reflect the applied potential (in V vs. RHE);

\*OER overpotential at 10 mA·cm<sup>-2</sup><sub>geo</sub>;

\*\*MUSCA and MUSCP average;

<sup>†</sup>Q<sub>eff</sub>: Coulombic efficiency;

<sup>‡</sup>C<sub>ret</sub>: Capacity retention after 1600 GCD cycles.

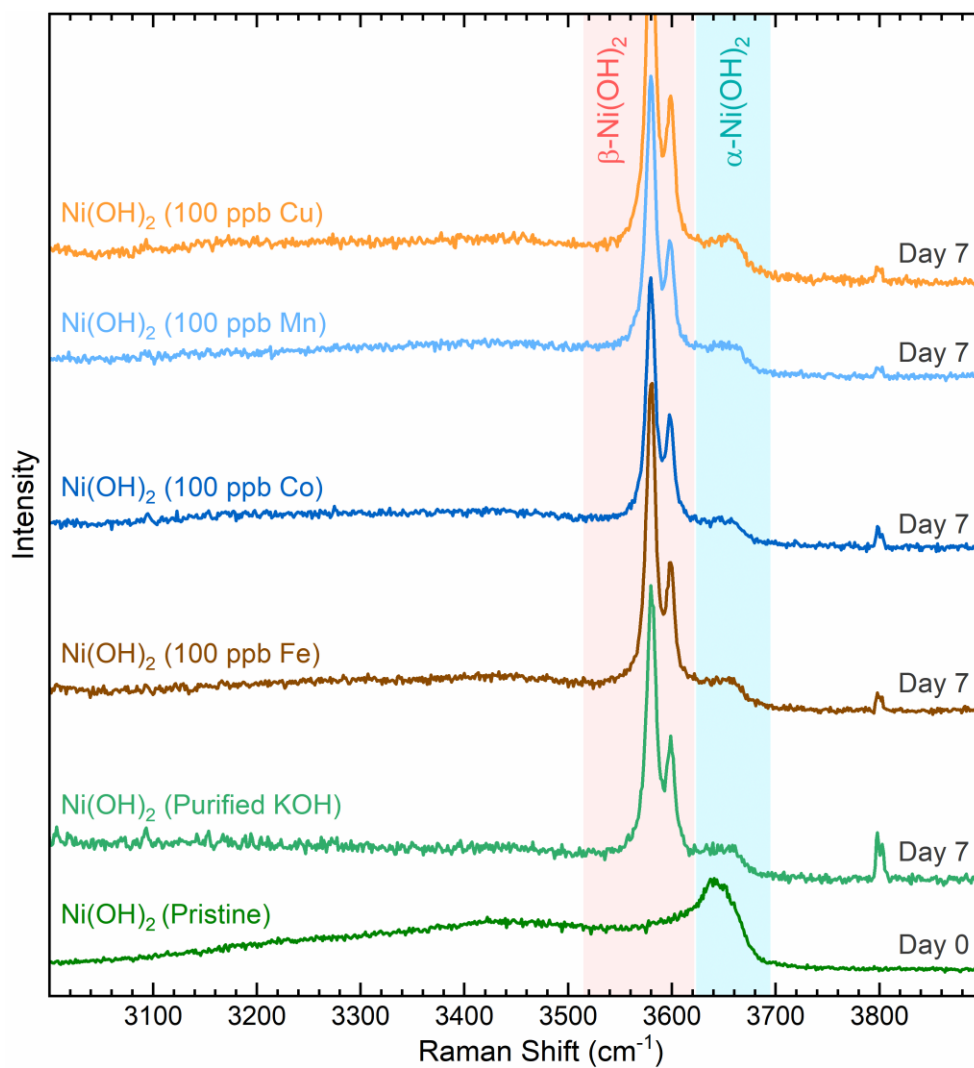


**Figure S20.** Raman spectra of NF-Ni(OH)<sub>2</sub> electrodes after aging for 7 days in purified 1 M KOH electrolyte spiked with transition metal cations (100 ppb M<sup>n+</sup>). A reference spectrum of the as-deposited Ni(OH)<sub>2</sub> film is also included. Spectra are offset on the y-axis for clarity. Laser: 532 nm.

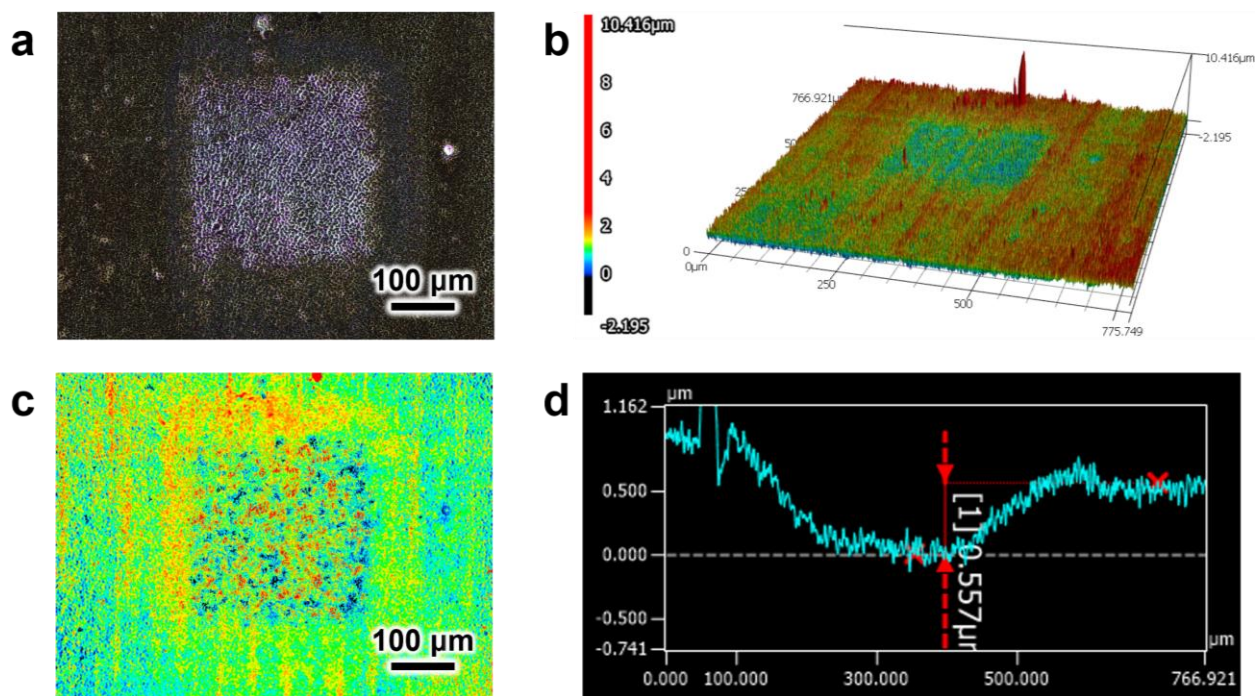


**Figure S21.** Ion sputtering of an NF-NiOOH electrode after CP conditioning in purified 1 M KOH electrolyte spiked with 100 ppb of  $\text{Co}^{2+}$ : (a) optical image, (b) 3D topographic view, and (c) 2D height-color map of the etching crater area ( $300 \times 300 \mu\text{m}^2$ ) created by the  $\text{Cs}^+$  ion sputtering beam; (d) single line scan showing the height difference between the bottom of the etching crater and the surroundings.

**Supporting Note:** We utilized NCP to estimate the average sputtering rate of NiOOH electrocatalytic films during TOF-SIMS analysis in negative polarity ( $\text{Cs}^+$  beam). For the NF-NiOOH +  $\text{Co}^{2+}$  sample, shown in **Figure S21**, the mean depth was calculated to be  $539 \pm 92$  nm based on an average of a hundred line scans in both x and y directions. Given a sputtering time of 9600 seconds for this sample, the resulting sputtering rate is  $0.056 \pm 0.01 \text{ nm}\cdot\text{s}^{-1}$ . We used this sputtering rate to estimate the depths in **Figures 6** and **S22**, as all the films essentially consisted of the same NiOOH composition, thereby having comparable densities.

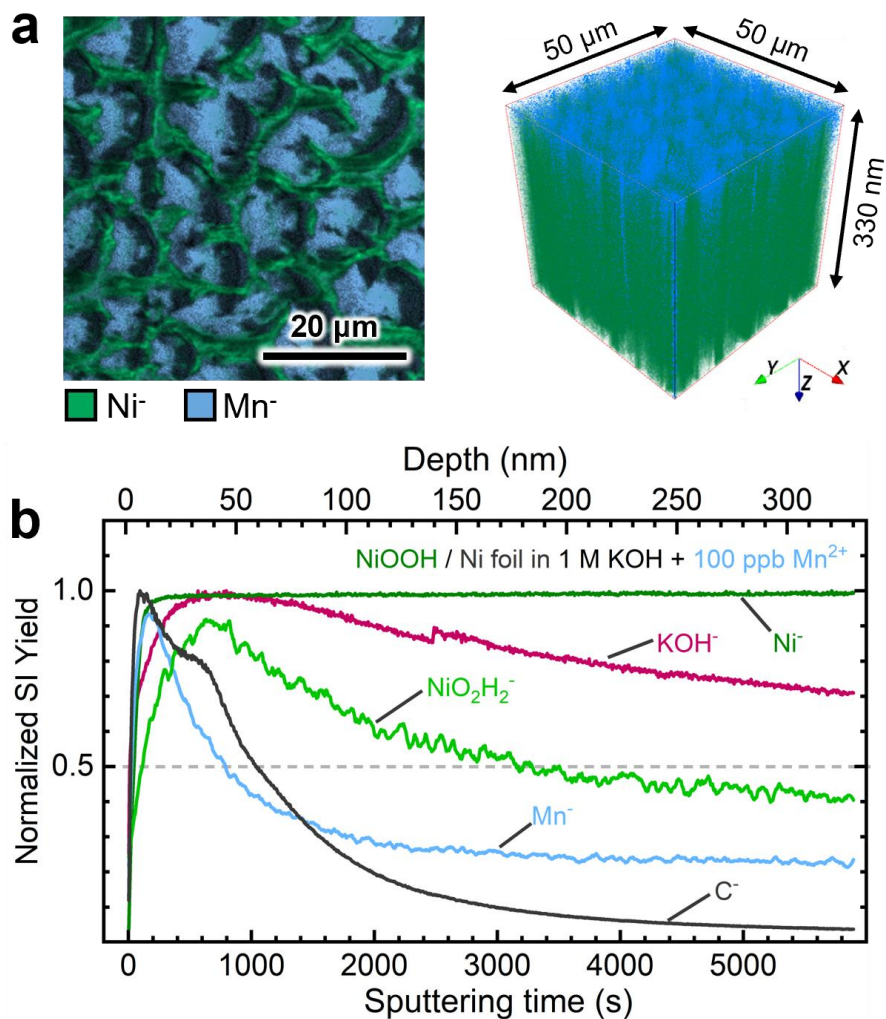


**Figure S22.** TOF-SIMS characterization of an NF-NiOOH electrode after CP conditioning in purified 1 M KOH electrolyte spiked with 100 ppb of  $\text{Mn}^{2+}$ : (a) 2D and 3D mappings showing the spatial distribution of  $\text{Ni}^-$  and  $\text{Mn}^-$  markers and (b) depth profiles (normalized to maximum) of secondary-ion fragments. Data were acquired in negative ion mode. A dashed line at 0.5 is added for reference only.

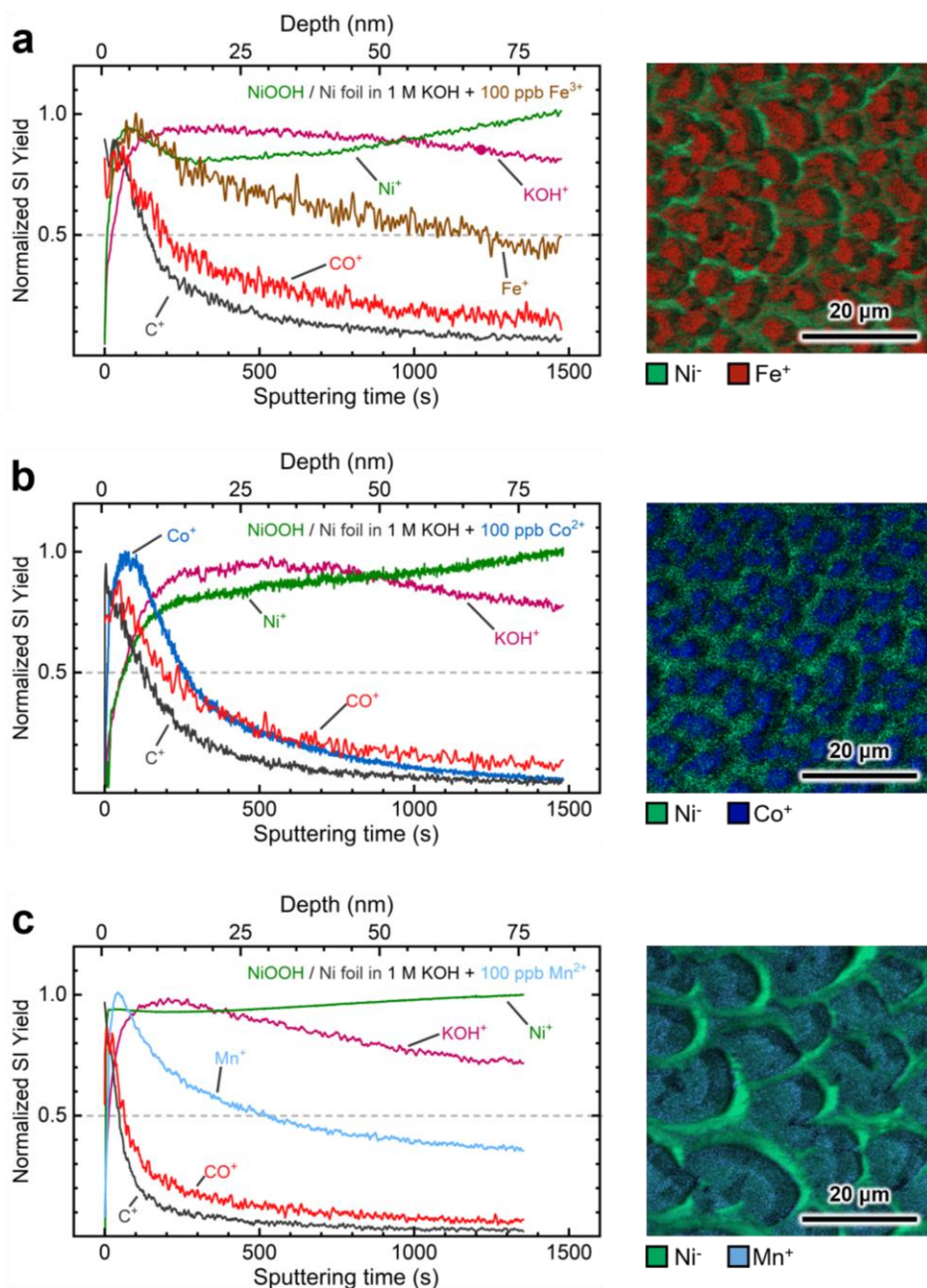


**Figure S23.** TOF-SIMS depth profiles (normalized to maximum) and 2D mappings in positive ion mode of NF-NiOOH electrodes after CP conditioning in purified 1 M KOH electrolyte spiked with 100 ppb of (a) Fe<sup>3+</sup>, (b) Co<sup>2+</sup>, (c) Mn<sup>2+</sup>. A dashed line at 0.5 is added for reference only.

**Supporting Note:** The depths in **Figure S23** were calculated based on the sputtering rate of  $0.056 \pm 0.01 \text{ nm} \cdot \text{s}^{-1}$ , determined under negative polarity. Note that the sputtering rate may differ slightly in positive polarity because it employs an O<sub>2</sub><sup>+</sup> beam instead of Cs<sup>+</sup>. Therefore, all calculations for statistical analysis were conducted using the sputtering time only. The displayed depth serves merely as a point of reference.

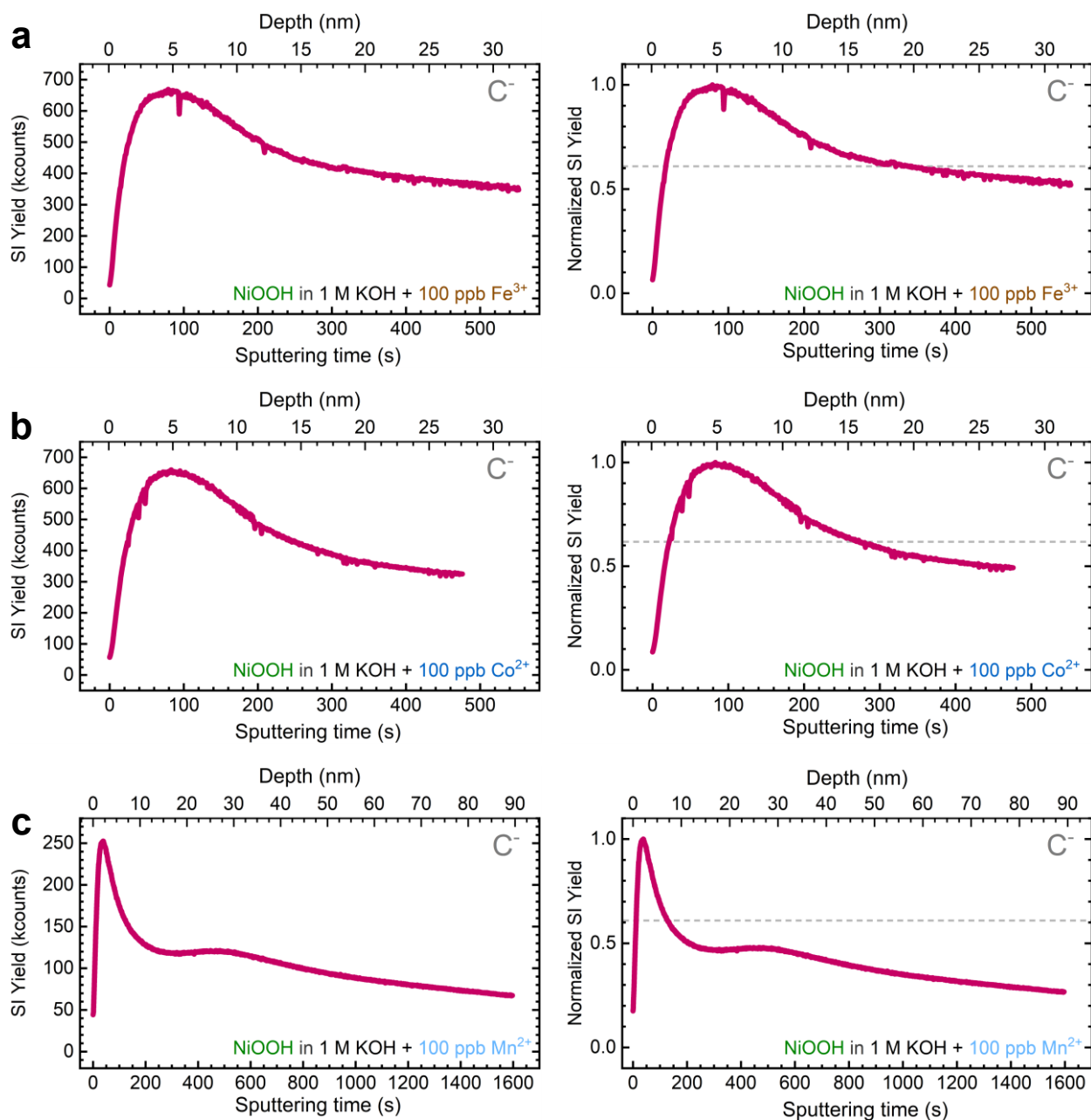


**Figure S24.** TOF-SIMS secondary-ion yield (left) and normalized to maximum (right) depth profiles of the  $C^-$  ion fragment present in NF-NiOOH electrodes after CP conditioning in purified 1 M KOH electrolyte spiked with 100 ppb of (a)  $Fe^{3+}$ , (b)  $Co^{2+}$ , (c)  $Mn^{2+}$ . The dashed line represents an interval estimate in a normal distribution of 68.27% ( $\mu \pm 1\sigma$ ). Data were acquired in negative ion mode.

**Supporting Note:** For TOF-SIMS depth profile statistical analysis, we integrate approximately 68% of the total secondary-ion yield, which falls within one standard deviation of the mean. The dashed line in **Figure S24** represents this line and establishes a range where roughly 68% of the ion fragment's total concentration is found within the depth profile.

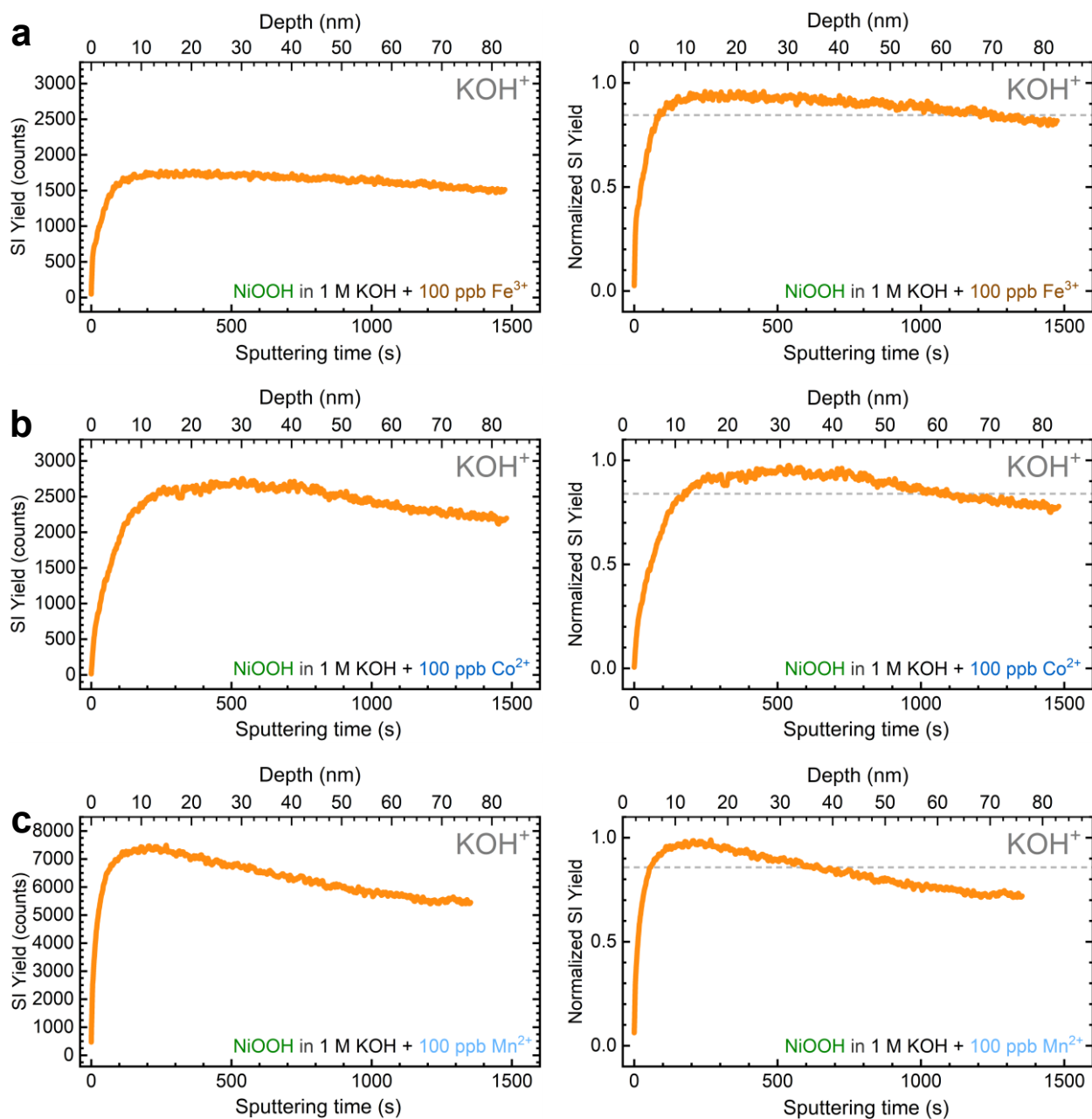


**Figure S25.** TOF-SIMS secondary-ion yield (left) and normalized to maximum (right) depth profiles of the  $\text{KOH}^+$  ion fragment present NF-NiOOH electrodes after CP conditioning in purified 1 M KOH electrolyte spiked with 100 ppb of (a)  $\text{Fe}^{3+}$ , (b)  $\text{Co}^{2+}$ , (c)  $\text{Mn}^{2+}$ . The dashed line represents an interval estimate in a normal distribution of 86.64% ( $\mu \pm 1.5\sigma$ ). Data were acquired in positive ion mode.

**Supporting Note:** Unlike **Figure S25**, we integrate approximately 87% (*i.e.*,  $\mu \pm 1.5\sigma$ ) of the total secondary-ion yield rather than 68%, as the normalized intensity never drops below 0.7.

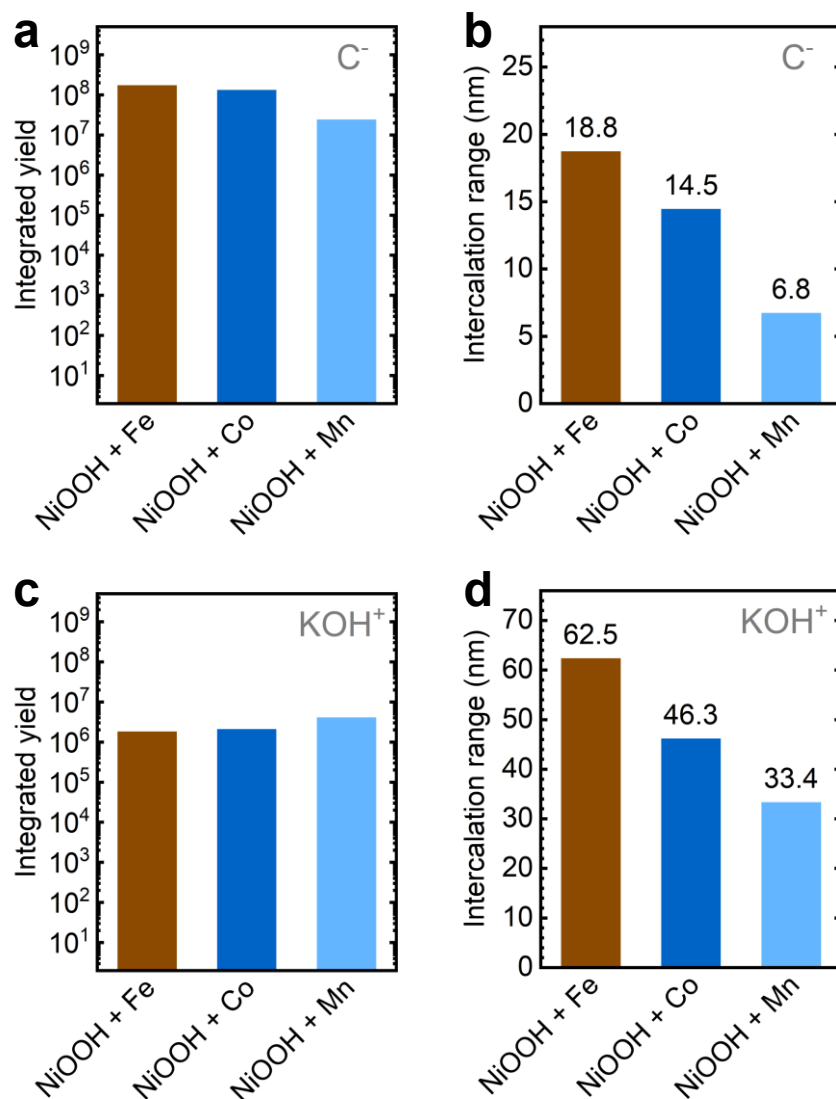


**Figure S26.** TOF-SIMS depth profile data analysis: (a, c) integrated yields and (b, d) intercalation ranges for (a, b) C<sup>-</sup> and (c, d) KOH<sup>+</sup> ion fragments in NF-NiOOH electrodes after CP conditioning in purified 1 M KOH electrolyte spiked with 100 ppb of Fe<sup>3+</sup>, Co<sup>2+</sup>, and Mn<sup>2+</sup>.

**Supporting Note:** In **Figure S26**, the integrated yield accounts for approximately 68% and 87% of the total C<sup>-</sup> and KOH<sup>+</sup> concentrations, respectively. The range for intercalation is identified by pinpointing the sputtering times where the dashed lines in **Figures S24** and **S25** intersect with the depth profile. These times are then converted to depth units (in nm) using the previously determined sputtering rate of  $0.056 \pm 0.01 \text{ nm} \cdot \text{s}^{-1}$  from NCP measurements (**Figure S21**). The intercalation range is calculated as the difference between these converted depth units. These values and the intercalation range are presented in **Figures 6e** and **f** of the main manuscript.

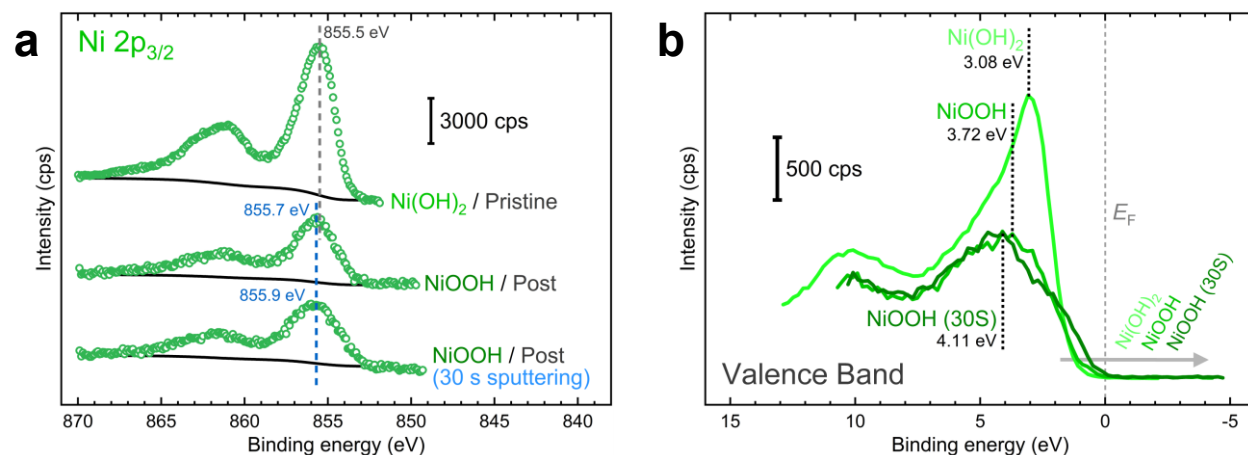


**Figure S27.** XPS spectra of the as-deposited NF-Ni(OH)<sub>2</sub> electrode, NF-NiOOH electrode, and NF-NiOOH electrode after 30 s of Ar<sup>+</sup> sputtering: (a) Ni 2p<sub>3/2</sub> and (b) valence band (VB) regions. Spectra in (a) are offset on the y-axis for clarity. The original XPS spectra are shown as open circles. The dashed line at 0 eV in (b) represents the Fermi level ( $E_F$ ) and is shown as a reference.

**Supporting Note.** We conducted a series of control XPS measurements to optimize the analysis of NF-NiOOH electrodes after CP conditioning in purified 1 M KOH electrolyte. **Figure S27a** reveals that electrochemically conditioned samples display a subdued peak shifting toward higher binding energies. This could be indicative of a higher proportion of the NiOOH phase.<sup>27,29</sup> This trend persists even when the surface is sputtered with Ar<sup>+</sup>, exposing the inner layers of NiOOH. Furthermore, a detailed examination of the valence band shows that the valence band maximum (VBM) shifts closer to 0 eV for the NiOOH sample (see **Figure S27b**). This shift intensifies after sputtering, exposing a more significant amount of higher-conductivity NiOOH. However, it is clear that not all Ni(OH)<sub>2</sub> transforms into NiOOH; some NiOOH may revert to Ni(OH)<sub>2</sub> upon contact with water. Therefore, as recommended by prior research,<sup>27,28</sup> we opted to deconvolve the XPS signals using a blend of Ni(OH)<sub>2</sub> and NiOOH phases.

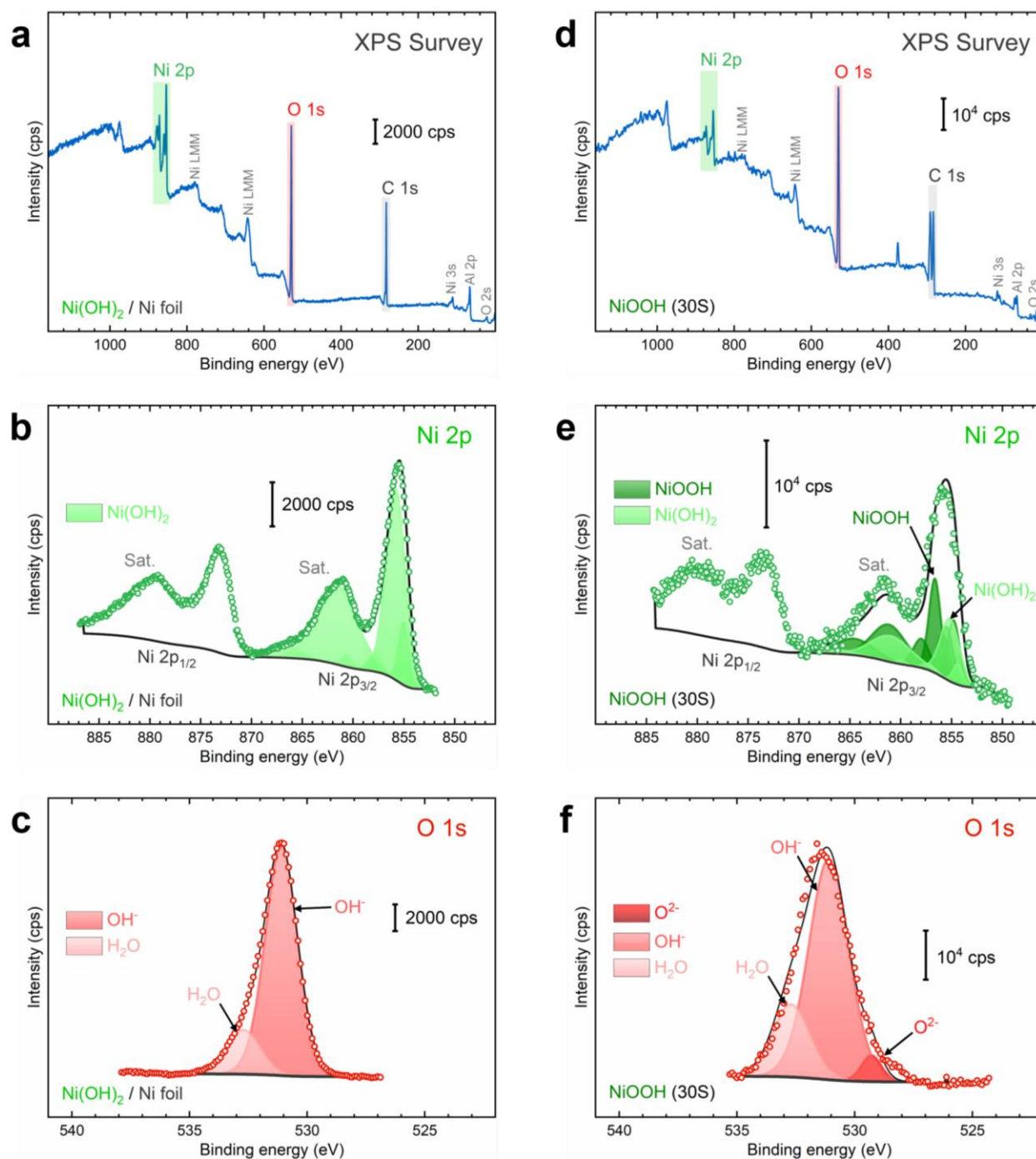


**Figure S28.** XPS spectra of the as-deposited NF-Ni(OH)<sub>2</sub> electrode: (a) XPS survey, (b) Ni 2p region, and (c) O 1s region. XPS spectra of the NF-NiOOH electrode after CP conditioning in purified 1 M KOH electrolyte and Ar<sup>+</sup> sputter etching for 30 s: (d) XPS survey, (e) Ni 2p region, and (f) O 1s region. The original XPS spectra are shown as open circles, and the envelopes of the component fit are drawn as solid lines.

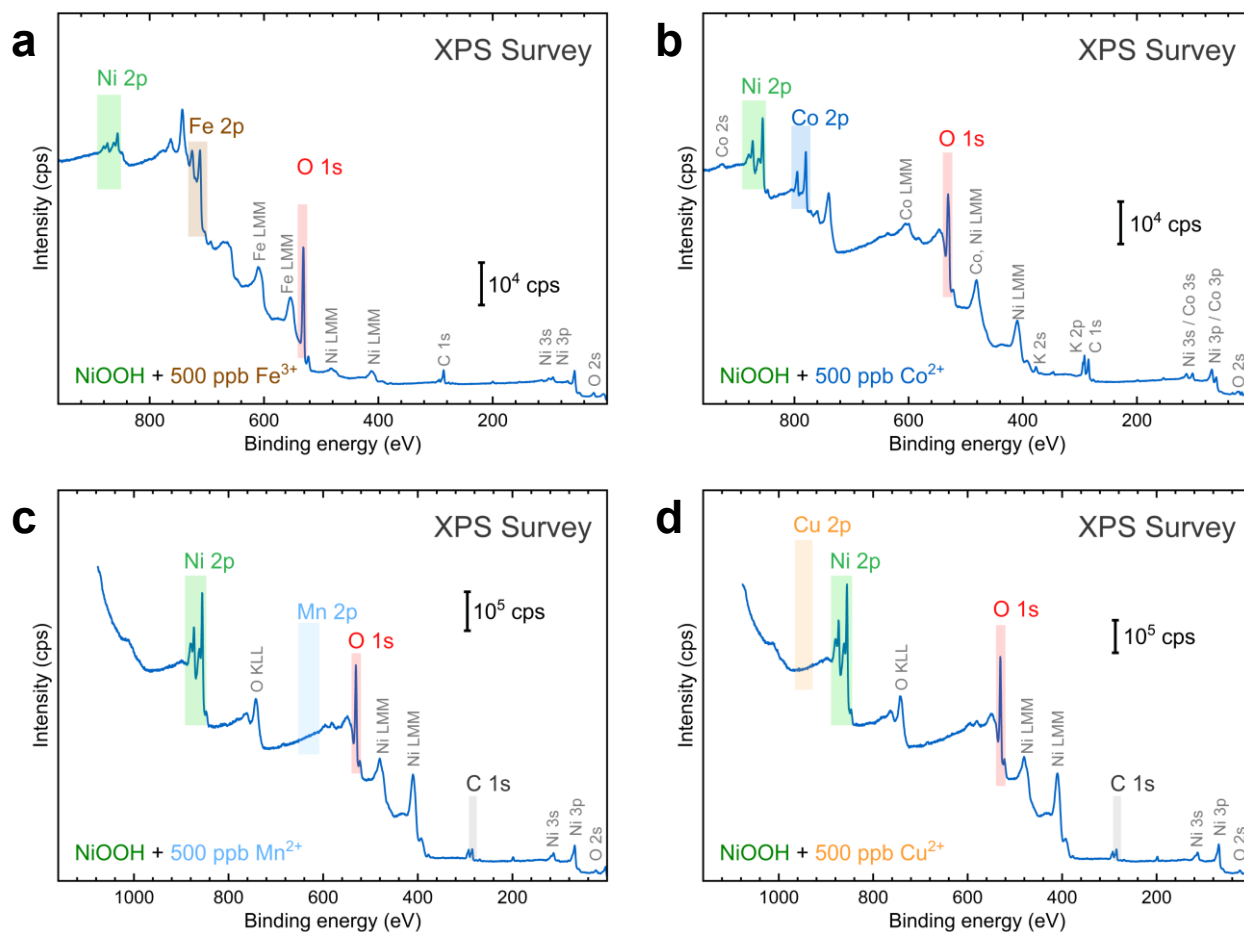


**Figure S29.** XPS survey scans of NF-NiOOH electrodes after CP conditioning in purified 1 M KOH electrolyte spiked with transition metal cations (500 ppb  $M^{n+}$ ): (a)  $Fe^{3+}$ , (b)  $Co^{2+}$ , (c)  $Mn^{2+}$ , and (d)  $Cu^{2+}$ . Key peaks and areas of interest are highlighted for clarity.

**Supporting Note:** To enhance the weak signals associated with Fe, Co, Mn, and Cu, we increased the transition metal concentration to 500 ppb. This signal weakness was likely caused by residual potassium from the KOH electrolyte, as demonstrated by the presence of K 2p peaks near the C 1s signal in **Figure S29**. Increasing the concentration confirmed the incorporation of Fe and Co into the NiOOH electrocatalytic films. However, Mn and Cu signals were still absent, suggesting they may be below the XPS detection threshold if present.

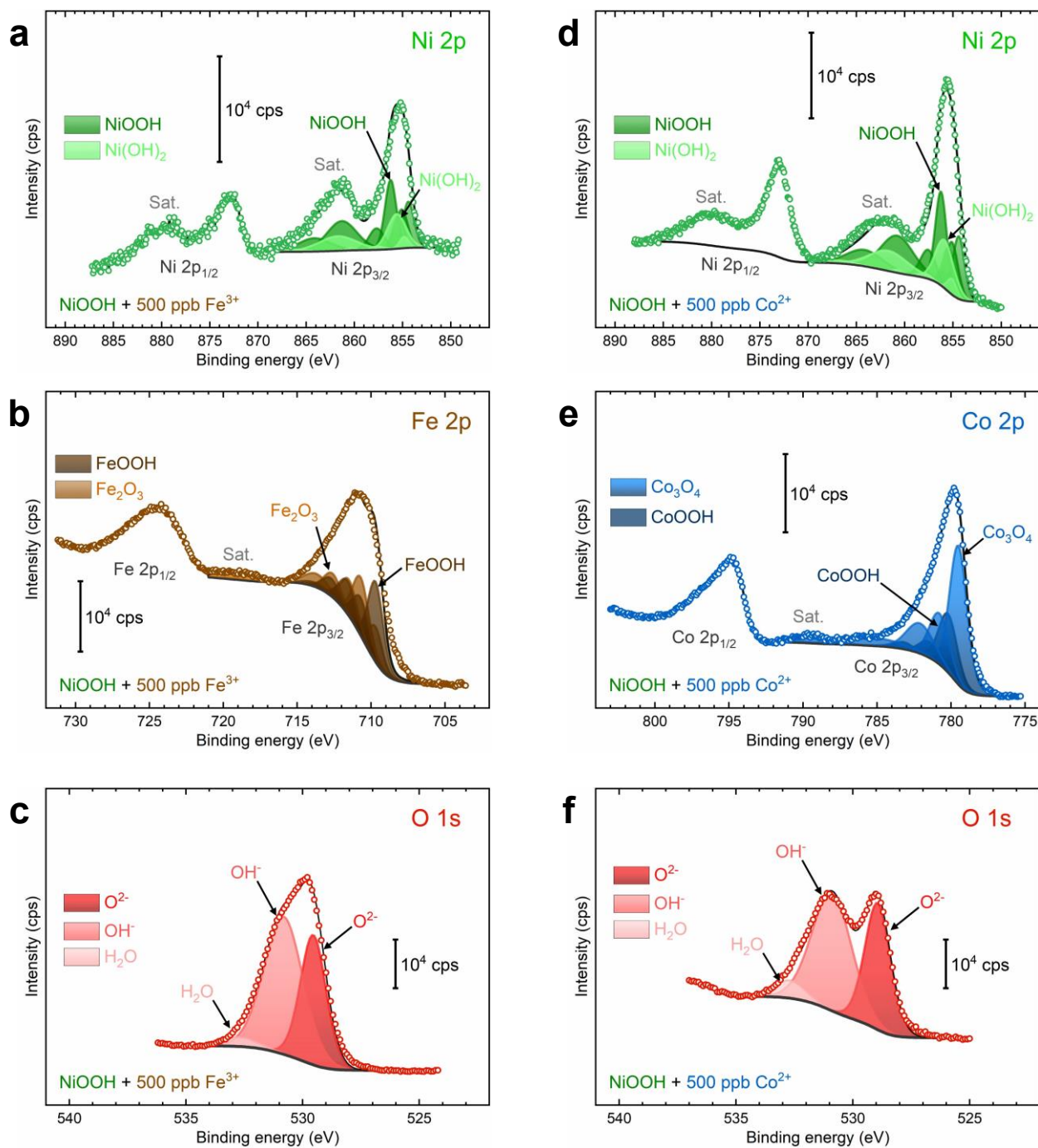


**Figure S30.** XPS spectra of NF-NiOOH electrodes after CP conditioning: Panels (a), (b), and (c) display the Ni 2p, Fe 2p, and O 1s regions, respectively, for films conditioned in purified 1 M KOH electrolyte spiked with 500 ppb of  $\text{Fe}^{3+}$ . Panels (d), (e), and (f) show the Ni 2p, Co 2p, and O 1s regions for films conditioned in purified 1 M KOH electrolyte spiked with 500 ppb of  $\text{Co}^{2+}$ . The original XPS spectra are shown as open circles, and the envelopes of the component fit are drawn as solid lines.

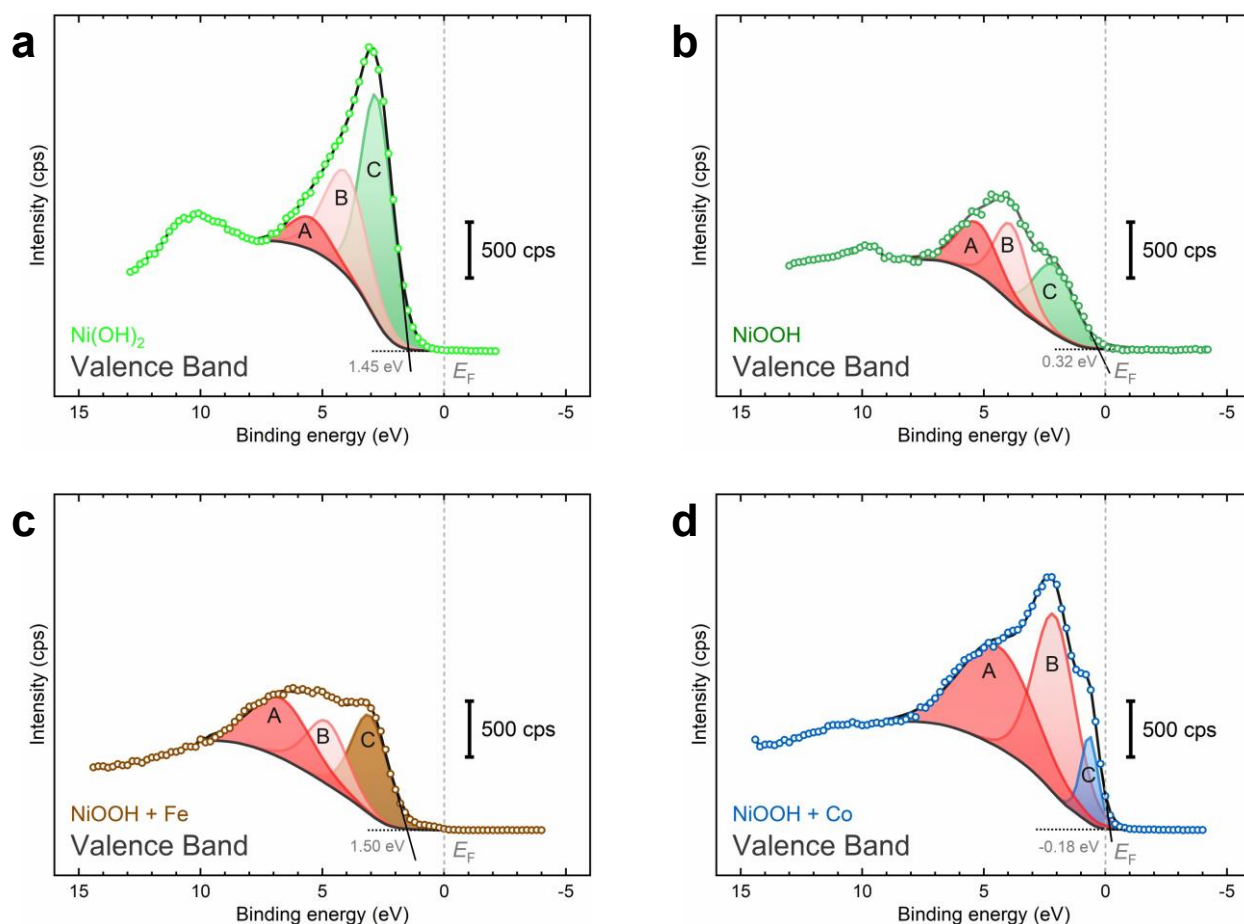


**Figure S31.** Fitting of the VB spectra of (a) as-deposited NF-Ni(OH)<sub>2</sub> electrode, (b) NF-NiOOH electrode after CP conditioning in purified KOH electrolyte, and NF-NiOOH electrodes after conditioning in purified 1 M KOH electrolyte spiked with 500 ppb of (c) Fe<sup>3+</sup>, and (d) Co<sup>2+</sup>. The original valence band XPS spectra are shown as open circles, and the envelopes of the component fit are drawn as solid lines. The dashed line at 0 eV represents the Fermi level ( $E_F$ ) and is shown as a reference.

**Supporting Note:** The electronic states of Ni(OH)<sub>2</sub>/NiOOH near the Fermi level can be separated into three primary components: bonding O 2p states (represented by peak A), nonbonding O 2p states (peak B), and antibonding transition metal 3d states (peak C). For the fitting, we selected a Gauss-Lorentz peak shape with a 40:60 ratio, in line with findings from previous studies.<sup>35–37</sup> The VBM (in eV) was determined when zero intensity intersects with a linear regression fit of the low binding-energy edge of the valence band spectra.

**Table S3.** Fitting parameters from the valence band spectra shown in **Figure S31**.

Sample	Peak position (eV)			B-C peak distance (eV)	Peak FWHM (eV)			Peak area		
	A	B	C		A	B	C	A	B	C
Ni(OH) <sub>2</sub> (Pristine )	5.50	4.03	2.78	1.26	1.97	2.07	1.52	650.9	2090.3	3355.5
NiOOH (after OER)	5.35	3.97	2.20	1.77	1.99	1.60	2.00	1083.5	1282.5	1409.5
NiOOH + 500 ppb Co <sup>2+</sup>	4.47	2.09	0.64	1.45	3.56	2.07	0.80	3442.7	3672.0	657.5
NiOOH + 500 ppb Fe <sup>3+</sup>	6.66	4.70	3.00	1.70	2.99	2.15	1.71	1739.9	1342.6	1568.4

**Supporting Note:** According to Heymann and coworkers,<sup>35</sup> the peak position and width indicate the extent of O 2p and metal 3d orbital overlap, thereby providing a rough estimate for M–O bond covalency. In the case of NiOOH with incorporated Co, the reduced distance between the maxima of peaks B and C, along with the broadening of O 2p states (peaks A and B), indicates a higher Co–O bond covalency compared to that of the Fe–O bond.

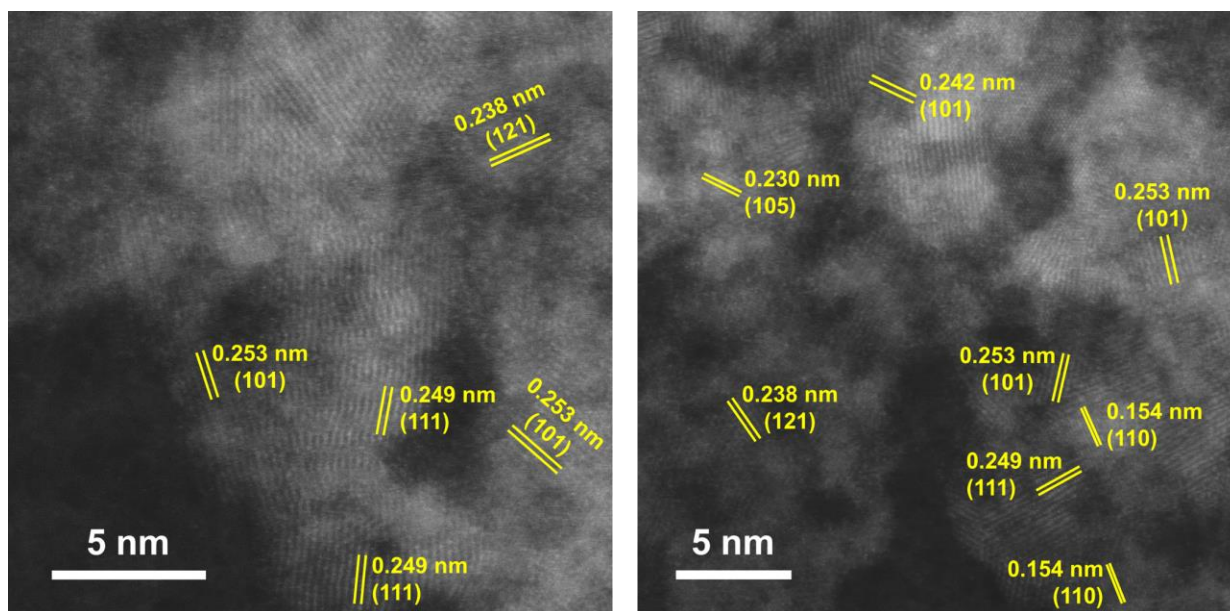


**Figure S32.** HAADF STEM images of NiOOH particles extracted from NF-NiOOH electrodes after CP conditioning in purified 1 M KOH electrolyte.

**Supporting Note:** The HAADF STEM images of **Figure S32** depict lattice planes corresponding to three crystalline phases: the (102) and (101) planes of  $\gamma$ -NiOOH (PDF#00-006-0075), (101), (111), and (121) planes of  $\text{Ni}_2\text{O}_3\text{H}$  (PDF#00-040-1179), and (110), (103), and (104) planes of  $\text{Ni}_x\text{OH}_y$  (PDF#00-027-0340). However, we note that some lattice planes fall within the uncertainty threshold, making it challenging to distinguish between different crystalline phases. Given that particles for HAADF STEM analysis were obtained from the film through sonication, the images are not representative of the surface composition. This accounts for the observed presence of  $\text{Ni}(\text{OH})_2$ . These results reflect a composite of  $\text{Ni}(\text{OH})_2$  and NiOOH phases following electrochemical conditioning.

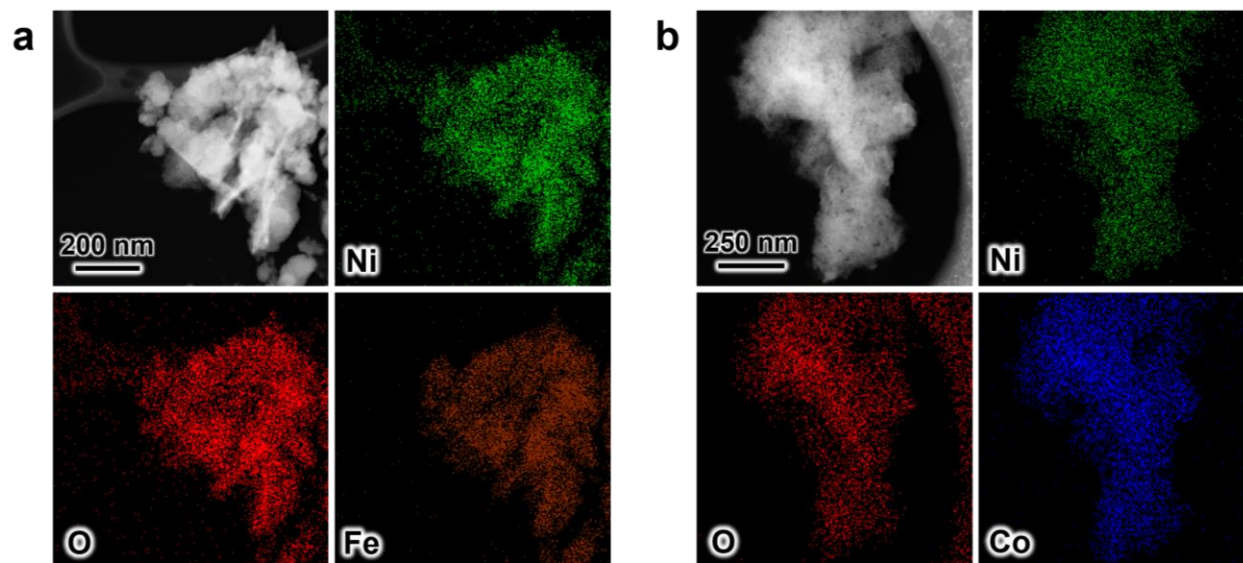


**Figure S33.** STEM images and EDX elemental mappings of Ni, Fe, Co, and O of NiOOH particles extracted from NF-NiOOH electrodes after CP conditioning in purified 1 M KOH electrolyte spiked with 500 ppb of (a)  $\text{Fe}^{3+}$  and (b)  $\text{Co}^{2+}$ .

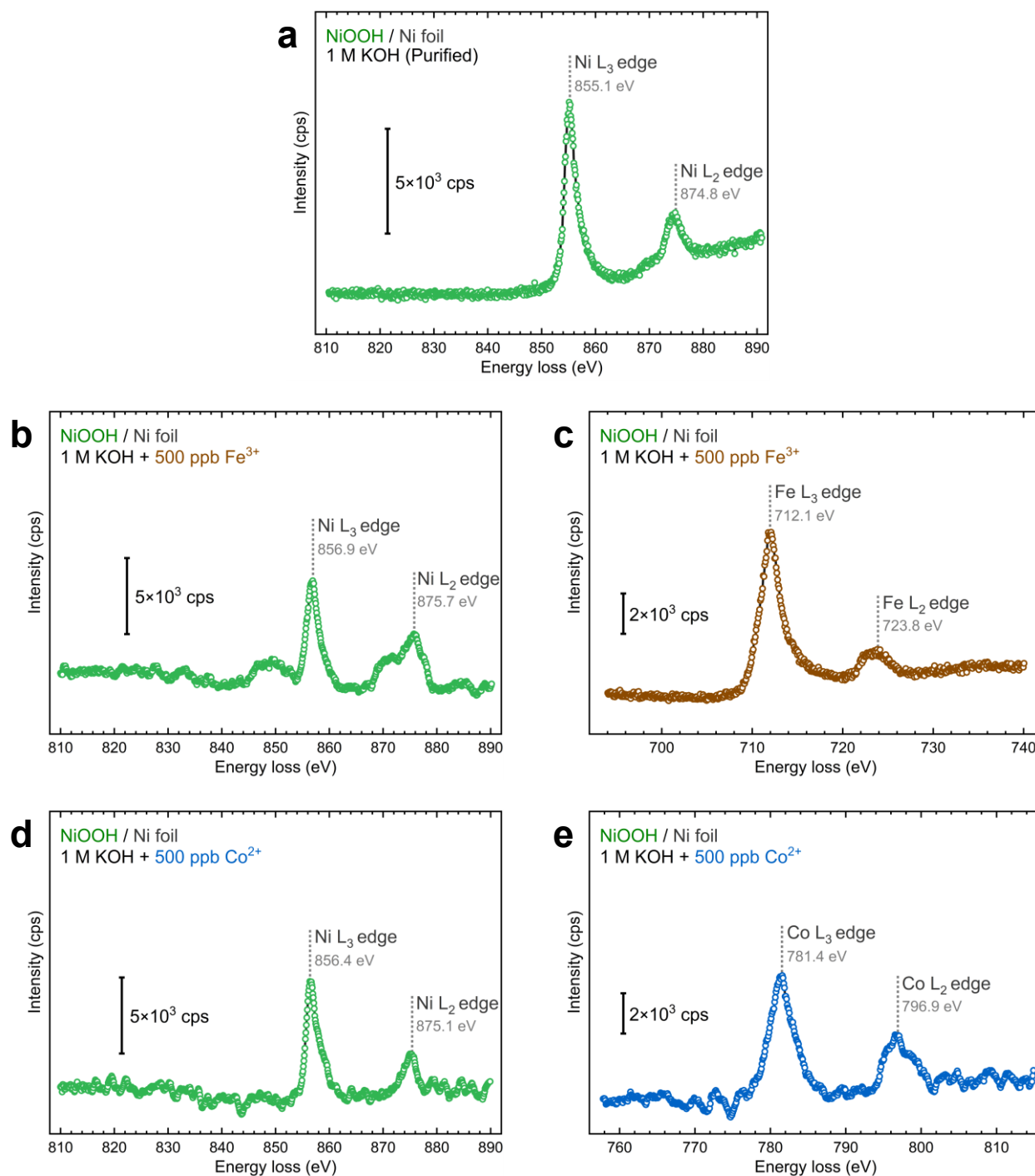


**Figure S34.** EELS analysis of NiOOH particles extracted from NF-NiOOH electrodes after CP conditioning: (a) Ni L<sub>2,3</sub>-edge spectrum from a sample conditioned in purified 1 M KOH electrolyte, (b) Ni L<sub>2,3</sub>-edge and (c) Fe L<sub>2,3</sub>-edge spectra from a sample conditioned in purified 1 M KOH electrolyte spiked with 500 ppb of Fe<sup>3+</sup>, and (d) Ni L<sub>2,3</sub>-edge and (e) Co L<sub>2,3</sub>-edge spectra from a sample conditioned in purified 1 M KOH electrolyte spiked with 500 ppb of Co<sup>2+</sup>. Peak positions, expressed in eV, are indicated in gray at the maxima.

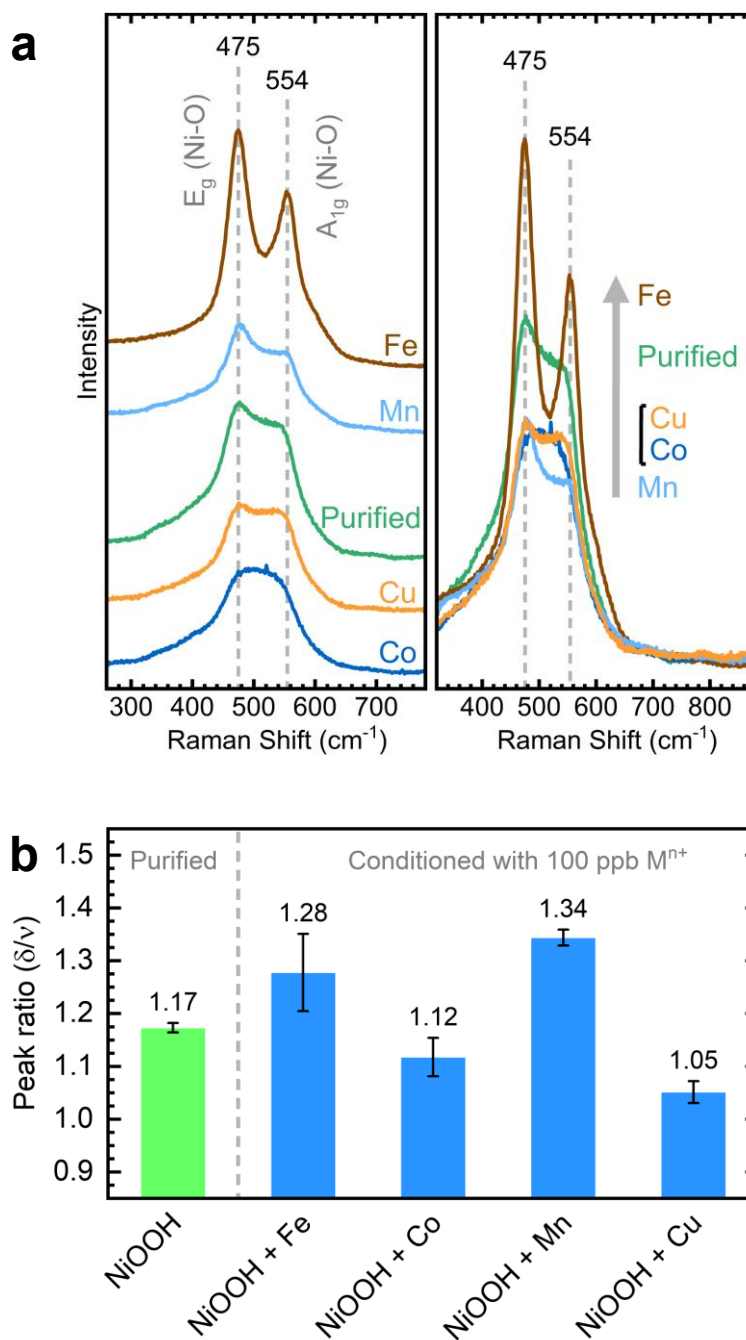


**Figure S35.** (a) Raman spectra of NF-NiOOH electrodes after conditioning in purified 1 M KOH electrolyte spiked with transition metal cations (100 ppb  $\text{M}^{\text{n}+}$ ). The electrodes were aged for one week in the KOH electrolyte containing transition metals and then conditioned electrochemically *via* CP at  $2.5 \text{ mA}\cdot\text{cm}^{-2}$  for 5 min. Left panel: Individual spectra offset on the y-axis for clarity. Right panel: Overlay of all spectra for comparison. (b) Bar plot showing the corresponding ratios of the peaks for the  $\delta(\text{O-Ni-O})$  bending ( $E_g$ ) and  $\nu(\text{O-Ni-O})$  stretching ( $A_{1g}$ ) vibrational modes, depicted in (a), across different transition metals spiked to the electrolyte. Uncertainty bars indicate the standard deviation derived from five replicate measurements. Laser: 633 nm.

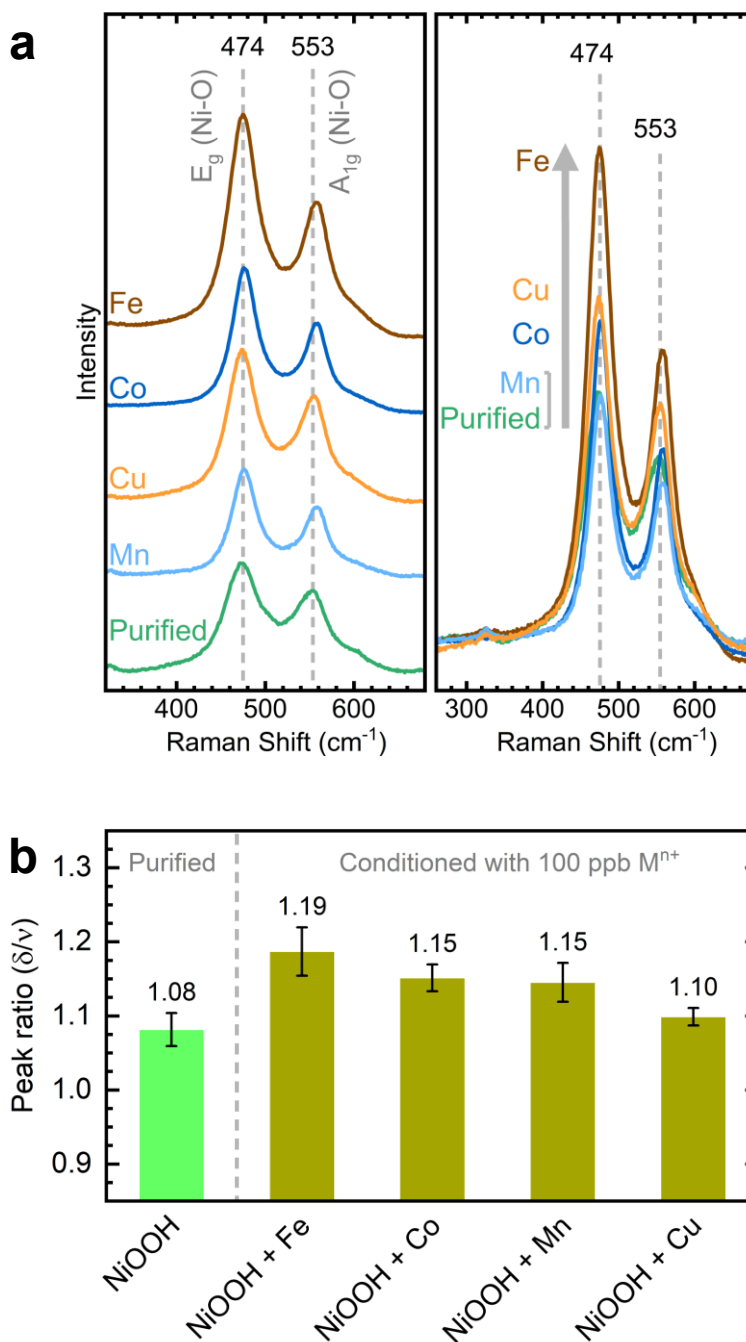


**Figure S36.** (a) Raman spectra of Au-*t*-NiOOH electrodes after conditioning in purified 1 M KOH electrolyte spiked with transition metal cations (100 ppb  $M^{n+}$ ). The electrodes were aged for one week in the KOH electrolyte containing transition metals and then conditioned electrochemically *via* CP at  $1 \text{ mA}\cdot\text{cm}^{-2}$  for 5 min. Left panel: Individual spectra offset on the y-axis for clarity. Right panel: Overlay of all spectra for comparison. (b) Bar plot showing the corresponding ratios of the peaks for the  $\delta(\text{O-Ni-O})$  bending ( $E_g$ ) and  $\nu(\text{O-Ni-O})$  stretching ( $A_{1g}$ ) vibrational modes, depicted in (a), across different transition metals spiked to the electrolyte. Uncertainty bars indicate the standard deviation derived from five replicate measurements. Laser: 633 nm.

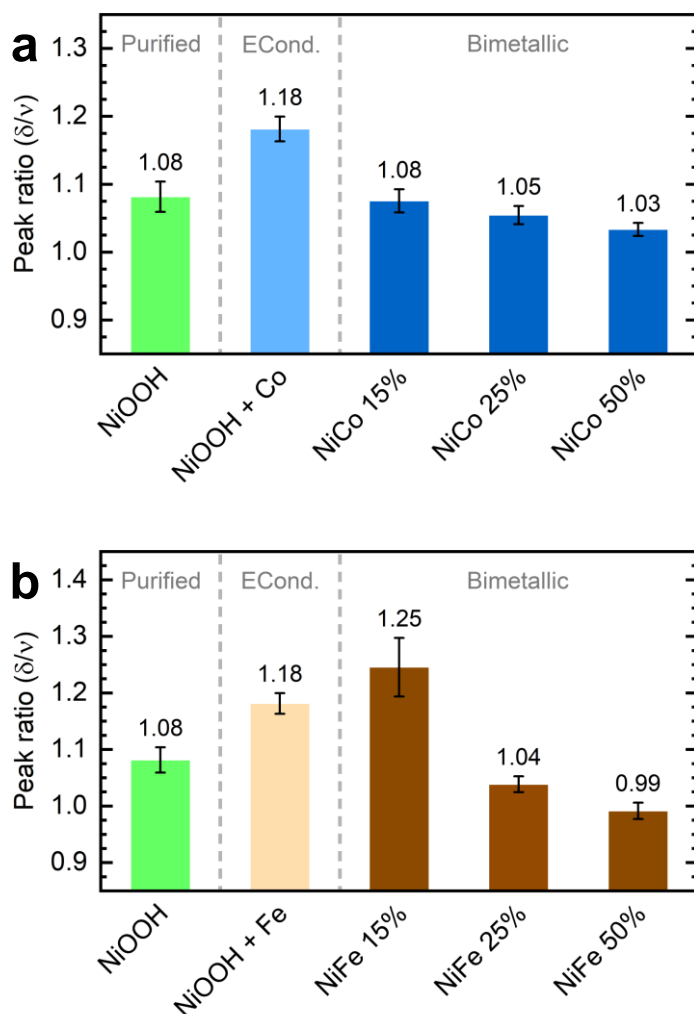


**Figure S37.** Bar plots illustrating the varying ratios of the  $\delta(\text{O-Ni-O})$  and  $\nu(\text{O-Ni-O})$  bands with increasing incorporation levels of (a) Co and (b) Fe, as shown in **Figures 8d** and **e**. The Au-*t*-NiOOH electrodes were aged for one week in purified 1 M KOH electrolyte containing  $\text{Fe}^{3+}$  or  $\text{Co}^{2+}$  (100 ppb  $\text{M}^{\text{n}+}$ ) and then conditioned electrochemically *via* CP at  $1 \text{ mA}\cdot\text{cm}^{-2}$  for 5 min. Uncertainty bars indicate the standard deviation derived from five replicate measurements. Metal content percentages are presented in terms of average atomic percent (at.%) from EDX measurements.

**Supporting Note:** We recognize the challenge of comparing results obtained from Au-*t*-NiOOH electrodes used for SERS measurements with those from thicker NF-NiOOH electrodes. We employed thin films to amplify the Raman scattering and perform a more adequate analysis of the  $\text{NiO}_2$  lattice modes. It is essential to clarify that SERS measurements were conducted only to offer supporting evidence regarding the presence of segregated phases on the surface. These measurements do not constitute a critical aspect of our study. Further investigation is necessary to draw definitive conclusions in this regard.

**Table S4.** Crystal field stabilization energies, octahedral site preference energy, ionic radii, and Jahn-Teller distortion for  $d^n$  configurations of Ni, Co, Fe, Mn, and Cu cations.

Metal	Charge	$d$ electrons	Spin state	Configuration	CFSE <sub>(oct)</sub> *	OSSE**	Ionic radius <sup>†</sup> (Å)	Jahn-Teller distortion
Ni	+2	8	-	$t_{2g}^6 e_g^2$	$-1.2\Delta_o$	$-0.844\Delta_o$	0.69	No
	+3	7	Low spin	$t_{2g}^6 e_g^1$	$-1.8\Delta_o + P$	$-1.266\Delta_o + P$	0.56	Strong
			High spin	$t_{2g}^5 e_g^2$	$-0.8\Delta_o$	$-0.266\Delta_o$	0.60	Weak
	+4	6	Low spin	$t_{2g}^6 e_g^0$	$-2.4\Delta_o + 2P$	$-2.133\Delta_o + 2P$	0.48	No
Co	+2	7	Low spin	$t_{2g}^6 e_g^1$	$-1.8\Delta_o + P$	$-1.266\Delta_o + P$	0.65	Strong
			High spin	$t_{2g}^5 e_g^2$	$-0.8\Delta_o$	$-0.266\Delta_o$	0.75	Weak
	+3	6	Low spin	$t_{2g}^6 e_g^0$	$-2.4\Delta_o + 2P$	$-2.133\Delta_o + 2P$	0.55	No
			High spin	$t_{2g}^4 e_g^2$	$-0.4\Delta_o$	$-0.133\Delta_o$	0.61	Weak
Fe	+2	6	Low spin	$t_{2g}^6 e_g^0$	$-2.4\Delta_o + 2P$	$-2.133\Delta_o + 2P$	0.61	No
			High spin	$t_{2g}^4 e_g^2$	$-0.4\Delta_o$	$-0.133\Delta_o$	0.78	Weak
	+3	5	Low spin	$t_{2g}^5 e_g^0$	$-2\Delta_o + 2P$	$-2\Delta_o + 2P$	0.55	Weak
			High spin	$t_{2g}^3 e_g^2$	0	0	0.65	No
Mn	+2	5	Low spin	$t_{2g}^5 e_g^0$	$-2\Delta_o + 2P$	$-2\Delta_o + 2P$	0.67	Weak
			High spin	$t_{2g}^3 e_g^2$	0	0	0.83	No
	+3	4	Low spin	$t_{2g}^4 e_g^0$	$-1.6\Delta_o + P$	$-1.422\Delta_o + P$	0.58	Weak
			High spin	$t_{2g}^3 e_g^1$	$-0.6\Delta_o$	$-0.422\Delta_o$	0.65	Strong
+4	3	-	$t_{2g}^3 e_g^0$	$-1.2\Delta_o$	$-0.844\Delta_o$	0.53	No	
Cu	+2	9	-	$t_{2g}^6 e_g^3$	$-0.6\Delta_o$	$-0.422\Delta_o$	0.73	Strong

The database of crystal and ionic radii was taken from ref<sup>38</sup>.

\*CFSE: Crystal field stabilization energy; \*\* OSSE: Octahedral site stabilization energy;

<sup>†</sup>Ionic radius for VI coordination (octahedral).

**Supporting Note:** The CFSE for an octahedral ligand field was calculated as follows:<sup>39</sup>

$$CFSE_{(oct)} = E_{ligand} - E_{isotropic} = \left[ -\frac{2}{5}\Delta_o(e_{t_{2g}}^-) + \frac{3}{5}\Delta_o(e_{e_g}^-) + nP \right] - nP$$

where  $E_{ligand}$  is the energy of the octahedral ligand field,  $E_{isotropic}$  is the energy of the isotropic field,  $\Delta_o$  is the octahedral-site splitting,  $P$  is the spin pairing energy,  $n$  is the number of electron pairs, and  $e_{t_{2g}}^-$  and  $e_{e_g}^-$  are the number of electrons occupying the  $t_{2g}$  and  $e_g$  bands, respectively. The OSSE was calculated as follows:<sup>40</sup>

$$OSSE = CFSE_{(oct)} - CFSE_{(tet)}$$

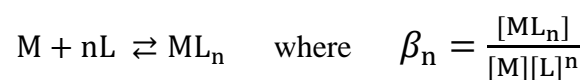
where  $CFSE_{(tet)} = \frac{2}{5}\Delta_t(e_{t_2}^-) - \frac{3}{5}\Delta_t(e_e^-) + nP$  and  $9\Delta_t \approx 4\Delta_o$ .

**Table S5.** Cumulative formation constants for metal-hydroxide (M-OH) complexes.

Cation	log $\beta_1$	log $\beta_2$	log $\beta_3$	log $\beta_4$	Temperature (°C)	Ionic strength (mol·L <sup>-1</sup> )
Mn <sup>2+</sup>	3.4	-	-	7.7	25	0.0
Fe <sup>2+</sup>	4.6	7.5	13	10	25	0.0
Fe <sup>3+</sup>	11.8	23.4	-	34.4	25	0.0
Co <sup>2+</sup>	4.3	9.2	10.5	9.7	25	0.0
Co <sup>3+</sup>	13.5	-	-	-	25	3.0
Ni <sup>2+</sup>	4.1	9.0	12.0	-	25	0.0
Cu <sup>2+</sup>	6.5	11.8	14.5	15.6	25	0.0

The database of complex formation constants was taken from ref <sup>41</sup>.

**Supporting Note:** The cumulative or overall formation constant,  $\beta_n$ , represents the stability constant for the formation of a complex from reagents as follows:



Note that  $\beta_n$  is related to the stepwise formation constants ( $K_i$ ) as follows:

$$\beta_n = K_1 K_2 \dots K_n$$

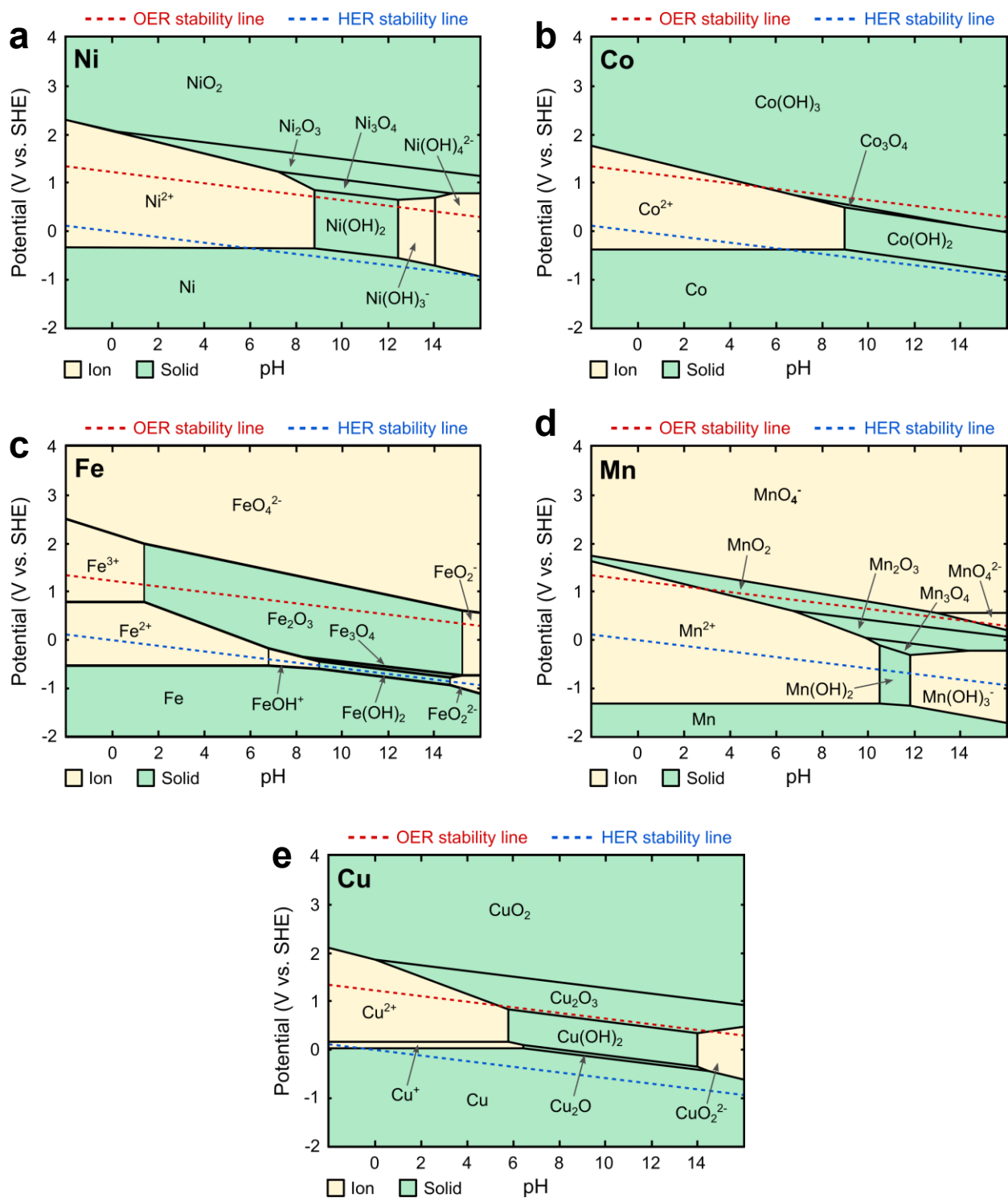


**Figure S38.** Pourbaix diagrams of (a) Ni, (b) Co, (c) Fe, (d) Mn, and (e) Cu using an ion concentration of  $10^{-5} \text{ mol}\cdot\text{L}^{-1}$ . The plots were adapted from diagrams generated using the Materials Project.<sup>42-45</sup>

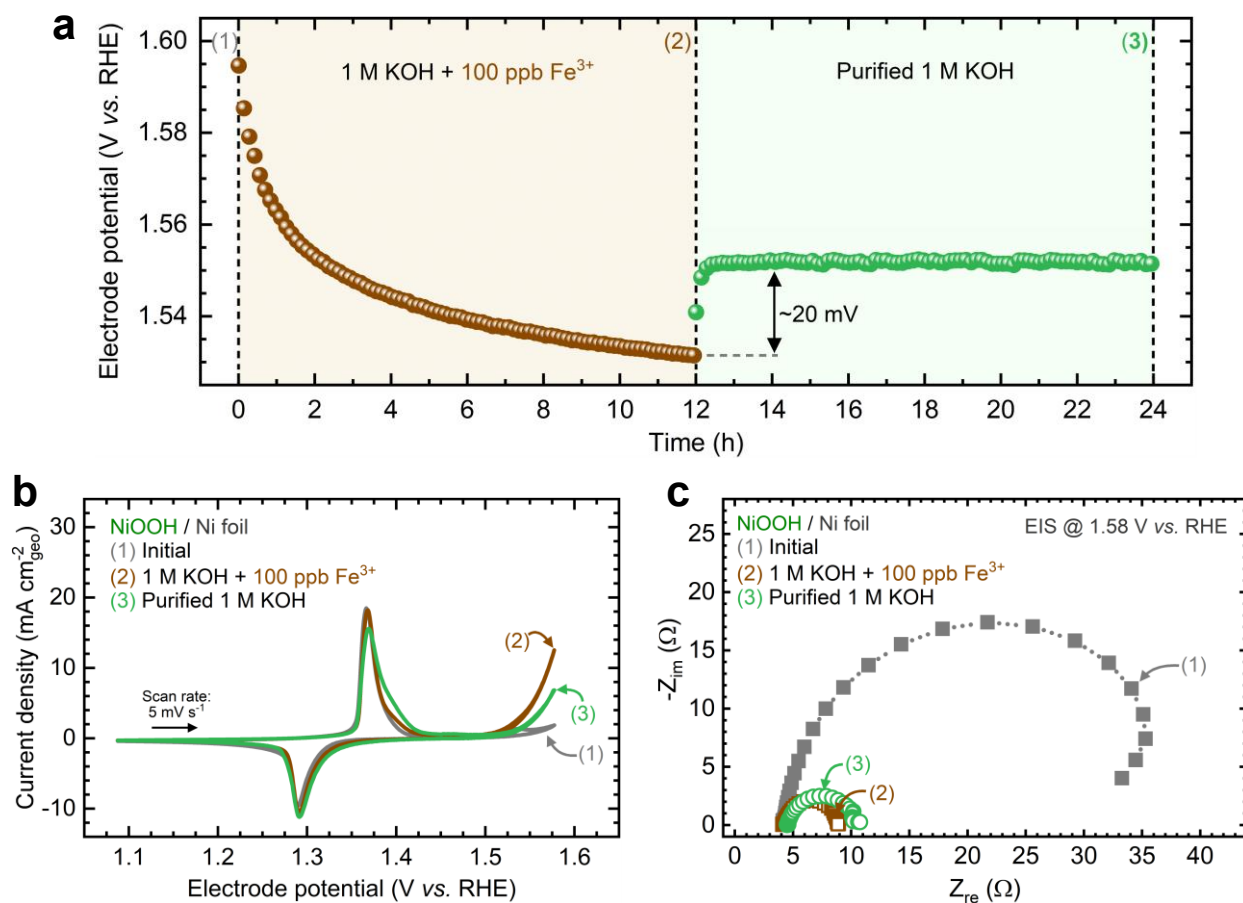


**Figure S39.** Reversing Fe incorporation on NF-NiOOH electrodes by substituting the electrolyte: (a) CP conditioning curve measured at 2.5 mA·cm<sup>-2</sup> in 1 M KOH electrolyte containing 100 ppb of Fe<sup>3+</sup>, then substituted with purified 1 M KOH; (b) CV scans and (c) Nyquist plots aligned with the specific stages noted in panel (a). The numbers in panel (a) indicate the following stages: (1) the sample prior to CP conditioning, (2) the sample after CP conditioning in the Fe<sup>3+</sup>-containing 1 M KOH, and (3) the sample after the second CP conditioning step in purified 1 M KOH.

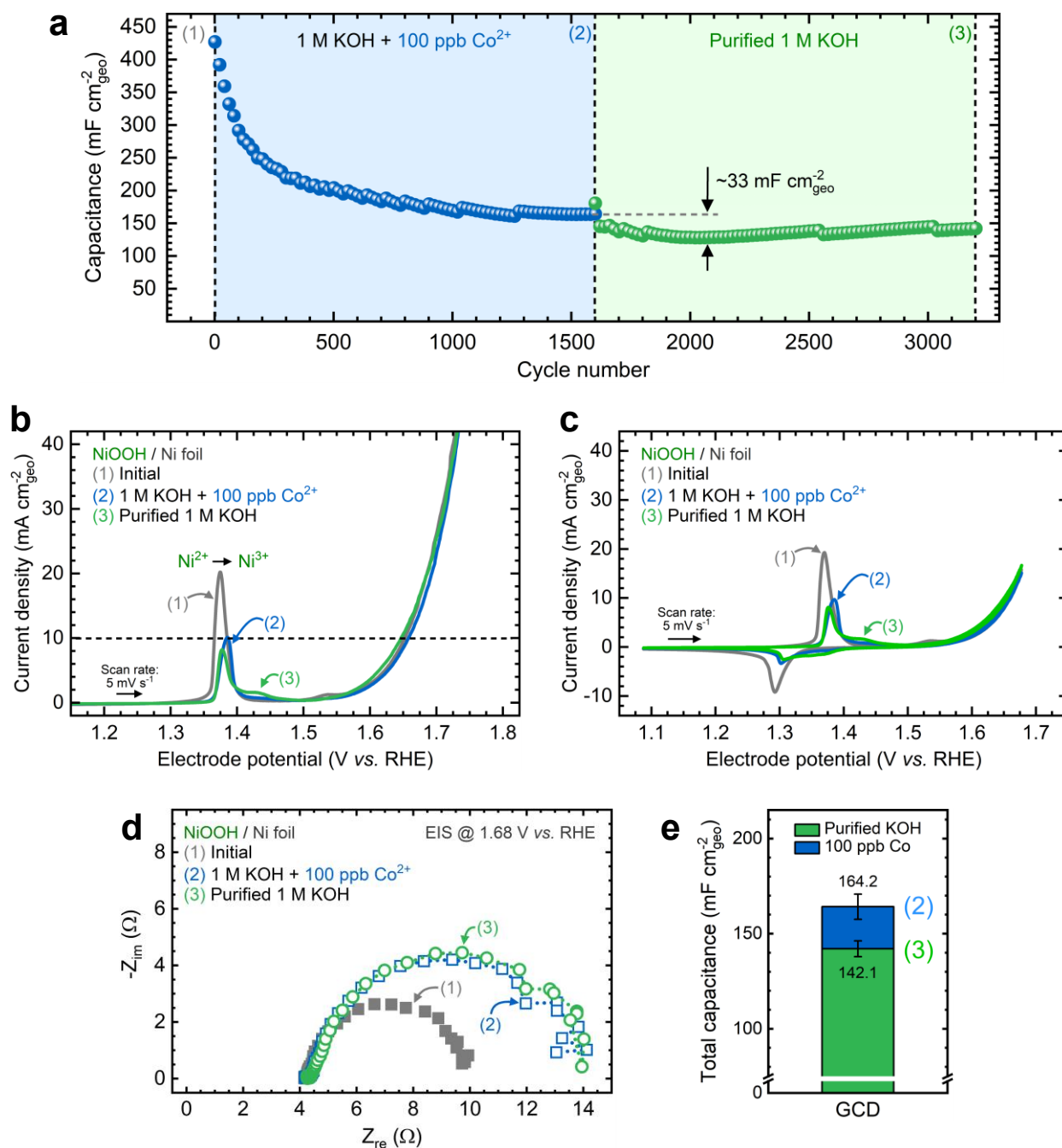


**Figure S40.** Reversing Co incorporation on NF-NiOOH electrodes by substituting the electrolyte: (a) total capacitance derived from GCD conditioning at  $2.5 \text{ mA} \cdot \text{cm}^{-2}$  in 1 M KOH containing 100 ppb of  $\text{Co}^{2+}$ , then substituted with purified 1 M KOH; (b) LSV scans, (c) CV scans, and (d) Nyquist plots aligned with the specific stages noted in panel (a). The numbers in panel (a) indicate the following stages: (1) the sample prior to GCD conditioning, (2) the sample after GCD conditioning in  $\text{Co}^{2+}$ -containing 1M KOH, and (3) the sample after the second GCD conditioning step in purified 1 M KOH. (e) Total capacitances after GCD conditioning in  $\text{Co}^{2+}$ -containing and purified 1 M KOH electrolytes. Uncertainty bars indicate the standard deviation derived from three replicate measurements.

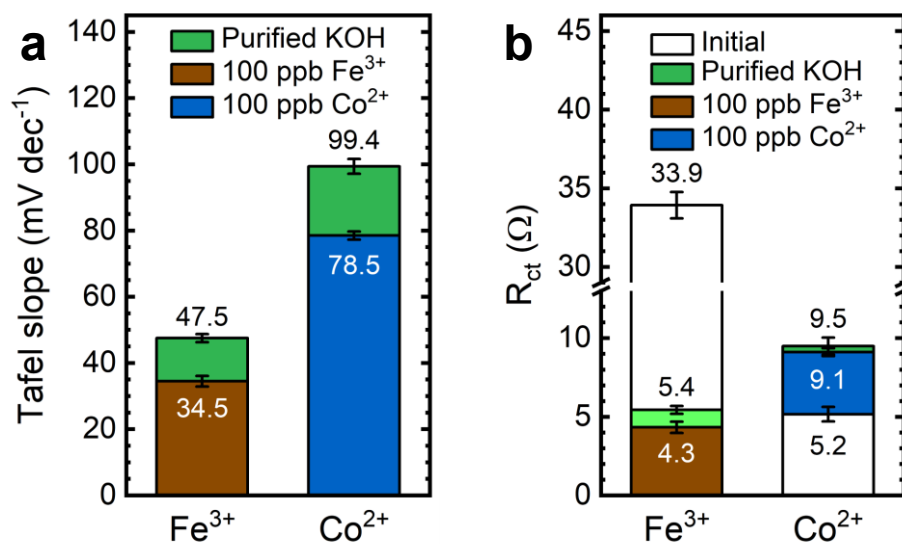


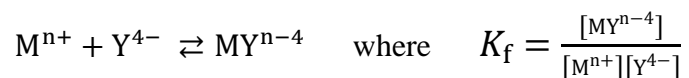
**Figure S41.** (a) Tafel slopes and (b) charge-transfer resistance values after electrochemical conditioning in metal-containing and purified 1 M KOH electrolytes. Uncertainty bars indicate the standard deviation derived from three replicate measurements. Tafel slopes are calculated as the average of values obtained from both MUSCP and MUSCA methods, while  $R_{ct}$  values are derived from EIS fitting of Nyquist plots.

**Table S6.** Formation constants for metal-EDTA (M-Y) complexes at 25 °C and 0.1 mol·L<sup>-1</sup> ionic strength. The table displays only cations present in the KOH electrolyte.

Cation	log K <sub>f</sub>						
Na <sup>+</sup>	1.86	Ba <sup>2+</sup>	7.88	Mn <sup>2+</sup>	13.89	Mn <sup>3+</sup>	25.20
K <sup>+</sup>	0.80	Zn <sup>2+</sup>	16.50	Fe <sup>2+</sup>	14.30	Fe <sup>3+</sup>	25.10
Mg <sup>2+</sup>	8.79	Zr <sup>4+</sup>	29.30	Co <sup>2+</sup>	16.45	Co <sup>3+</sup>	41.40
Ca <sup>2+</sup>	10.65	Al <sup>3+</sup>	16.40	Ni <sup>2+</sup>	18.40	Cu <sup>2+</sup>	18.78

The database of complex formation constants was taken from ref <sup>41</sup>.

**Supporting Note:** The formation constant for metal-EDTA reactions,  $K_f$ , represents the stability constant for the formation of a metal-EDTA complex as follows:



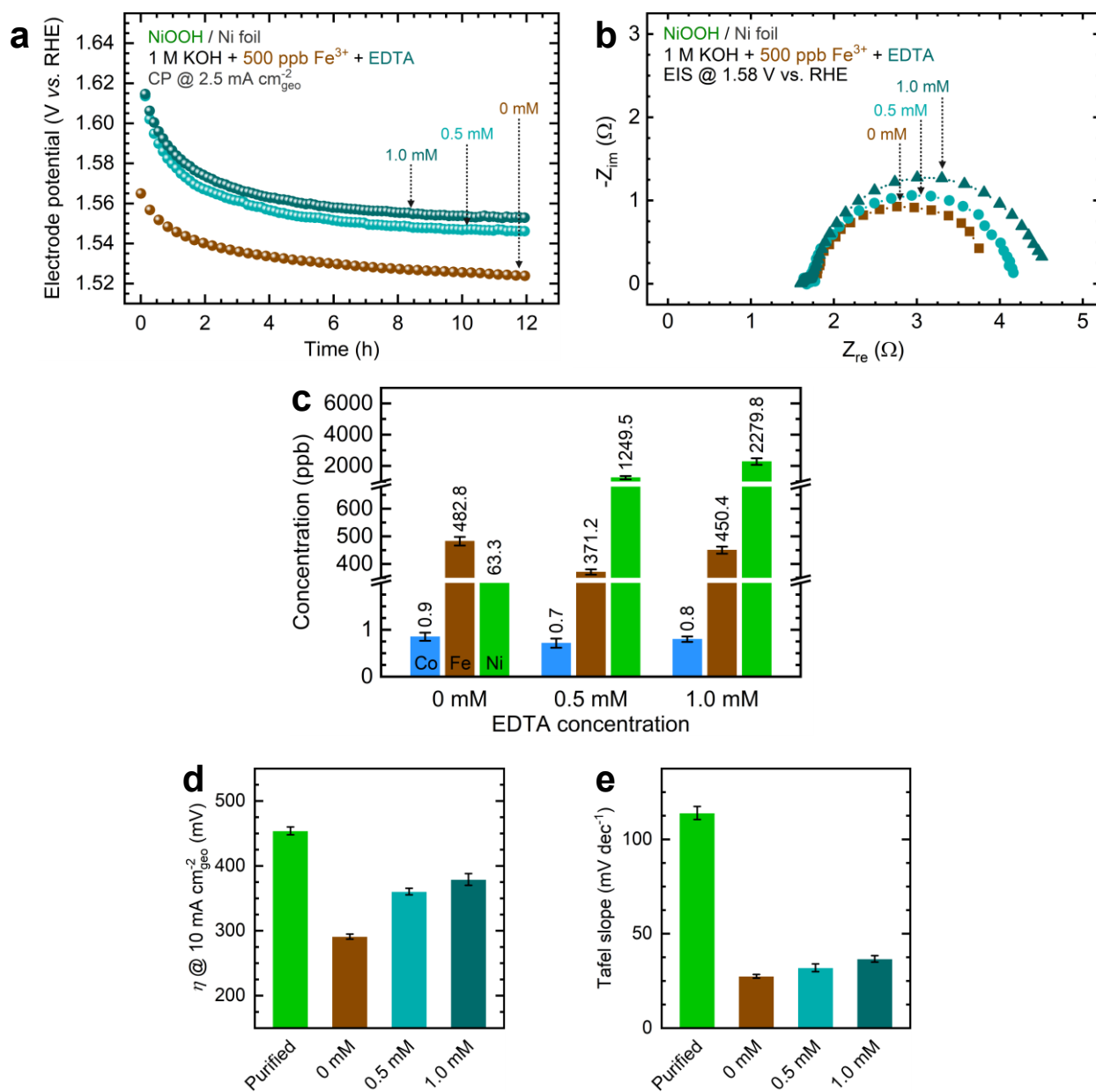


**Figure S42.** Reversing Fe incorporation on NF-NiOOH electrodes *via* metal complexation: (a) CP conditioning curves at 2.5 mA·cm<sup>-2</sup> in purified 1 M KOH electrolyte containing 500 ppb of Fe<sup>3+</sup> at increasing EDTA concentrations, (b) Nyquist plots corresponding to the EDTA concentrations specified in panel (a); (c) Ni, Co, and Fe concentrations in the 1 M KOH electrolyte, (d) OER overpotentials at 10 mA cm<sup>-2</sup> geo, and (e) Tafel slopes measured after CP conditioning at increasing EDTA concentrations. Metal concentrations in the electrolyte were determined *via* solution-mode ICP-MS using 100 μL samples collected after conditioning. OER overpotentials are determined from LSV scans. Tafel slopes are calculated as the average values obtained from MUSCP and MUSCA methods. Uncertainty bars indicate the standard deviation derived from three replicate measurements.

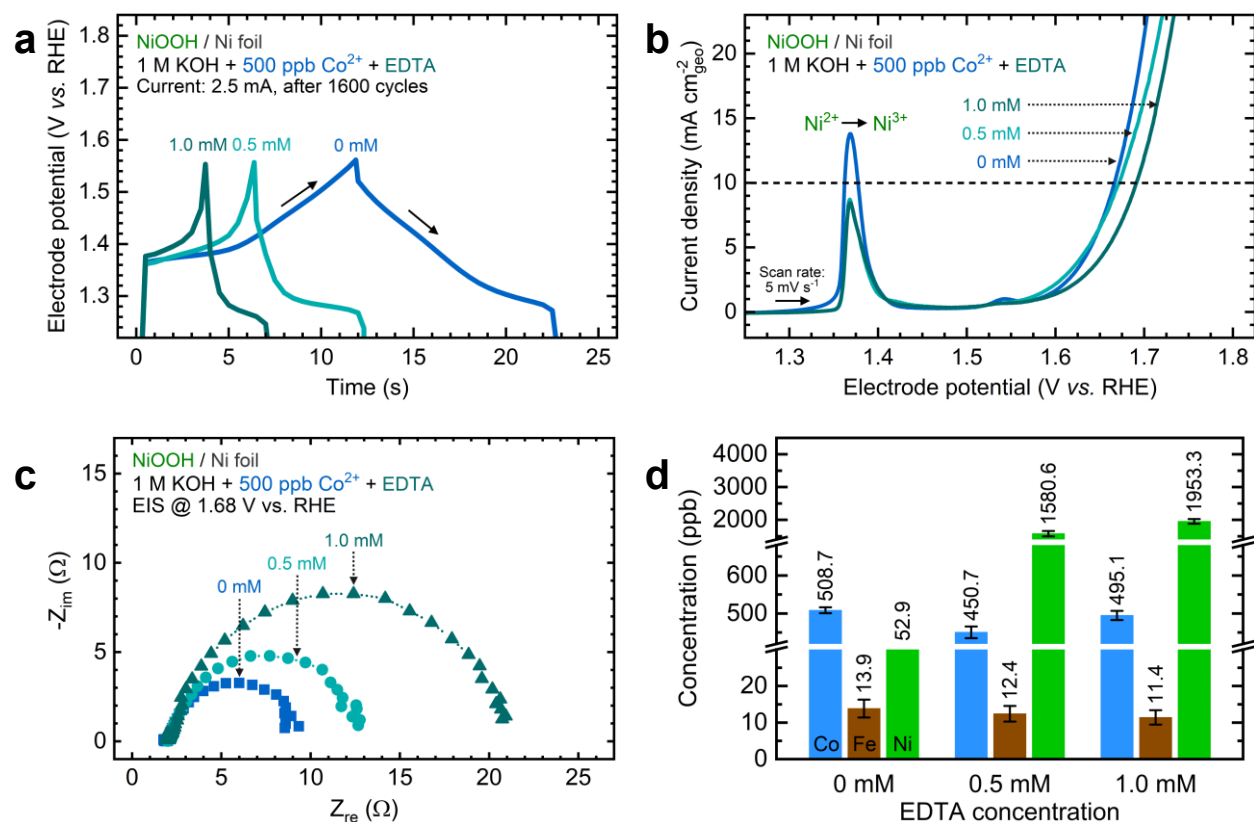


**Figure S43.** Reversing Co incorporation on NF-NiOOH electrodes *via* metal complexation: (a) GCD conditioning at 2.5 mA·cm<sup>-2</sup> in purified 1 M KOH electrolyte containing 500 ppb of Co<sup>2+</sup> at increasing EDTA concentrations, (b) LSV scans and (c) Nyquist plots corresponding to the EDTA concentrations specified in panel (a); (d) Ni, Co, and Fe concentrations in the 1 M KOH electrolyte after GCD conditioning at increasing EDTA concentrations. Metal concentrations in the electrolyte were determined *via* solution-mode ICP-MS using 100  $\mu$ L samples collected after conditioning. Uncertainty bars indicate the standard deviation derived from three replicate measurements.

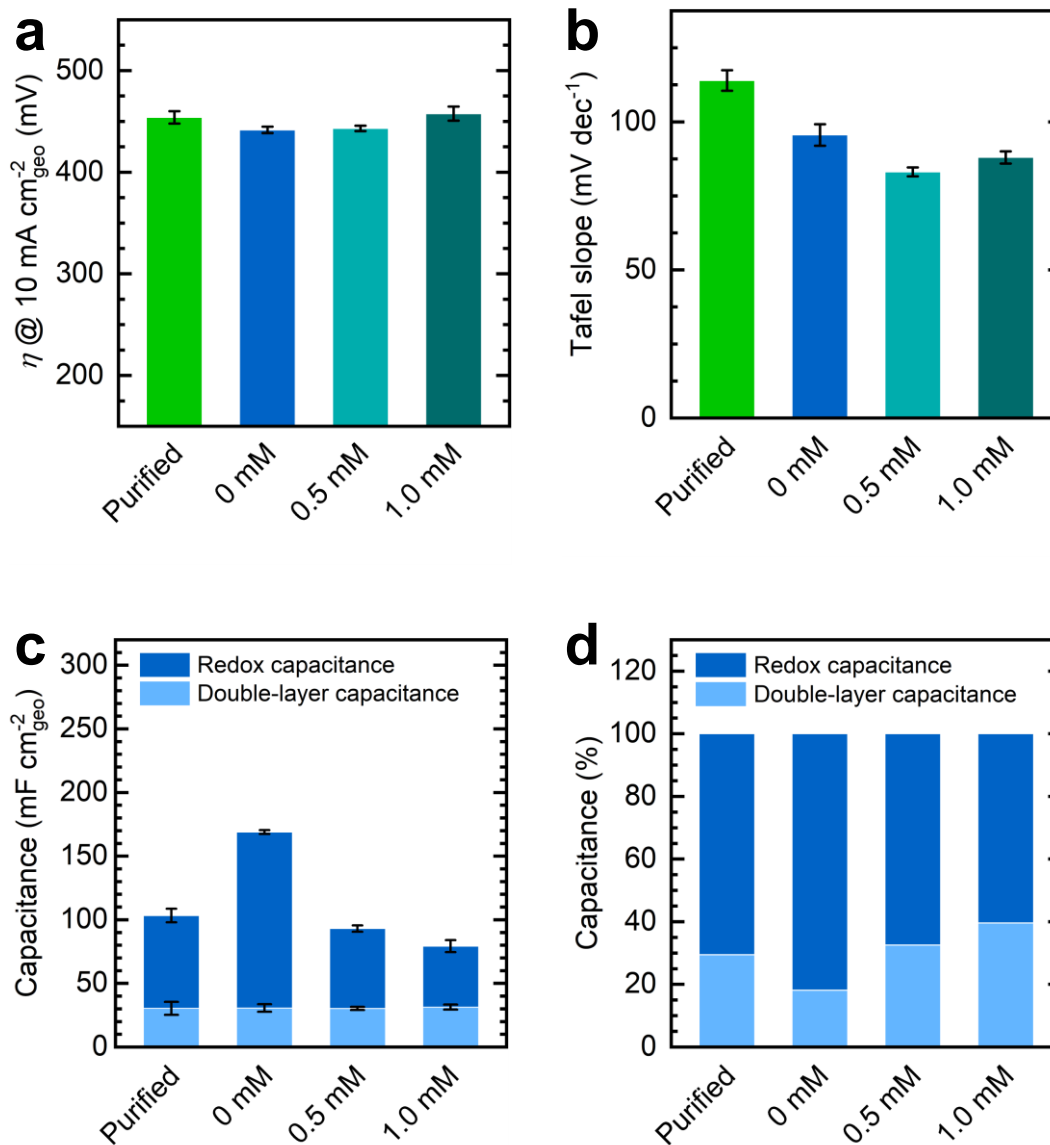


**Figure S44.** Reversing Co incorporation on NF-NiOOH electrodes *via* metal complexation: (a) OER overpotentials at 10 mA cm<sup>-2</sup><sub>geo</sub> and (b) Tafel slopes measured after GCD conditioning in purified 1 M KOH electrolyte containing 500 ppb of Co<sup>2+</sup> at increasing EDTA concentrations; (c) total and (d) relative capacitance contributions at increasing EDTA concentrations. OER overpotentials are determined from LSV scans. Tafel slopes are calculated as the average values obtained from MUSCP and MUSCA methods. Redox and double-layer capacitances are estimated from GCD and EIS measurements, respectively. Uncertainty bars indicate the standard deviation derived from three replicate measurements.

## References

- (1) Márquez, R. A.; Kawashima, K.; Son, Y. J.; Castelino, G.; Miller, N.; Smith, L. A.; Chukwunke, C. E.; Mullins, C. B. Getting the Basics Right: Preparing Alkaline Electrolytes for Electrochemical Applications. *ACS Energy Lett.* **2023**, *8* (2), 1141–1146. <https://doi.org/10.1021/acseenergylett.2c02847>.
- (2) Stevens, M. B.; Enman, L. J.; Batchellor, A. S.; Cosby, M. R.; Vise, A. E.; Trang, C. D. M.; Boettcher, S. W. Measurement Techniques for the Study of Thin Film Heterogeneous Water Oxidation Electrocatalysts. *Chem. Mater.* **2017**, *29* (1), 120–140. <https://doi.org/10.1021/acs.chemmater.6b02796>.
- (3) Trotochaud, L.; Young, S. L.; Ranney, J. K.; Boettcher, S. W. Nickel–Iron Oxyhydroxide Oxygen-Evolution Electrocatalysts: The Role of Intentional and Incidental Iron Incorporation. *J. Am. Chem. Soc.* **2014**, *136* (18), 6744–6753. <https://doi.org/10.1021/ja502379c>.
- (4) Burke, M. S.; Kast, M. G.; Trotochaud, L.; Smith, A. M.; Boettcher, S. W. Cobalt–Iron (Oxy)Hydroxide Oxygen Evolution Electrocatalysts: The Role of Structure and Composition on Activity, Stability, and Mechanism. *J. Am. Chem. Soc.* **2015**, *137* (10), 3638–3648. <https://doi.org/10.1021/jacs.5b00281>.
- (5) Hoang, T. T. H.; Gewirth, A. A. High Activity Oxygen Evolution Reaction Catalysts from Additive-Controlled Electrodeposited Ni and NiFe Films. *ACS Catal.* **2016**, *6* (2), 1159–1164. <https://doi.org/10.1021/acscatal.5b02365>.
- (6) Chen, R.; Yang, C.; Cai, W.; Wang, H.-Y.; Miao, J.; Zhang, L.; Chen, S.; Liu, B. Use of Platinum as the Counter Electrode to Study the Activity of Nonprecious Metal Catalysts for the Hydrogen Evolution Reaction. *ACS Energy Lett.* **2017**, *2* (5), 1070–1075. <https://doi.org/10.1021/acseenergylett.7b00219>.
- (7) Kawashima, K.; Márquez, R. A.; Son, Y. J.; Guo, C.; Vaidyula, R. R.; Smith, L. A.; Chukwunke, C. E.; Mullins, C. B. Accurate Potentials of Hg/HgO Electrodes: Practical Parameters for Reporting Alkaline Water Electrolysis Overpotentials. *ACS Catal.* **2023**, *13* (3), 1893–1898. <https://doi.org/10.1021/acscatal.2c05655>.
- (8) Jerkiewicz, G. Standard and Reversible Hydrogen Electrodes: Theory, Design, Operation, and Applications. *ACS Catal.* **2020**, *10* (15), 8409–8417. <https://doi.org/10.1021/acscatal.0c02046>.
- (9) Feltham, A. M.; Spiro, M. Platinized Platinum Electrodes. *Chem. Rev.* **1971**, *71* (2), 177–193. <https://doi.org/10.1021/cr60270a002>.
- (10) Louie, M. W.; Bell, A. T. An Investigation of Thin-Film Ni–Fe Oxide Catalysts for the Electrochemical Evolution of Oxygen. *J. Am. Chem. Soc.* **2013**, *135* (33), 12329–12337. <https://doi.org/10.1021/ja405351s>.
- (11) Son, Y. J.; Kim, S.; Leung, V.; Kawashima, K.; Noh, J.; Kim, K.; Marquez, R. A.; Carrasco-Jaim, O. A.; Smith, L. A.; Celio, H.; Milliron, D. J.; Korgel, B. A.; Mullins, C. B. Effects of Electrochemical Conditioning on Nickel-Based Oxygen Evolution Electrocatalysts. *ACS Catal.* **2022**, *12* (16), 10384–10399. <https://doi.org/10.1021/acscatal.2c01001>.
- (12) Sanchis-Gual, R.; Seijas-Da Silva, A.; Coronado-Puchau, M.; Otero, T. F.; Abellán, G.; Coronado, E. Improving the Onset Potential and Tafel Slope Determination of Earth-

- Abundant Water Oxidation Electrocatalysts. *Electrochim. Acta* **2021**, 388, 138613. <https://doi.org/10.1016/j.electacta.2021.138613>.
- (13) Klaus, S.; Cai, Y.; Louie, M. W.; Trotochaud, L.; Bell, A. T. Effects of Fe Electrolyte Impurities on Ni(OH)<sub>2</sub>/NiOOH Structure and Oxygen Evolution Activity. *J. Phys. Chem. C* **2015**, 119 (13), 7243–7254. <https://doi.org/10.1021/acs.jpcc.5b00105>.
- (14) Anantharaj, S.; Noda, S.; Driess, M.; Menezes, P. W. The Pitfalls of Using Potentiodynamic Polarization Curves for Tafel Analysis in Electrocatalytic Water Splitting. *ACS Energy Lett.* **2021**, 6 (4), 1607–1611. <https://doi.org/10.1021/acscenergylett.1c00608>.
- (15) Gogotsi, Y.; Penner, R. M. Energy Storage in Nanomaterials – Capacitive, Pseudocapacitive, or Battery-Like? *ACS Nano* **2018**, 12 (3), 2081–2083. <https://doi.org/10.1021/acsnano.8b01914>.
- (16) Gamry Instruments. Testing Electrochemical Capacitors Part 2 Cyclic Charge Discharge and Stacks. *Gamry Application Notes*. <https://www.gamry.com/application-notes/battery-research/electrochemical-capacitors-cyclic-charge-discharge-and-stacks/>.
- (17) Brousse, T.; Bélanger, D.; Long, J. W. To Be or Not To Be Pseudocapacitive? *J. Electrochem. Soc.* **2015**, 162 (5), A5185. <https://doi.org/10.1149/2.0201505jes>.
- (18) Simon, P.; Gogotsi, Y.; Dunn, B. Where Do Batteries End and Supercapacitors Begin? *Science* **2014**, 343 (6176), 1210–1211. <https://doi.org/10.1126/science.1249625>.
- (19) Evanko, B.; Boettcher, S. W.; Yoo, S. J.; Stucky, G. D. Redox-Enhanced Electrochemical Capacitors: Status, Opportunity, and Best Practices for Performance Evaluation. *ACS Energy Lett.* **2017**, 2 (11), 2581–2590. <https://doi.org/10.1021/acscenergylett.7b00828>.
- (20) Son, Y. J.; Kawashima, K.; Wygant, B. R.; Lam, C. H.; Burrow, J. N.; Celio, H.; Dolocan, A.; Ekerdt, J. G.; Mullins, C. B. Anodized Nickel Foam for Oxygen Evolution Reaction in Fe-Free and Unpurified Alkaline Electrolytes at High Current Densities. *ACS Nano* **2021**, 15 (2), 3468–3480. <https://doi.org/10.1021/acsnano.0c10788>.
- (21) Zheng, W. iR Compensation for Electrocatalysis Studies: Considerations and Recommendations. *ACS Energy Lett.* **2023**, 1952–1958. <https://doi.org/10.1021/acscenergylett.3c00366>.
- (22) Son, Y. J.; Marquez, R. A.; Kawashima, K.; Smith, L. A.; Chukwunke, C. E.; Babauta, J.; Mullins, C. B. Navigating iR Compensation: Practical Considerations for Accurate Study of Oxygen Evolution Catalytic Electrodes. *ACS Energy Lett.* **2023**, 8 (10), 4323–4329. <https://doi.org/10.1021/acscenergylett.3c01658>.
- (23) *The Constant Phase Element - CPE*. Electrochemistry Resources. <https://electrochemistryresources.com/the-constant-phase-element-cpe/> (accessed 2021-09-09).
- (24) Yoon, Y.; Yan, B.; Surendranath, Y. Suppressing Ion Transfer Enables Versatile Measurements of Electrochemical Surface Area for Intrinsic Activity Comparisons. *J. Am. Chem. Soc.* **2018**, 140 (7), 2397–2400. <https://doi.org/10.1021/jacs.7b10966>.
- (25) Morales, D. M.; Risch, M. Seven Steps to Reliable Cyclic Voltammetry Measurements for the Determination of Double Layer Capacitance. *J. Phys. Energy* **2021**, 3 (3), 034013. <https://doi.org/10.1088/2515-7655/abee33>.
- (26) Peña, F. de la; Prestat, E.; Fauske, V. T.; Burdet, P.; Lähnemann, J.; Jokubauskas, P.; Furnival, T.; Nord, M.; Ostasevicius, T.; MacArthur, K. E.; Johnstone, D. N.; Sarahan, M.;

- Taillon, J.; Aarholt, T.; pquinn-dls; Migunov, V.; Eljarrat, A.; Caron, J.; Francis, C.; Nemoto, T.; Poon, T.; Mazzucco, S.; actions-user; Tappy, N.; Cautaerts, N.; Somnath, S.; Slater, T.; Walls, M.; Winkler, F.; Ánes, H. W. Hyperspy/Hyperspy: Release v1.7.3. *Zenodo* **2022**. <https://doi.org/10.5281/zenodo.7263263>.
- (27) Biesinger, M. C.; Payne, B. P.; Lau, L. W. M.; Gerson, A.; Smart, R. St. C. X-Ray Photoelectron Spectroscopic Chemical State Quantification of Mixed Nickel Metal, Oxide and Hydroxide Systems. *Surf. Interface Anal.* **2009**, *41* (4), 324–332. <https://doi.org/10.1002/sia.3026>.
- (28) Biesinger, M. C.; Payne, B. P.; Grosvenor, A. P.; Lau, L. W. M.; Gerson, A. R.; Smart, R. St. C. Resolving Surface Chemical States in XPS Analysis of First Row Transition Metals, Oxides and Hydroxides: Cr, Mn, Fe, Co and Ni. *Applied Surface Science* **2011**, *257* (7), 2717–2730. <https://doi.org/10.1016/j.apsusc.2010.10.051>.
- (29) Grosvenor, A. P.; Biesinger, M. C.; Smart, R. St. C.; McIntyre, N. S. New Interpretations of XPS Spectra of Nickel Metal and Oxides. *Surf. Sci.* **2006**, *600* (9), 1771–1779. <https://doi.org/10.1016/j.susc.2006.01.041>.
- (30) Kawashima, K.; Márquez-Montes, R. A.; Li, H.; Shin, K.; Cao, C. L.; Vo, K. M.; Son, Y. J.; Wygant, B. R.; Chunangad, A.; Youn, D. H.; Henkelman, G.; Ramos-Sánchez, V. H.; Mullins, C. B. Electrochemical Behavior of a Ni<sub>3</sub>N OER Precatalyst in Fe-Purified Alkaline Media: The Impact of Self-Oxidation and Fe Incorporation. *Mater. Adv.* **2021**, *2*, 2299–2309. <https://doi.org/10.1039/D1MA00130B>.
- (31) Hall, D. S.; Bock, C.; MacDougall, B. R. An Oxalate Method for Measuring the Surface Area of Nickel Electrodes. *J. Electrochem. Soc.* **2014**, *161* (12), H787. <https://doi.org/10.1149/2.0711412jes>.
- (32) Bode, H.; Dehmelt, K.; Witte, J. Zur Kenntnis Der Nickelhydroxidelektrode—I.Über Das Nickel (II)-Hydroxidhydrat. *Electrochimica Acta* **1966**, *11* (8), 1079–1087. [https://doi.org/10.1016/0013-4686\(66\)80045-2](https://doi.org/10.1016/0013-4686(66)80045-2).
- (33) Lyons, M. E. G.; Brandon, M. P. The Oxygen Evolution Reaction on Passive Oxide Covered Transition Metal Electrodes in Aqueous Alkaline Solution. Part 1-Nickel. *Int. J. Electrochem. Sci.* **2008**, *3*, 39. [https://doi.org/10.1016/S1452-3981\(23\)15531-3](https://doi.org/10.1016/S1452-3981(23)15531-3).
- (34) Dionigi, F.; Strasser, P. NiFe-Based (Oxy)Hydroxide Catalysts for Oxygen Evolution Reaction in Non-Acidic Electrolytes. *Adv. Energy Mater.* **2016**, *6* (23), 1600621. <https://doi.org/10.1002/aenm.201600621>.
- (35) Heymann, L.; Weber, M. L.; Wohlgemuth, M.; Risch, M.; Dittmann, R.; Baeumer, C.; Gunkel, F. Separating the Effects of Band Bending and Covalency in Hybrid Perovskite Oxide Electrocatalyst Bilayers for Water Electrolysis. *ACS Appl. Mater. Interfaces* **2022**, *14* (12), 14129–14136. <https://doi.org/10.1021/acsami.1c20337>.
- (36) Hong, W. T.; Stoerzinger, K. A.; Moritz, B.; Devereaux, T. P.; Yang, W.; Shao-Horn, Y. Probing LaMO<sub>3</sub> Metal and Oxygen Partial Density of States Using X-Ray Emission, Absorption, and Photoelectron Spectroscopy. *J. Phys. Chem. C* **2015**, *119* (4), 2063–2072. <https://doi.org/10.1021/jp511931y>.
- (37) Hong, W. T.; Stoerzinger, K. A.; Lee, Y.-L.; Giordano, L.; Grimaud, A.; Johnson, A. M.; Hwang, J.; Crumlin, E. J.; Yang, W.; Shao-Horn, Y. Charge-Transfer-Energy-Dependent Oxygen Evolution Reaction Mechanisms for Perovskite Oxides. *Energy Environ. Sci.* **2017**, *10* (10), 2190–2200. <https://doi.org/10.1039/C7EE02052J>.

- (38) Shannon, R. D. Revised Effective Ionic Radii and Systematic Studies of Interatomic Distances in Halides and Chalcogenides. *Acta Cryst A* **1976**, *32* (5), 751–767. <https://doi.org/10.1107/S0567739476001551>.
- (39) Penn State University. *Introduction to Inorganic Chemistry (Wikibook)*; LibreTexts Chemistry.
- (40) Manthiram, A. A Reflection on Lithium-Ion Battery Cathode Chemistry. *Nat. Commun.* **2020**, *11* (1), 1550. <https://doi.org/10.1038/s41467-020-15355-0>.
- (41) Harris, D. C.; Lucy, C. A. *Quantitative Chemical Analysis*, Ninth Edition.; W. H. Freeman and Company, 2016.
- (42) Jain, A.; Ong, S. P.; Hautier, G.; Chen, W.; Richards, W. D.; Dacek, S.; Cholia, S.; Gunter, D.; Skinner, D.; Ceder, G.; Persson, K. A. Commentary: The Materials Project: A Materials Genome Approach to Accelerating Materials Innovation. *APL Materials* **2013**, *1* (1), 011002. <https://doi.org/10.1063/1.4812323>.
- (43) Singh, A. K.; Zhou, L.; Shinde, A.; Suram, S. K.; Montoya, J. H.; Winston, D.; Gregoire, J. M.; Persson, K. A. Electrochemical Stability of Metastable Materials. *Chem. Mater.* **2017**, *29* (23), 10159–10167. <https://doi.org/10.1021/acs.chemmater.7b03980>.
- (44) Patel, A. M.; Nørskov, J. K.; Persson, K. A.; Montoya, J. H. Efficient Pourbaix Diagrams of Many-Element Compounds. *Phys. Chem. Chem. Phys.* **2019**, *21* (45), 25323–25327. <https://doi.org/10.1039/C9CP04799A>.
- (45) Persson, K. A.; Waldwick, B.; Lazic, P.; Ceder, G. Prediction of Solid-Aqueous Equilibria: Scheme to Combine First-Principles Calculations of Solids with Experimental Aqueous States. *Phys. Rev. B* **2012**, *85* (23), 235438. <https://doi.org/10.1103/PhysRevB.85.235438>.